



THE HONG KONG
POLYTECHNIC UNIVERSITY

香港理工大學

Pao Yue-kong Library

包玉剛圖書館

Copyright Undertaking

This thesis is protected by copyright, with all rights reserved.

By reading and using the thesis, the reader understands and agrees to the following terms:

1. The reader will abide by the rules and legal ordinances governing copyright regarding the use of the thesis.
2. The reader will use the thesis for the purpose of research or private study only and not for distribution or further reproduction or any other purpose.
3. The reader agrees to indemnify and hold the University harmless from and against any loss, damage, cost, liability or expenses arising from copyright infringement or unauthorized usage.

IMPORTANT

If you have reasons to believe that any materials in this thesis are deemed not suitable to be distributed in this form, or a copyright owner having difficulty with the material being included in our database, please contact lbsys@polyu.edu.hk providing details. The Library will look into your claim and consider taking remedial action upon receipt of the written requests.

**MODELING AND ANALYSIS OF
BIOMIMETIC STRUCTURES WITH
SELF-CLEANING PROPERTIES
FABRICATED BY ULTRA-PRECISION
MACHINING**

CHENG CHEUNG TONG

Ph.D

The Hong Kong Polytechnic University

2016

The Hong Kong Polytechnic University

Department of Industrial and Systems Engineering

**Modeling and Analysis of Biomimetic Structures
with Self-cleaning Properties Fabricated by Ultra-
precision Machining**

CHENG Cheung Tong

A thesis submitted in partial fulfillment of the requirements
for the degree of Doctor of Philosophy

April 2016

CERTIFICATE OF ORIGINALITY

I hereby declare that this thesis is my own work and that, to the best of my knowledge and belief, it reproduces no material previously published or written, nor material that has been accepted for the award of any other degree or diploma, except where due acknowledgement has been made in the text.

_____ (Signed)

CHENG Cheung Tong (Name of student)

Abstract

Biomimetic structures with hydrophobic properties have enormous potential for applications on artificial self-cleaning surfaces, such as the next generation of vehicle windshields, exterior paint for buildings, and solar panels, due to their excellent water repellence properties. Although most of the recent studies focus on the fabrication methods of hydrophobic surfaces for self-cleaning, and the wetting behavior on self-cleaning surfaces, there are still great challenges in applying one-step manufacturing methods to fabricate bare hydrophobic micro-patterned surfaces with good sliding and optical performance for mass production. This involves fabricating, analyzing, and characterizing micro-patterned surfaces taking into account the wetting characteristics, droplet wetting states, and optical performance for advanced self-cleaning surfaces.

This thesis is divided into four parts. In the first part, optimization modeling of the surface geometries of biomimetic structures for self-cleaning has been developed based on an optical function and a wetting model of micro-patterned surfaces, considering hydrophobicity and optical performance.

The second part of the thesis describes investigations on the wetting characteristics of bare hydrophobic micro-patterned cyclic olefin copolymer surfaces machined by a one-step fabrication method, ultra-precision raster milling

(UPRM), which is potentially applicable for the mass production of plastic injection moldings. Water droplets are governed by the Cassie and Baxter regime, and are stabilized by the sharp edges induced by the numerical-controlled tool path in the material removal process in the mechanical machining of the top asperities of the micro-patterns after deposition on the surfaces. This results in a good sliding performance on the micro-grooved surfaces.

In the third part, a characterization method for the droplet wetting states, significantly affecting its sliding performance on hydrophobic surfaces, is proposed, based on observations of the droplet contact lines on the micro-grooved surfaces. This characterization method is capable of identifying intermediate wetting states but it is difficult to use traditional verification methods for such identification. The partial wetting state is found to be the sliding boundary of the micro-grooved surfaces, whereas droplets contacting the side walls of the grooves still form a favorable wetting state for the anisotropic sliding on the micro-grooved surfaces.

In the fourth part, the anisotropic wetting of micro-micro hierarchical structured surfaces fabricated by ultra-precision machining, including regular, irregular, and multi-level hierarchical structures, have been investigated. It is found that applying irregular hierarchical structures and multi-level design can

further enhance the water static contact angle to over 150° and 161° respectively. This is achieved by inducing more energy barriers, reducing the contact area of the solid-liquid interface, and reserving more buffers to air pocket formation.

The originality and significance of this research include: (i) an optimization modeling for the surface geometries of biomimetic structures for advanced self-cleaning surfaces has been established; (ii) highly controllable one-step fabrication methods, potentially applicable for mass production in the plastic injection molding of bare micro-patterned surfaces with good sliding and optical performance, are proposed through study of the wetting characteristics; (iii) a characterization method for the droplet wetting states, that significantly affect the sliding performance on hydrophobic surfaces, is firstly proposed from observations of the droplet contact lines on micro-patterned surfaces; (iv) this characterization method is capable of identifying intermediate wetting states which show the sliding boundary and the favorable wetting state for anisotropic sliding on the micro-grooved surfaces. This provides more flexibility for the design of advanced self-cleaning surfaces.

Publications Arising from this Study

Journal Papers

1. **Cheng Cheung Tong**, Zhang Guoqing and To Suet, “Wetting Characteristics of Bare Micro-patterned Cyclic Olefin Copolymer Surfaces fabricated by Ultra-precision Raster Milling”, *RSC Advances*, Vol.6, pp.1562-1570 (2016). (Impact Factor: 3.84)
2. **Cheng Cheung Tong**, To Suet and Zhang Guoqing, “Characterization of Anisotropic Wetting on Micro-Directional Grooved Surfaces”, *Applied Surface Science*, under review and revision.
3. **Cheng Cheung Tong**, To Suet, Chan Chang Yuen and Cheung Chi Fai, “An Investigation on the Effect of Ultra-precision Machined Patterns in Wetting Transition”, *International Journal of Nanomanufacturing*, Vol.7, pp.245-266 (2011).
4. Kong Ling Bao, Cheung Chi Fai, To Suet and **Cheng Cheung Tong**, “Modeling and Characterization of Generation of 3D Micro-structured Surfaces with Self-cleaning and Optical Functions”, *Optik*, Vol.124, pp.2848-2853 (2013).
5. **Cheng Cheung Tong**, To Suet and Zhu Zhiwei, “Anisotropic wetting of micro-micro hierarchical cyclic olefin copolymer surfaces fabricated by end-fly-cutting-servo diamond machining”, *Applied Surface Science*, under preparation.
6. **Cheng Cheung Tong** and To Suet, “Transparent, superhydrophobic, and high haze micro-patterned cyclic olefin copolymer surfaces fabricated by ultra-precision raster milling”, *Journal of Colloid and Interface Science*, under preparation.
7. **Cheng Cheung Tong** and To Suet, “Superhydrophobic surface of multi-level hierarchical structures fabricated by end-fly-cutting”, *Soft Matter*, under preparation.

Conference Papers

1. **Cheng Cheung Tong** and To Suet, “Wetting Transition of Ultra-Precision Machined Hydrophobic Surfaces”. *The 4th Asia Pacific Conference on Optics Manufacture (APCOM)*, Guangzhou, China, 9-11 November (2014). (Oral presentation)
2. **Cheng Cheung Tong**, To Suet, Chan Chang Yuen and Cheung Chi Fai, “An investigation of fabrication of micro patterns from using different cutting strategies in ultra-precision raster milling”. *The 5th International Conference of Asian Society for Precision Engineering and Nanotechnology (APSEN)*, Taipei, Taiwan, 12-15 November (2013). (Oral presentation)
3. **Cheng Cheung Tong**, To Suet, Chan Chang Yuen and Cheung Chi Fai, “Fabrication of Biomimetic Structures for Self-cleaning in Ultra-precision Machining”. *The 12th International Conference of the Eurospen Society for Precision Engineering & Nanotechnology*, Stockholm, Sweden, 4-8 June (2012). (Poster presentation)
4. **Cheng Cheung Tong**, To Suet, Chan Chang Yuen and Cheung Chi Fai, “A study of design, fabrication and characterization of micro patterns from ultra-precision raster milling.” *The 4th International Conference of Asian Society for Precision Engineering and Nanotechnology (APSEN)*, Hong Kong, 15-18 November (2011). (Oral presentation)
5. **Cheng Cheung Tong**, To Suet, Chan Chang Yuen and Cheung Chi Fai, “The influence of ultra-precision machined patterns on self-cleaning properties”, *The 2nd International Conference on Nanomanufacturing*, Tianjin, China, 24-26 September (2010). (Oral presentation)

Acknowledgments

I would like to express my sincere appreciation and thanks to my chief supervisor, Dr Sandy Suet To, Associate Professor of the Department of Industrial and Systems Engineering of The Hong Kong Polytechnic University and Associate Director of the State Key Laboratory in Ultra-precision Machining Technology, for her valuable guidance, encouragement, support, and advice. Without her consistent guidance, this thesis could not have been completed. I would also like to thank my co-supervisors, Prof. Benny C. F. Cheung, Professor of the Department of Industrial and Systems Engineering and Associate Director of the State Key Laboratory in Ultra-precision Machining Technology, and Prof. W. B. Lee, Cheng Yick Chi Chair Professor of Manufacturing Engineering and Director of the State Key Laboratory in Ultra-precision Machining Technology, for their valuable ideas and advice.

I also wish to thank the Research Committee of The Hong Kong Polytechnic University, and The Innovation and Technology Fund of the Government of the Hong Kong Special Administrative Region of the People's of Republic of China for providing the financial support for this research work under the Project Nos. 4-RPLU and ITS/390/09 respectively.

Many thanks are extended to Dr. Joe C. Y. Chan, Dr. Bobby L. B. Kong, Mr.

K. C. Cheung, Mr. T. W. Chung, Mr. Jon Wong, Mr. David Lai, Mr. C. M. Wong, Mr. Alex Wong, Mr. T. H. Fan, Ms. May Chun, Dr. Lesley Ho, and all the staff in the State Key Laboratory in Ultra-precision Machining Technology for their valuable advice and technical support. I also owe sincere thanks to my friends Dr. Guoqing Zhang, Dr. Zhiwei Zhu, Dr. Shaojin Zhang, Dr. Gaobo Xiao, Mr. Quanli Zhang, Mr. Jackie Chow, Dr. Hao Wang, Dr. Haotiao Wang, Dr. Sujuan Wang and Mr. Felix Ng for their encouragement and help.

Finally, I would like to deeply thank my beloved family: my sisters Miss Meina Cheng, and Miss Anna Cheng, and my parents for their loving consideration and great confidence in me during this study. Without their patience and understanding, I could not successfully complete my study.

Table of Contents

Abstract	i
Publications Arising from this Study	iv
Acknowledgments	vi
Table of Contents	viii
List of Figures	xii
List of Tables	xxii
Chapter 1 Introduction	1
1.1 Background of Research	1
1.2 Research Objectives and Significance	4
1.3 Organization of the Thesis	5
Chapter 2 Literature Review	8
2.1 Overview of Biomimetic Self-cleaning Industry	8
2.2 Categories of Superhydrophobic Surfaces in Nature	12
2.2.1 Lotus Leaf	12
2.2.2 Rice Leaf	13
2.2.3 Cicada Wing	15
2.2.4 Butterfly Wing	16
2.3 Fabrication Technologies of Superhydrophobic Surfaces	17
2.4 Development of Ultra-precision Machining Technologies	22
2.4.1 Single-point Diamond Turning (SPDT)	22
2.4.2 Ultra-precision Grinding (UPG)	23
2.4.3 Ultra-precision Raster Milling (UPRM)	24
2.5 Major Factors Affecting Self-cleaning Performance	27
2.5.1 Surface Geometries	27
2.5.2 Materials	29
2.5.3 Contact Area with Liquid	30
2.5.4 Droplet Contact Line	31
2.6 Characterization of Droplet Wetting States	32
2.7 Modeling and Optimization Approaches	36
2.7.1 Static Contact Angle	37
2.7.2 Dynamic Contact Angle	42
2.8 Summary	45

Chapter 3 Optimization Modeling of Biomimetic Structures for Self-cleaning and Optical Performance	47
3.1 Introduction	47
3.2 Design Criteria of Surface Geometry	49
3.2.1 Self-cleaning Performance Requirements	49
3.2.2 Optical Performance Requirements	53
3.2.3 Consideration of Machining Ability	54
3.2.4 Design Challenge	55
3.3 Structure Design	56
3.3.1 Mathematical Model for Micro-grooved Surfaces	57
3.3.2 Mathematical Model for Micro-pillar Surfaces	59
3.4 Experimental Procedures	60
3.4.1 Fabrication of Micro-patterns Using Ultra-precision Raster Milling	60
3.4.2 Surface Topography Measurement	62
3.4.3 Contact Angle Measurement	65
3.5 Results and Discussion	66
3.5.1 Static Contact Angle Measurement	66
3.5.2 Length of Water Droplet Elongation	71
3.5.3 Optical Testing of Biomimetic Structures	75
3.6 Summary	78
Chapter 4 Wetting Characteristics of Micro-patterned Surfaces Fabricated by Ultra-precision Raster Milling	81
4.1 Introduction	81
4.2 Experimentation	82
4.2.1 Experimental Setup	82
4.2.2 Fabrication of Micro-patterned Surfaces	84
4.2.3 Micro-patterned Surface Topography	87
4.3 Results and Discussion	91
4.3.1 Comparison with the Theoretical Models	91
4.3.1.1 The Wenzel Model	91
4.3.1.2 The Cassie and Baxter Model	95
4.3.2 Static Contact Angle from the Experiment	97
4.3.3 Droplet Anisotropy	100
4.3.4 Droplet Contact Line	101
4.3.5 Contact Angle Hysteresis	103
4.3.6 Sliding Angle Measurement	107
4.4 Summary	110

Chapter 5	Characterization of Intermediate Wetting States and Anisotropic Sliding on Micro-directional Grooved Surfaces	112
5.1	Introduction	112
5.2	Experimentation	113
5.2.1	Fabrication of Micro-directional Grooved Surfaces using UPRM	113
5.2.2	Micro-directional Grooved Surface Topography	115
5.3	Results and Discussion	117
5.3.1	Observation of Droplet Contact Line	117
5.3.2	Plot of Static Contact Angle against Droplet Deposition Time	123
5.3.3	Comparison with the Theoretical Models	128
5.3.4	Anisotropic Sliding Behavior	136
5.4	Summary	142
Chapter 6	Anisotropic Wetting of Micro-Micro Hierarchical Structures Fabricated by Ultra-precision Machining	144
6.1	Introduction	144
6.2	Regular Micro-Micro Hierarchical Structures Fabricated by UPRM	146
6.2.1	Experimental Setup	146
6.2.2	Fabrication of Regular Micro-Micro Hierarchical Structures	147
6.2.3	Surface Topography Measurement	150
6.2.4	Results and Discussion	152
6.3	Irregular Micro-Micro Hierarchical Structures Fabricated by EFCS	159
6.3.1	Experimental Setup	159
6.3.2	Fabrication of Irregular Micro-Micro Hierarchical Structures	160
6.3.3	Surface Topography Measurement	161
6.3.4	Results and Discussion	162
6.4	Multi-level Hierarchical Structures Fabricated by EFC	166
6.4.1	Experimental Setup	167
6.4.2	Fabrication of Multi-level Hierarchical Structures	168
6.4.3	Surface Topography Measurement	169
6.4.4	Results and Discussion	169
6.5	Summary	175
Chapter 7	Conclusions and Suggestions for Further Work	178
7.1	Overall Conclusions	178
7.2	Suggestions for Future Work	184

Lists of Figures

Figure 2.1	Potential applications of self-cleaning surfaces.	9
Figure 2.2	Possible elements challenging self-cleaning surfaces.	9
Figure 2.3	Categories of self-cleaning surfaces (Nishimoto and Bhushan, 2013).	11
Figure 2.4	(a) SEM images of the front surface of the lotus leaf with hierarchical micro-nanostructures (Bhushan et al., 2009), (b) hierarchical micro-nanostructures shown in surface height map (Cheng et al., 2006), (c) an enlarged SEM image of a micro-pillar with nano-hair in wax (Cheng et al., 2006), and (d) a water droplet on the front surface of the lotus leaf (Bhushan et al., 2009).	13
Figure 2.5	(a) A water droplet on the front surface of the rice leaf, and (b) the hierarchical micro-nanostructures on the rice leaf shown in SEM image (Bixler and Bhushan, 2012).	14
Figure 2.6	(a) SEM image of cicada wing (Lee et al., 2004), and (b) AFM image and the cross section profile of the nanostructures on cicada wing (Watson et al., 2008).	16
Figure 2.7	(a) Water droplets on a blue butterfly wing (Bixler and Bhushan, 2013), (b) SEM images of the hierarchical micro- and nano-structures on the surface of the butterfly wings (Zheng et al., 2007), (c) AFM images of the overlapping micro-scales and nano-stripe structures (Zheng et al., 2007), and (d) Water droplets are tilted along	17

	and against the RO direction (Zheng et al., 2007).	
Figure 2.8	Superhydrophobic surfaces fabricated by (a) Lithography (Zhao et al., 2012), (b) Plasma treatment after lithography (Park et al., 2012), (c) Electrochemical anodization (Xiao et al., 2015), (d) Laser processing (Yong et al., 2014), (e) Sol-gel coating (Rao et al., 2009), (f) Chemical reaction (Levkin et al., 2009), (g) Electrospinning (Ma et al., 2005), (h) Self-assembly (Yang et al., 2013), and (i) Molding using template (Greiner et al., 2009).	19
Figure 2.9	(a) Single-point diamond turning, and (b) Single crystal diamond tool.	23
Figure 2.10	Ultra-precision grinding (Zhang et al., 2015).	24
Figure 2.11	Ultra-precision raster milling.	25
Figure 2.12	The front surface of the lotus leaf with nanometer structure shown in (a) SEM image and (b) surface height maps (Cheng et al., 2006).	27
Figure 2.13	The back surface of the lotus leaf with nanometer structure shown by (a) SEM image and (b) surface height maps (Cheng et al., 2006).	28
Figure 2.14	A liquid droplet (a) with force at three-phase contact line on a smooth surface, (b) under Wenzel state on a rough surface, and (c) under Cassie-Baxter state on a rough surface.	39
Figure 2.15	Contact angle hysteresis measurements using (a) sessile drop method, and (b) tilting plate method.	43
Figure 3.1	Schematic diagram of the methodology for modeling and	48

	optimizing biomimetic structures for self-cleaning in ultra-precision machining.	
Figure 3.2	Two typical structures surface design (a) frustum ridge, and (b) frustum pillar (Kong et al., 2012).	51
Figure 3.3	Optical images of (a) a round tool with a tool nose radius, (b) an acute tool with a rake angle, and (c) a facet tool with a tool width used in ultra-precision raster milling (Kong et al., 2013).	55
Figure 3.4	A mathematical model of micro-directional grooved surfaces.	57
Figure 3.5	(a) 2D plot of profile, and (b) 3D Plot of frustum ridge by the mathematical model with input parameter: $\alpha = 75^\circ$, $s = 5\mu\text{m}$, $c = 40\mu\text{m}$ and $h = 9\mu\text{m}$.	58
Figure 3.6	A mathematical model of micro-pillar surfaces.	59
Figure 3.7	(a) 3D plot of a single pillar, and (b) 3D Plot of a frustum pillar array by the mathematical model with input parameter: $\alpha = 75^\circ$, $s = 5\mu\text{m}$, $c = 40\mu\text{m}$ and $h = 9\mu\text{m}$.	60
Figure 3.8	Schematic diagram of the periodic micro-grooved pattern on PMMA surface.	61
Figure 3.9	Surface height maps and 2-D profiles of the micro patterns on PMMA surfaces with various groove width of (a) $5\mu\text{m}$, (b) $10\mu\text{m}$, (c) $15\mu\text{m}$, (d) $20\mu\text{m}$, (e) $25\mu\text{m}$, (f) $30\mu\text{m}$, (g) $35\mu\text{m}$, (h) $40\mu\text{m}$, and (i) $45\mu\text{m}$ by Alicona InfiniteFocus (50x).	63
Figure 3.10	2-D profiles of the micro patterns on PMMA surfaces with (a) $9\mu\text{m}$ depth, $10\mu\text{m}$ width, $5\mu\text{m}$ distance between grooves,	69

	and (b) 9 μ m depth, 20 μ m width, 5 μ m distance between grooves.	
Figure 3.11	A water droplet suspended on a surface with periodic micro-grooved pattern.	70
Figure 3.12	Static contact angle as a function of geometric parameters of the micro patterns on PMMA surfaces with different groove width values with 5 μ l volume. A dotted line represents the boundary of wetting transition.	71
Figure 3.13	Images of a 5 μ l water droplet in contact with PMMA surface with different groove width of (a) 5 μ m, (b) 10 μ m, (c) 15 μ m, (d) 20 μ m, (e) 25 μ m, (f) 30 μ m, (g) 35 μ m, (h) 40 μ m, and (i) 45 μ m captured in the direction perpendicular to that of grooves.	73
Figure 3.14	Optical images displayed from flat COC sample, micro-directional grooved COC sample, and micro-pillar COC sample (a) without light reflection, and (b) with light reflection.	77
Figure 4.1	Hardware configuration of UPRM: (a) A Precitech Freeform 705G UPRM machine, (b) a workpiece fixture, and (c) SEM images of a diamond facet cutting tool tip.	84
Figure 4.2	Schematic diagrams of cutting geometry by UPRM: (a) horizontal cutting, and (b) vertical cutting.	85
Figure 4.3	Tool path design of a micro directional grooved surface generation in sequence: (a) horizontal cutting on grooves, and (b) vertical cutting on ridges.	87

Figure 4.4	Tool path design of a micro pillar surface generation in sequence: (a) horizontal cutting on grooves, (b) horizontal cutting on grooves after a 90° turn of fixture, and (c) vertical cutting on ridges.	87
Figure 4.5	Cutting cycles of grooves on a workpiece in horizontal cutting strategy.	87
Figure 4.6	Surface topography of a micro directional grooved surface with material swelling.	89
Figure 4.7	Surface topographies of (a) the micro-directional grooved surface, and (b) the micro-pillar surface from the experiment.	90
Figure 4.8	Schematic illustrations of the wetted area A_w and the projected area of the wetted regions A_{proj} on (a) micro-grooved surfaces, and (b) micro-pillar surfaces.	92
Figure 4.9	Static contact angles of water droplets on (a) the flat surface, (b) the micro-grooved surface, (c) the micro-pillar surface, and (d) air pockets under the droplet on micro-patterned surface.	98
Figure 4.10	Anisotropy of a water droplet on (a) the flat surface, (b) the micro-grooved surface, and (c) the micro-pillar surface from the top view.	101
Figure 4.11	Water droplets acting on (a) the micro-grooved surface, and (b) the micro-pillar surface.	103
Figure 4.12	Snapshots of the advancing and the receding angle measurement on (a) the flat surface, (b) the micro-grooved surface, and (c) the micro-pillar surface.	104

Figure 4.13	Snapshots of water droplets acting on the inclined (a) flat surface, (b) micro-grooved surface in the parallel direction, and (c) micro-pillar surface.	108
Figure 5.1	Schematic diagrams of (a) cutting geometry of UPRM, and (b) micro-periodic grooved surface.	114
Figure 5.2	Surface topographies and SEM images of the directional grooved COC surfaces with (a) 15 μm , (b) 30 μm , and (c) 45 μm groove width and spacing.	116
Figure 5.3	Schematic illustrations of a droplet (a) completely wetting in the Wenzel regime, (b) partially wetting, (c) contacting the side wall of the grooves, and (d) pinned at the top of the ridges in the Cassie and Baxter regime on micro- directional grooved surfaces.	117
Figure 5.4	Images (left) and assumptions (right) of various droplet wetting states on droplet contact lines on micro- directional grooved COC surfaces.	119
Figure 5.5	Wetting phenomena of droplet contact lines on micro- directional grooved PMMA surfaces.	122
Figure 5.6	Representative static contact angles, θ plotted against the droplet deposition time on the sample surface with (a) 15 μm , (b) 30 μm , (c) 45 μm groove width and spacing in the parallel direction (left) and the orthogonal direction (right).	125
Figure 5.7	Images and schematics of a water droplet in contact with (a) flat COC surface, (b) 15 μm , (c) 30 μm , (d) 45 μm groove width and spacing of directional grooved COC surfaces	133

	captured from side and top views.	
Figure 5.8	Comparison of the static contact angles of water measured on grooved COC surfaces in the parallel and orthogonal direction to the Wenzel model as well as the Cassie and Baxter model.	134
Figure 5.9	Snapshots of a water droplet (a) under complete wetting on the flat surface, (b) under complete wetting on the 15 μ m grooved surface, (c) under partial wetting on the 15 μ m grooved surface, (d) under the Cassie-Baxter state on the 30 μ m grooved surface, and (e) contacting the side walls of the 45 μ m grooved surface during the sliding measurement in the parallel direction.	138
Figure 5.10	Receding contact lines of a droplet under partial wetting state after tilting a 90 degree on the 15 μ m grooved COC surface in (a) 5x magnification, and (b) 20x magnification.	140
Figure 6.1	Cutting geometry of UPRM, and the tool path design of surface generation in (b) micro-grooved surfaces, (c) micro-pillar surface, (d) micro-micro hierarchical G-G surface, (e) micro-micro hierarchical G-P surface by UPRM.	148
Figure 6.2	Surface topographies of (a) micro-grooves, (b) micro-pillars, (c) micro-micro hierarchical G-G structure I, (d) micro-micro hierarchical G-G structure II, and (e) micro-micro hierarchical G-P structures fabricated by UPRM. (Remarks: G-G = Groove-Groove, G-P = Groove-Pillar)	151
Figure 6.3	Static contact angles of 5 μ l water droplets on (a) micro-	153

	grooves, (b) micro-pillars, (c) micro-micro hierarchical G-G structure I, (d) micro-micro hierarchical G-G structure II, and (e) micro-micro hierarchical G-P structure.	
Figure 6.4	Sliding performance of water droplets on (a) flat surface, (b) micro-grooved surface, (c) micro-pillar surface, (d) micro-micro hierarchical G-G structure, and (e) micro-micro hierarchical G-P surface.	157
Figure 6.5	Configuration of (a) the EFCS system, (b) the cutting model, and (c) the vertical cutting mode (Zhu et al., 2015).	161
Figure 6.6	Surface topographies of irregular (a) micro-micro hierarchical G-G surface, and (b) micro-micro hierarchical G-P surface. fabricated by end-fly-cutting-servo diamond machining.	162
Figure 6.7	Static contact angles of 5 μ l water droplets on irregular (a) micro-micro hierarchical G-G surface, and (b) micro-micro hierarchical G-P surface.	163
Figure 6.8	The wetting process and the contact area of solid-air-liquid interface of a water droplet with (a) regular micro-micro hierarchical G-G structure, and (b) irregular micro-micro hierarchical G-G structure.	164
Figure 6.9	Sliding performance of water droplets on irregular (a) micro-micro hierarchical G-G surface, and (b) micro-micro hierarchical G-P surface.	165
Figure 6.10	Schematic diagrams of the multi-level design of (a) micro-micro hierarchical G-G structure III with one	167

	pattern, and (b) micro-micro hierarchical G-G structure IV with two patterns.	
Figure 6.11	Surface topographies of the multi-level design of (a) micro-micro hierarchical G-G structure III with one pattern, and (b) micro-micro hierarchical G-G structure IV with two patterns fabricated by ultra-precision vertical cutting.	169
Figure 6.12	Static contact angles of 5 μ l water droplets on the multi-level (a) micro-micro hierarchical G-G structure III with one pattern, and (b) micro-micro hierarchical G-G structure IV with two patterns, and (c) the air pockets formation between the water droplet and the structures.	171
Figure 6.13	Wetting models on the multi-level of (a) micro-micro hierarchical G-G structure III with one pattern, and (b) micro-micro hierarchical G-G structure IV with two patterns.	171
Figure 6.14	(a) Original image of a water droplet captured from the highest static contact angle of 161.5 $^{\circ}$ on a multi-level hierarchical G-G structure IV with two patterns, and (b) the image of the water droplet after contour fitting by software.	173
Figure 6.15	Droplet contact lines on (a) micro-micro hierarchical G-G structure III, and (b) micro-micro hierarchical G-G structure IV. (Remark: Left is focusing on the droplet contact line; Right is focusing on the structures.)	173
Figure 6.16	Sliding performance of water droplets on the multi-level	174

	(a) hierarchical G-G structure III with one pattern, and (b) hierarchical G-G structure IV with two patterns.	
Figure I-1	Precitech Freeform 705G Ultra-precision raster milling machine.	186
Figure II-1	Hitachi TM3000 Scanning Electron Microscope.	188
Figure III-1	Zygo Nexview™ 3D Optical Surface Profiler.	190
Figure IV-1	Alicona IFM G4 3D Optical Surface Profiler.	192
Figure V-1	Olympus BX40 Optical Microscope.	194
Figure VI-1	Sindatek Model 100SB Video-based Optical Contact Angle Meter.	195

List of Tables

Table 3.1	Cutting conditions.	62
Table 3.2	Measured dimensions of micro patterns with 9 μ m depth, various widths and 5 μ m distance between grooves by Alicona InfiniteFocus (50x).	64
Table 3.3	Static contact angle (\pm SD) of PMMA surfaces without machining.	67
Table 3.4	Static contact angle (\pm SD) of micro-patterned PMMA surfaces measured in the direction along the grooves.	68
Table 3.5	Length of water droplet elongation (\pm SD) along the grooves of micro patterns on PMMA surfaces measured.	72
Table 3.6	Comparison between the material properties of COC and PMMA.	76
Table 3.7	Optical performance of micro-patterned COC surfaces.	78
Table 4.1	Cutting conditions.	84
Table 4.2	Measured geometrical parameters of micro-patterned COC surfaces.	91
Table 4.3	Wetting performance of the micro-patterned COC surfaces.	98
Table 5.1	Cutting conditions.	115
Table 5.2	Measurement data of surface geometries on micro-directional grooved surfaces.	115
Table 5.3	Deionized water contact angle data on micro-directional grooved COC surfaces.	131
Table 6.1	Cutting conditions.	147
Table 6.2	Measured geometrical parameters of micro-patterned COC	152

surfaces.

Table 6.3	Wetting performance of the micro-patterned COC surfaces.	154
-----------	--	-----

Chapter 1 Introduction

1.1 Background of Research

Over the last few years, biomimetic structures, such as lotus leaf and butterfly wing-like structures with self-cleaning properties, have been widely investigated due to their extensive potential applications (Nishimoto et al., 2013; Bixler et al., 2012). In nature, leaf surfaces of many different plants are superhydrophobic and exhibit extreme water-repellence. Such repellence can be applied to provide an artificial surface with certain self-cleaning properties (Nishimoto et al., 2013; Xia et al., 2012; Bhushan et al., 2011). Self-cleaning implies that dirty water droplets due to the characteristics of superhydrophobicity can easily roll off the surface and thus effectively prevent dirt from being suspended from it. These surfaces can be used in many fields such as the next generation of vehicle windshields, exterior paint for buildings, and solar panels.

Most of the research has focused on developing various material substrates with low surface energy, such as fluorocarbons and silicones, establishing different production methods to achieve surfaces with self-cleaning properties, and investigating major factors affecting the self-cleaning properties. Referring to the basis of the lotus effect, the superhydrophobicity of a surface can be enhanced

through designing and machining micro-patterns onto it. Numerous fabrication methods for self-cleaning surfaces, such as lithography (Murakami et al., 2014; Zhao et al., 2011), laser etching (Chen et al., 2013; Li et al., 2012), chemical reaction (Tanaka et al., 2013; Levkin et al., 2009), electrospinning (Ahmed et al., 2013; Han et al., 2009), and self-assembly (Li et al., 2011) have been proposed by various researchers in the last few years. However, most of the manufacturing processes involve complicated chemical treatment, are time-consuming, are not suitable for fabricating large surfaces, do not consider optical performance, or are only applicable to certain engineering materials such as metals, semiconductors, and alloys but are limited in regard to plastics. Sliding performance of hydrophobic micro-patterned surfaces is one of the major factors determining wettability (Lv et al., 2010; Miwa et al., 2000). However, there are very few one-step manufacturing methods capable of fabricating bare hydrophobic micro-patterned surfaces with good sliding performance and optical properties for mass production.

The existence of air under a droplet on hydrophobic micro-patterned surfaces is governed by the Cassie and Baxter state and is an essential element to achieve self-cleaning properties (Bhushan et al., 2011; Jung et al., 2009). Traditionally, the verification of a droplet wetting state is only capable of identifying complete wetting, and composite wetting states on isotopic micro-patterned surfaces. These

mainly rely on several approaches such as the observation of droplet from the front view (Yong et al., 2014; Li et al., 2010; Jung et al., 2007; Chen et al., 2005) or bottom view (Murakami et al., 2014; Park et al., 2009) captured by optical microscopy, or a comparison between the static contact angle measured by experiment and the calculation value from the Wenzel equation as well as the Cassie and Baxter equation (Zhao et al., 2012). The most commonly used method is to observe the existence of air under the droplet on the sample surface from the front view image. However, both the Cassie and Baxter state and partial wetting consist of solid-liquid-air interfaces which are under composite states. In other words, the existence of air under the droplet shown in the front view image can only prove that the droplet consists of solid-liquid-air interfaces but cannot verify that the droplet is governed by the Cassie and Baxter state or partial wetting during the wetting transition. This shows that traditional verification methods of a droplet wetting state is only capable of identifying complete wetting, and composite wetting states on isotopic micro-patterned surfaces but cannot verify intermediate wetting states. The limitation further leads to an incomplete understanding of the influence of intermediate wetting states on the sliding performance of the water droplet.

From the foregoing discussion, it can be concluded that better recognition of

wetting characteristic of bare hydrophobic micro-patterned surfaces with good sliding performance and optical properties fabricated from a one-step manufacturing method of advanced self-cleaning surfaces for mass production is needed. In addition, a characterization method of droplet wetting states on micro-patterned surfaces which facilities to illustrate the influence of intermediate wetting states on the sliding performance of the water droplet is lacking.

1.2 Research Objectives and Significance

This research explores the wetting characteristics and optical performance of bare surface geometries fabricated by ultra-precision machining. It also develops a characterization method of intermediate wetting states on micro-patterned surfaces based on the contact line of the droplet contour. The specific objectives of this research work are:

- (i) To develop an optimization model of surface geometries for self-cleaning surfaces, with consideration of the wetting performance and optical function;
- (ii) To investigate the wetting characteristics of bare micro-patterned surfaces with good sliding performance, using ultra-precision machining, for mass production;
- (iii) To propose a characterization method to identify various droplet wetting states, especially the intermediate wetting states, on micro-patterned

surfaces; and

- (iv) To study the anisotropic wetting behavior of micro-micro hierarchical structures fabricated by ultra-precision machining.

This research is meaningful since the optimization model of surface geometries strikes a balance between the wetting performance and optical function. This will allow the optimal set of parameters of bare biomimetic structures for advanced self-cleaning surfaces to be determined prior to the actual production by the one-step ultra-precision machining methods needed for mass production. In addition, the new characterization method of the droplet wetting states by the droplet contact line can identify the sliding conditions of the immediate wetting states on the micro-patterned surfaces. This provides more flexibility for the design of advanced self-cleaning surfaces which have great potential in applications for microfluidic devices.

1.3 Organization of the Thesis

This thesis consists of seven chapters. The first chapter gives a brief description of the research background, objectives and significance. Chapter 2 gives a systematic review on the related topics of this research study including an overview of the biomimetic self-cleaning industry, categories of superhydrophobic surfaces in nature, fabrication technologies of superhydrophobic surfaces,

development of ultra-precision machining technologies using single-point diamond turning assisted by fast-tool-servo, ultra-precision raster milling, and ultra-precision grinding, major factors affecting self-cleaning performance, characterization of droplet wetting states, and modeling and optimization approaches of wetting performance. Chapter 3 introduces a methodology for the optimization model of biomimetic structures for self-cleaning with consideration of the optical function in detail. Chapter 4 studies the wetting characteristics of bare hydrophobic micro-patterned surfaces machined by a highly controllable one-step mechanical machining method, UPRM, which is potentially capable of manufacturing bare hydrophobic micro-patterned surfaces with good sliding performance for mass production in plastic injection molding. Chapter 5 proposes a characterization method which can identify various wetting states including partial wetting, droplet contact with the side walls of the grooves, complete wetting, and the Cassie and Baxter state from observation of the droplet contact line. After the verification of various wetting states, the influences of the intermediate wetting states including partial wetting and droplet contact with the side walls of the grooves on anisotropic sliding performance of water droplet are investigated. Chapter 6 investigates the anisotropic wetting behavior of micro-micro hierarchical structures fabricated by ultra-precision machining. Finally, Chapter 7

draws overall conclusions of the whole study, and provides some recommendations for future work.

Chapter 2 Literature Review

2.1 Overview of Biomimetic Self-cleaning Industry

Over the past few decades, scientists have expressed growing interest in the investigation of self-cleaning surfaces inspired by biological aspects. Biomimetic structures such as lotus leaves, rice leaves, cicada wings, and butterfly wing-like structures with self-cleaning properties have been investigated widely due to their extensive potential applications. In nature, leaf surfaces of many different plants and insect wing surfaces are superhydrophobic, anisotropic wetting, anti-reflection, low adhesion, low drag, and directional adhesion surfaces (Nishimoto and Bhushan, 2013). Such functions, structures, and principles can be applied to manufacture artificial surfaces with certain self-cleaning properties with extreme water-repellence (Celia et al., 2013; Nishimoto and Bhushan, 2013; Bixler and Bhushan, 2012; Bhushan and Jung, 2011). The potential applications of these surfaces cover extensive fields such as the next generation of car rear mirrors, vehicle windshields, exterior paint for buildings, and solar panels, as shown in Figure 2.1.



Figure 2.1 Potential applications of self-cleaning surfaces.

Self-cleaning implies that water droplets can easily roll off from a surface and thus effectively prevents dirt from being suspended from it by the action of water. The possible elements challenging the self-cleaning surfaces include water (i.e. deionized water, salt water and ice), moisture, oil, and dust (i.e. water-soluble non-metal, oil-soluble non-metal, water-insoluble non-metal, and metal) as shown in Figure 2.2.



Figure 2.2 Possible elements challenging self-cleaning surfaces.

From recent research progress, bioinspired self-cleaning surfaces are mainly divided into three categories: superhydrophobicity, superhydrophilicity, and superoleophobicity as shown in Figure 2.3 (Nishimoto and Bhushan, 2013). Each category is inspired by different self-cleaning surfaces with various properties found in nature. Superhydrophobic surfaces refer to those surfaces which achieve a high static contact angle (CA) above 150° . When a water droplet starts to move downwards on a surface tilted at a specific angle, the angle is defined as the tilting angle (TA). The tilting angle is roughly equal to the contact angle hysteresis (CAH) given by the difference of the CA at the front of the moving droplet (advancing CA) and the CA at the back of the moving droplet (receding CA). The CAH relates to the energy required to move a droplet on a surface. A low CAH normally below 10° is desirable for a self-cleaning surface (Marmur, 2004). Most of the research has mainly focused on developing various material substrates with low surface energy, such as fluorocarbons and silicones, or establishing different production methods to achieve surfaces with self-cleaning properties. Referring to the basis of the lotus effect, the superhydrophobicity of a surface can be enhanced through designing and machining micro-patterns or hierarchical structures onto it, besides modifying the materials by chemistry.

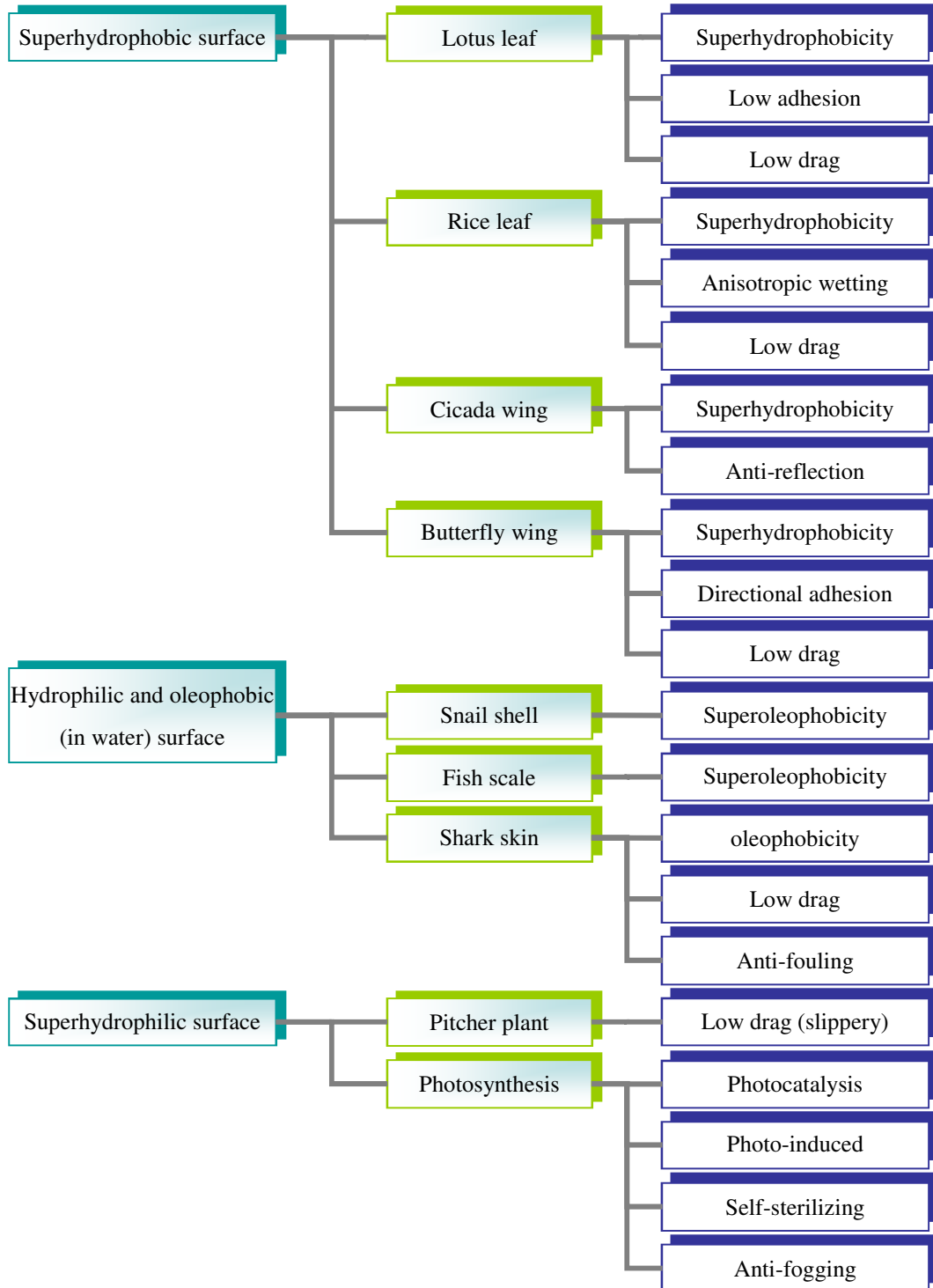


Figure 2.3 Categories of self-cleaning surfaces (Nishimoto and Bhushan, 2013).

2.2 Categories of Superhydrophobic Surfaces in Nature

2.2.1 Lotus Leaf

In nature, the leaf surface of a lotus plant (*Nelumbo nucifera*) possesses superhydrophobicity, low adhesion, and low drag properties. Figure 2.4 shows that front surface of a lotus leaf possesses random hierarchical micro-nanostructures and a layer of nano-hair in wax which can achieve a very high static contact angle of over 160° and a very low tilting angle of less than 5° with a water droplet. Wang et al. (2009) found that the average height, width and distance between micro-pillars on the front surface of a fresh lotus leaf are $15\mu\text{m}$, $7\mu\text{m}$ and $20\mu\text{m}$ respectively. Cheng et al. (2006) found that if the nano-scale, hair-like structures are melted by heating at 150°C , while keeping the chemical composition of the surface approximately the same, the contact angle of the water droplet is dramatically reduced by altering the roughness only. It can therefore be proven that the superhydrophobic state of a lotus leaf is a result of the combined effect of the hierarchical surface structure with entrapped air under a water droplet and the hydrophobicity of the surface wax. This shows that both the multi-leveled roughness and the hydrophobic nature of a low surface energy material are important in achieving surfaces with a high static contact angle, a low sliding angle and a self-cleaning effect.

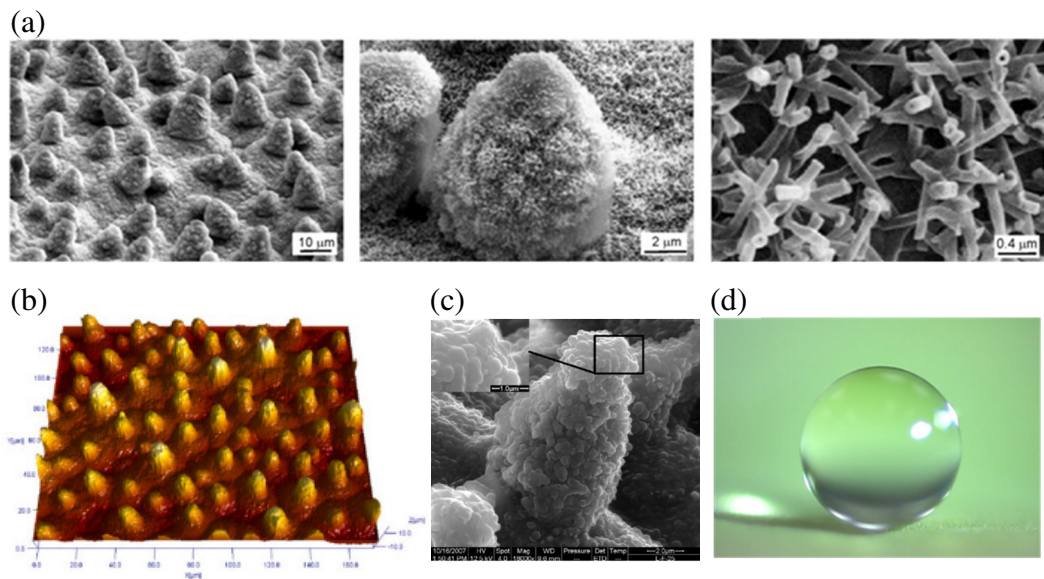


Figure 2.4 (a) SEM images of the front surface of the lotus leaf with hierarchical micro-nanostructures (Bhushan et al., 2009), (b) hierarchical micro-nanostructures shown in surface height map (Cheng et al., 2006), (c) an enlarged SEM image of a micro-pillar with nano-hair in wax (Cheng et al., 2006), and (d) a water droplet on the front surface of the lotus leaf (Bhushan et al., 2009).

2.2.2 Rice Leaf

The rice leaf is a natural surface which possesses superhydrophobic, anisotropic wetting and low drag properties. Figure 2.5(a) shows an image of a water droplet rolling in a direction parallel to the edge of the rice leaf. According to the SEM images shown in Figure 2.5(b) and (c), the rice leaf surface consists of directional micro- and nanostructures, and papillae, with average diameter of approximately 5-8 μm , arranged in order (Gao and Liu, 2007). Wu et al. (2010) reported that the water static contact angle measured along and perpendicular to the direction of the rice leading edge were $153^\circ \pm 3^\circ$ and $146^\circ \pm 2^\circ$ respectively.

Due to the anisotropic arrangement of the papillae on the rice leaf surface, water droplets can easily roll off along the direction of the rice leaf edge. Gao and Liu (2007) reported that the tilting angle of the parallel and perpendicular directions to the rice leaf edge were 4° and 12° respectively. It is believed that the anisotropic wettability of the rice leaf surface enhances the self-cleaning efficiency when the water droplets pick up contamination during the sliding process on the surface. The reason is that a water droplet can roll off to the edge of the leaf without dropping off of the leaf. All of these effects have attracted researchers to investigate anisotropic wettability using different fabrication methods (Yong et al., 2014; Liu et al., 2013; Wu et al., 2011; Zhang et al., 2010; Yang et al., 2010). Furthermore, Bixler and Bhushan (2012) suggested that a superhydrophobic surface with anisotropic grooves should give low fluid drag.

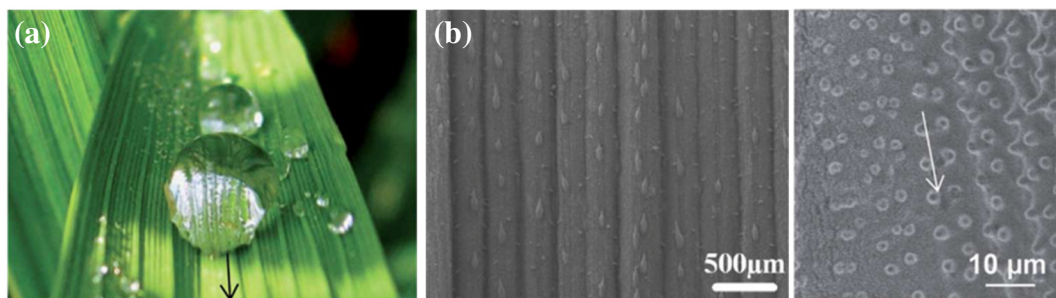


Figure 2.5 (a) A water droplet on the front surface of the rice leaf, and (b) the hierarchical micro-nanostructures on the rice leaf shown in SEM image (Bixler and Bhushan, 2012).

2.2.3 Cicada Wing

The wing surface of a cicada is an external insect surface which is superhydrophobic, and anti-reflective in nature. Figure 2.6 shows a SEM image and the surface height maps of the cicada wing surface, which consists of closely packed nano-pillars with pitch values ranging from 110nm to 140nm (Lee et al., 2004; Watson et al., 2008), and heights of the pillars ranged from 225nm to 250nm. Due to the waxy coating of the pillars and the nano-scale array, cicada wing surfaces show superhydrophobicity with a static contact angle of 160° (Malm et al., 2010). According to the AFM analysis reported by Watson et al. (2008), it was revealed that particle adhesion on the cicada wing surface is extremely small when compared to that on a flat hydrophilic silica surface. Similar to the lotus effect, contaminants on the surface can be easily removed by moving water, or even wind blasts. Besides the superhydrophobic, low adhesion, and self-cleaning properties, the nano-array structures on the cicada wing give an antireflection property which may protect cicadas from predators (Watson et al., 2008). The combination of the antireflection and self-cleaning properties could be suitable for solar cell applications in which the surfaces are required to be transparent and clean for the utilization of solar light.

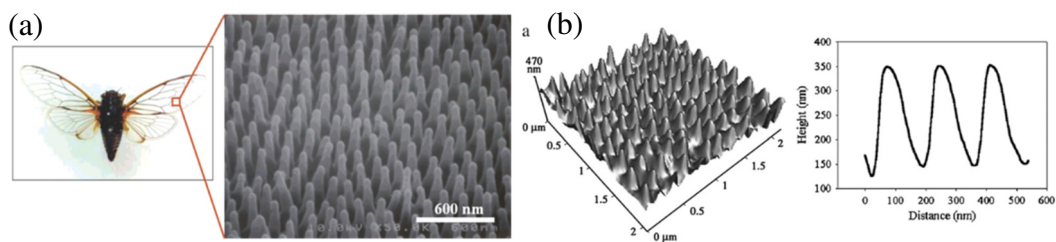


Figure 2.6 (a) SEM image of cicada wing (Lee et al., 2004), and (b) AFM image and the cross section profile of the nanostructures on cicada wing (Watson et al., 2008).

2.2.4 Butterfly Wing

A butterfly wing surface is a multifunctional insect wing which includes structure coloring (Gu et al., 2003), fluorescence emission functions, (Vukusic and Hooper, 2005) and chemical sensing capability (Vukusic and Sambles, 2003), as shown in Figure 2.7(a). With respect to self-cleaning properties, it has been reported that the water static contact angle was $152^\circ \pm 2^\circ$ on the butterfly wing surface which shows directional adhesion properties due to the periodic arrangement of the overlapping micro-scales on the wings, and the fine lamella-stacking nano-stripes on the scales along the RO direction, as shown in Figure 2.7(b) and (c) (Bixler and Bhashan, 2012; Wanger, T.; Zheng et al., 2007; Neinhuis et al., 1996). Droplets start to roll off from the surface in the RO direction at a tilting angle of approximately 9° but are pinned on the tilted upright wing surface when the tilting direction is against the RO direction, as shown in Figure 2.7(d). This shows that the difference between the anisotropic wettability of the butterfly

wing and the rice leaf, where one-dimensional anisotropic wetting occurs on the butterfly wing, while two-dimensional anisotropic wetting occurs on the rice leaf due to their unique arrangements of the micro- and nano-structures.

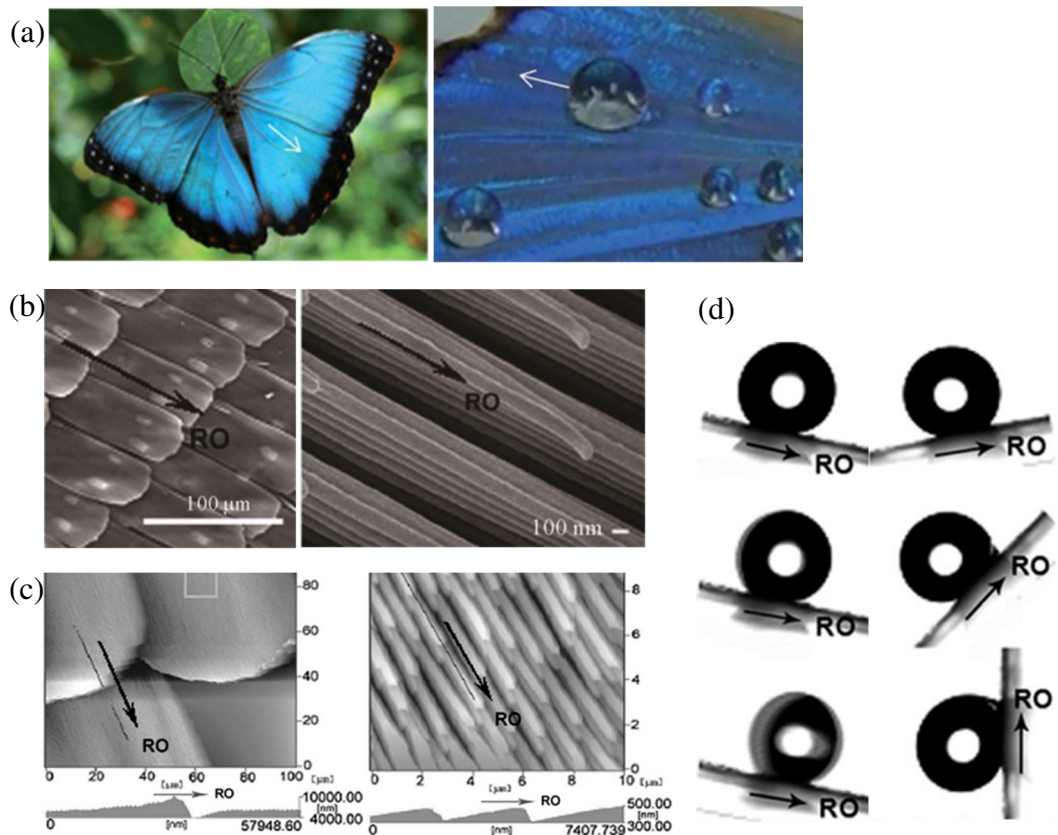


Figure 2.7 (a) Water droplets on a blue butterfly wing (Bixler and Bhushan, 2013), (b) SEM images of the hierarchical micro- and nano-structures on the surface of the butterfly wings (Zheng et al., 2007), (c) AFM images of the overlapping micro-scales and nano-stripe structures (Zheng et al., 2007), and (d) Water droplets are tilted along and against the RO direction (Zheng et al., 2007).

2.3 Fabrication Technologies of Superhydrophobic Surfaces

Microstructures in nature, such as the surfaces of leaves and insect wings, have micro-patterned surfaces that have hydrophobic properties (Bixler and

Bhushan, 2012; Byun et al., 2009; Zheng et al., 2007). These hydrophobic surfaces have great potential in applications for biomimetic self-cleaning surfaces, such as the next generation of vehicle windshields, exterior paint for buildings, and solar panels, due to their extreme water repellence (Nishimoto and Bhushan, 2013; Xia et al., 2012; Bhushan and Jung, 2011). Recent studies have focused on the fabrication of hydrophobic surfaces using various methods such as lithography (Murakami et al., 2014; Zhao et al., 2012; Oner and McCarthy, 2000; Ma and Hill, 2006;), plasma treatment after lithography (Park et al., 2012), electrochemical anodization (Xiao et al., 2015), laser processing (Yong et al., 2014; Rukosuyev et al., 2014; Chen et al., 2013; Li et al., 2012), sol-gel coating (Liu et al., 2015; Rao et al., 2009), chemical reaction (Tanaka et al., 2013; Levkin et al., 2009; Pozzato et al., 2006; Zhang et al., 2008), electrospinning (Ahmed et al., 2013; Huang et al., 2010; Han and Steckl et al., 2009; Ma et al., 2005), self-assembly (Yang et al., 2013; Li et al., 2011), and molding using templates (Greiner et al., 2009; Jeong et al., 2009), as shown in Figure 2.8.

Most of the manufacturing processes are complicated in chemical treatment, time-consuming, unsuitable for fabricating large surfaces, or only applicable to certain engineering materials such as metals, semiconductors, and alloys but limited with plastics. Most researchers reported the manufacturing methods and

ended up merely with detailed results of their contact angle measurement on the sample surfaces. This shows that extensive research on superhydrophobicity has been collecting data for the sake of manufacturing rather than to grasp a thorough understanding of the mechanism of self-cleaning taking place behind the scenes.

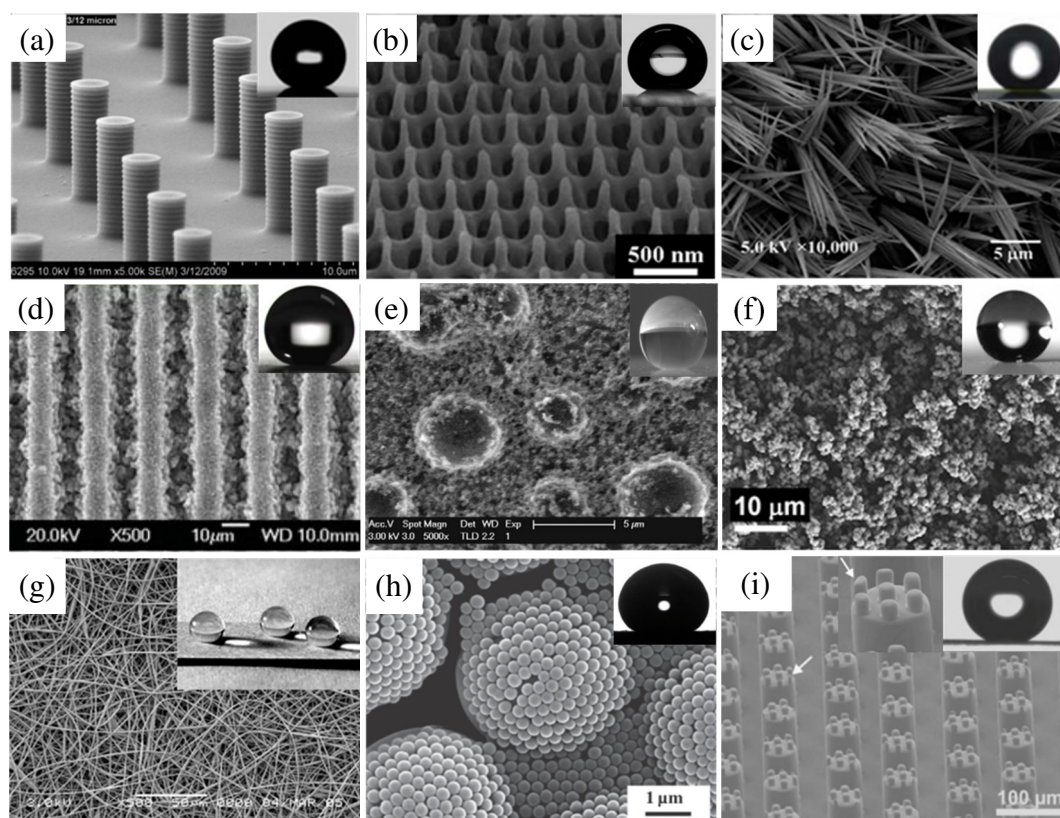


Figure 2.8 Superhydrophobic surfaces fabricated by (a) Lithography (Zhao et al., 2012), (b) Plasma treatment after lithography (Park et al., 2012), (c) Electrochemical anodization (Xiao et al., 2015), (d) Laser processing (Yong et al., 2014), (e) Sol-gel coating (Rao et al., 2009), (f) Chemical reaction (Levkin et al., 2009), (g) Electrospinning (Ma et al., 2005), (h) Self-assembly (Yang et al., 2013), and (i) Molding using template (Greiner et al., 2009).

Cheng et al. (2006) argue that few experimental investigations have focused on the chemical composition and surface structure of superhydrophobic surfaces. Guo et al. (2011) revealed that creating superhydrophobic surfaces is not just simply about copying or duplicating biological structures. To this end, recent studies have begun investigating what critical factors influence the self-cleaning properties (Marmur, 2004; Martines et al., 2005; Cheng et al., 2006; Wang et al., 2009). All of these qualitative studies advocate that entrapped air formed in asperities, the shape and curvature of the edges of the asperities, and the surface energy of materials are the critical factors influencing the contact angle. Sliding performance of hydrophobic micro-patterned surfaces is one of the major issues determining wettability (Lv et al., 2010; Miwa et al., 2000). However, there are very little one-step manufacturing methods capable of fabricating bare hydrophobic micro-patterned surfaces with good sliding performance suitable for mass production.

Mechanical machining would be one of the best solutions to fabricate bare hydrophobic micro-patterned surfaces with good sliding performance for mass production due to the numerical control of the machine tool path during the material removal process. Ultra-precision machining such as single-point diamond turning (SPDT), assisted by a fast-tool-servo, ultra-precision grinding (UPG), and

ultra-precision raster milling (UPRM), are capable of manufacturing micro-patterned surfaces with sub-micrometer form accuracy and nanometer surface roughness, without subsequent processes. Although fast-tool-servo diamond turning is capable of generating different micro-patterned arrays, the aspect ratio of the generated micro-patterned arrays is relatively low (Yu et al., 2011). It is difficult for droplets on these micro-patterned arrays to form a composite solid-liquid-air interface which is essential for hydrophobic surfaces to achieve self-cleaning properties (Bhushan and Jung, 2011). Li et al. (2014) recently reported a mechanical micro-grinding method to fabricate hydrophobic micro-V-grooved Si surfaces. However, the geometrical dimensions of the micro-V-grooves are not very controllable and this method can only be applied to the machining of certain engineering materials such as metals, alloys, or ceramics, but not plastics. UPRM has been conventionally applied to machine mold inserts for F-theta lenses, V-groove structures for fiber array connectors, and other optical freeform surfaces. It takes advantage of manufacturing both the bare hydrophobic micro-patterned surface and its mold insert for mass production in plastic injection molding. This greatly reduces the cost and time for manufacturing hydrophobic micro-patterned surfaces. It is known that a sample surface with a high static contact angle with a water droplet does not mean that it has good droplet mobility (Gao and McCarthy,

2009). Although Kong et al. (2012 and 2013) proposed a framework for the design, fabrication, and characterization of three dimensional patterned micro-structured surfaces with a high static contact angle of water on hydrophilic materials, both the fabrication details and the wettability of the machined micro-patterned surfaces are still incomplete. Thus, there is still a lack of a highly controllable fabrication method for bare micro-patterned surfaces with good sliding performance for mass production.

2.4 Development of Ultra-precision Machining Technologies

2.4.1 Single-point Diamond Turning (SPDT)

Single-point diamond turning (SPDT), assisted by fast-tool-servo as shown in Figure 2.9(a), is an ultra-precision process employing a single crystal diamond cutting tool which possesses a nanometric edge radius, form reproducibility and wear resistance (Ikawa et al., 1991). The diamond tool shown in Figure 2.9(b) is used to machine non-ferrous materials like aluminum, copper alloy and plastic. This technology is able to manufacture components with sub-micrometer form accuracy and surface roughness in the nanometer range (Cheung et al., 2001). The current applications include the manufacture of mould inserts for injection moulding used in plastic camera lenses, F-theta lenses in scanners, and back-light

lenses for LED arrays, etc. Different kinds of spherical, aspheric, and freeform surfaces can be generated by using different values of spindle speed, feed rate, depth of cut, and tool nose radius. Although fast-tool-servo diamond turning is capable of generating different micro-patterned arrays, the aspect ratio of the generated micro-patterned arrays is relatively low (Yu et al., 2011). It is difficult for droplets on these micro-patterned arrays to form a composite solid-liquid-air interface which is essential for hydrophobic surfaces to achieve self-cleaning properties (Bhushan and Jung, 2011).

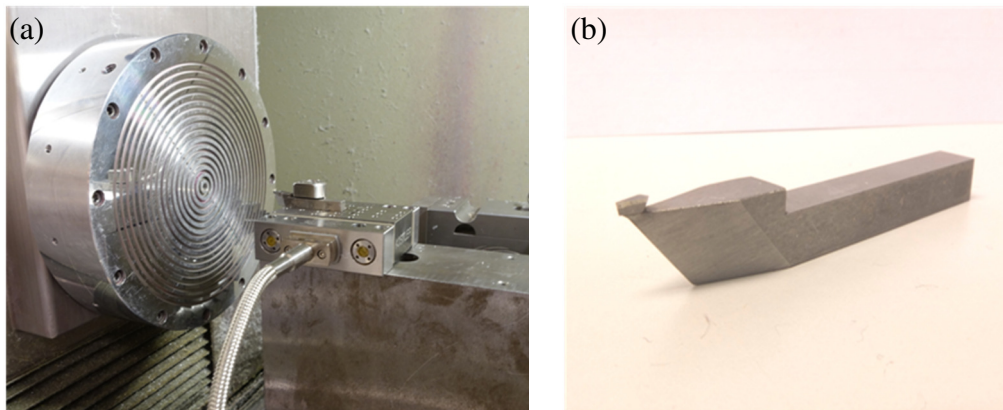


Figure 2.9 (a) Single-point diamond turning, and (b) Single crystal diamond tool.

2.4.2 Ultra-precision Grinding (UPG)

Ultra-precision grinding (UPG) is a mechanical machining process using different types of grinding wheels with dressing which can generate components made in difficult-to-machine materials such as silicon, silicon carbide, tungsten carbide, ceramics, and stainless steels with high form accuracy, low surface

roughness, and good surface integrity (Zhang et al., 2015; Bletek et al., 2013; Suzuki et al., 2012; Agarwal and Rao, 2008). The components are generally applied in the electronics, aeronautics and optical industries. Li et al. (2014) recently reported a mechanical micro-grinding method to fabricate hydrophobic micro-V-grooved Si surfaces. However, the geometrical dimensions of the micro-V-grooves are not very controllable and this method can only be applied to the machining of particular engineering materials such as metals, alloys, or ceramics, but not plastics. An ultra-precision grinding machine is as shown in Figure 2.10.

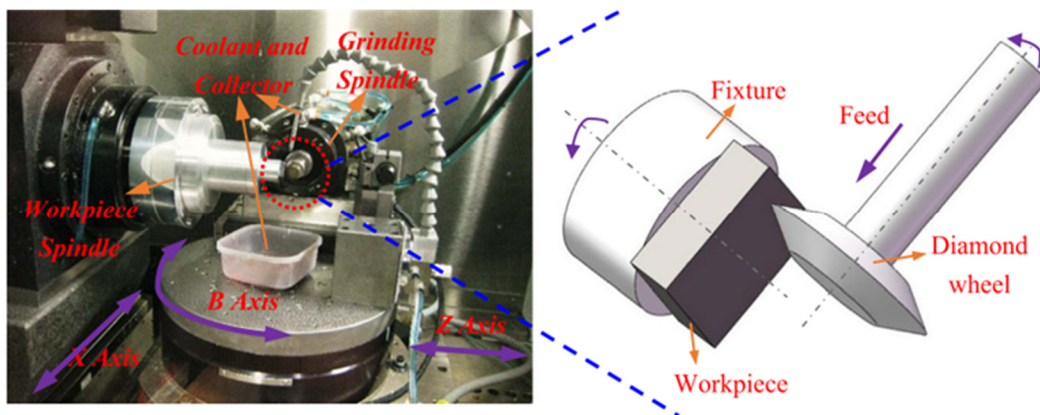


Figure 2.10 Ultra-precision grinding (Zhang et al., 2015).

2.4.3 Ultra-precision Raster Milling (UPRM)

Ultra-precision raster milling (UPRM) can be used to replicate biomimetic structures at various micro scales. This technology is used to generate non-rotational symmetrical freeform optical surfaces with form accuracy in the submicrometre range and surface finish in the nanometer range, without the need

for subsequent polishing. The machine tool has a mono-crystal diamond which is usually employed for machining non-ferrous materials such as aluminium and copper. There are various shapes of diamond tools, such as round shape with a tool nose radius, acute shape with a rake angle, or faceted shape with a tool width controlled by a five axis CNC machine, as shown in Figure 2.11.



Figure 2.11 Ultra-precision raster milling.

Due to the geometrical complexity, the surface generation mechanism of raster milling is different from that of single-point diamond turning. A machined surface manufactured from raster milling is able to create different freeform optical components as well as different shapes of groove with various dimensions. Conventionally, UPRM has been applied to machine mold inserts for F-theta lenses, V-groove structures for fiber array connector, and other optical freeform surfaces. It takes advantage of manufacturing both the bare hydrophobic micro-patterned surface and its mold insert for mass production in plastic injection

molding. This greatly reduces the cost and time for manufacturing hydrophobic micro-patterned surfaces. In addition, this also fosters ease of control in the dimensions of the micro-patterns in investigating the influence of ultra-precision machined patterns on wetting transition. Three different ultra-precision methods including SPDT, UPG and UPRM have been compared as shown in Table 2.1. It is shown that UPRM is better to fabricate micro-patterns in plastics with high precision in geometrical dimensions and relatively high aspect ratio.

Table 2.1 Comparison between different ultra-precision machining methods.

Method	Advantages	Limitations
Single-point diamond turning (SPDT), assisted by fast-tool-servo	<ul style="list-style-type: none"> • Capable of machining non-ferrous materials • Capable of generating different micro-patterned arrays 	<ul style="list-style-type: none"> • Not capable of generating micro-patterned arrays with relatively high aspect ratio
Ultra-precision grinding (UPG)	<ul style="list-style-type: none"> • Capable of machining metals, alloys, or ceramics • Capable of generating micro-patterned arrays with relatively high aspect ratio 	<ul style="list-style-type: none"> • Not capable of machining plastics • Not capable of generating micro-patterns with very controllable geometrical dimensions
Ultra-precision raster milling (UPRM)	<ul style="list-style-type: none"> • Capable of machining non-ferrous materials and plastics • Capable of generating micro-patterns with high precision in geometrical dimensions • Capable of generating micro-patterned arrays with relatively high aspect ratio 	<ul style="list-style-type: none"> • Relatively long machining time

2.5 Major Factors Affecting Self-cleaning Performance

2.5.1 Surface Geometry

Surface geometry is one of the major factors directly affecting the wetting behavior of a droplet on a rough surface. This relates to the formation of the solid-liquid or solid-liquid-air interfaces on a superhydrophobic surface for self-cleaning during wetting transition. Various wetting states, including complete wetting, partial wetting, and composite wetting, can be formed by the surface geometry during wetting transition of the rough surface. A multi-roughness surface formed by the hierarchical micro-nano structures on lotus leaves is one of the key factors to achieve self-cleaning properties by superhydrophobicity. The front leaf surface of a lotus plant (*Nelumbo nucifera*) is a natural hydrophobic surface which is a combination of micrometre-scale and nanometre-scale patterns, as shown in Figures 2.12 and 2.13.

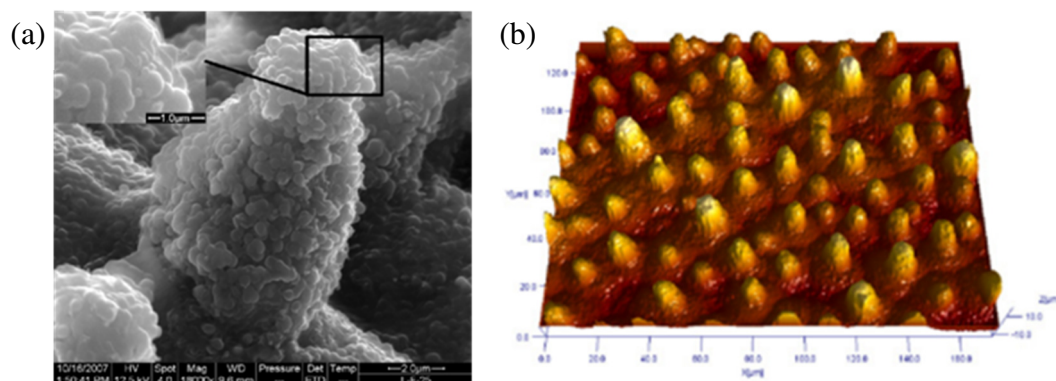


Figure 2.12 The front surface of the lotus leaf with nanometer structure shown in (a) SEM image and (b) surface height maps (Cheng et al., 2006).

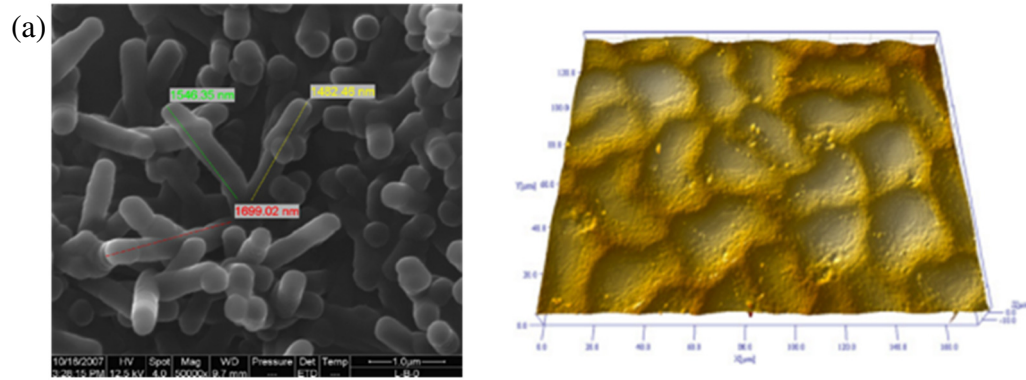


Figure 2.13 The back surface of the lotus leaf with nanometer structure shown by (a) SEM image and (b) surface height maps (Cheng et al., 2006).

Lotus leaves possess self-cleaning properties due to the superhydrophobicity of their front surfaces and the metastable position of the contact line (MPCL) of their back surfaces. Wang et al. (2009) found that the average height, width and distance between the micro-pillars on the front surface of a fresh lotus leaf are $15\mu\text{m}$, $7\mu\text{m}$ and $20\mu\text{m}$ respectively. Cheng et al. (2006) proved that intricate surface structures with a low surface energy material leads to a high static contact angle, a low sliding angle and a self-cleaning effect. Jung and Bhushan (2006) found that without hydrophobic coatings such as perfluorodecyltriethoxysilane (PFDTES), single-layer nanopatterned PMMA surfaces manufactured by soft lithography achieved a static contact angle of less than 90° due to its intrinsic hydrophilic surface. Bhushan et al. (2008) investigated the effect of the surface geometry of superhydrophobic patterned surfaces on the contact angle of a water droplet. It was found that increasing the roughness of the hydrophobic surface

increases its contact angle with water. Although micro-patterned surfaces have a higher roughness factor than nano-patterned surfaces, both single-layer structures have a similar contact angle due to the benefit gained from the air pocket formation under the droplet. Besides, multi-layer structures such as micro-nano and micro-micro hierarchical structures can further increase the static contact angle of water droplets and induce more energy barriers for wetting transition when compared with that on the single-layer structure, such as a micro- or nano-patterned surface.

2.5.2 Materials

Surface energy is regarded as the interaction between the cohesion force of the liquid molecules and the adhesion force of the liquid on the material surface. In other words, the surface energy determines whether spreading of a liquid over a surface will occur. Different liquids have various cohesion forces due to molecular bonding. The adhesion force of a liquid on a material surface will also be affected by the surface chemistry (i.e. molecular bonding among surface material). As a result, low surface energy materials such as fluorocarbons or silicones are widely employed in different manufacturing methods for the fabrication of self-cleaning surfaces (Yabu et al., 2005; Xu et al., 2005; Khorasani et al., 2005; Sun et al., 2005; Ma et al., 2005). Without any structures on a flat

material surface, the highest static contact angle of a water droplet reported is around 120° on a fluorinated material. Chemical vapor deposition, sol-gel coating, and spray-coating are some commonly used fabrication methods to manufacture hydrophobic surfaces for self-cleaning applications. However, most of these manufacturing processes are complicated in the chemical treatment, time-consuming, or not suitable for fabricating large surfaces. Limited research has been undertaken on investigating the influence of micro-patterned surfaces on the static contact angle measured on mediate hydrophobic materials which can also achieve self-cleaning properties.

2.5.3 Contact Area with Liquid

Surface geometry is one of the major factors determining the liquid contact area on a rough surface. Besides adding multi-roughness and changing the surface chemistry, minimizing the contact area between the solid and liquid interface is one of the methods to increase the static contact angle of the liquid on the solid surface, according to the Cassie-Baxter regimen. The prediction of the static contact angle using the contact area in the Wenzel, and the Cassie-Baxter models, is only valid to the extent that the structures in the contact area reflect the ground-state energies of the contact lines and the transition states between them (Gao and McCarthy, 2007). Bhushan et al. (2008) claims that on increasing the tip radius of

hydrophilic materials, the adhesion force increases due to the increased contact area between the tip and liquid surface. Meniscus force has a contribution in this situation. On the other hand, the adhesive force of a water droplet on a hydrophobic materials increases due to the increased contact area, but not meniscus force. Cheng et al. (2006) proved that without the nano-scale hair like structures, the surface of a lotus leaf is changed into a different roughness. Its contact angle with water decreases and water droplets do not roll off from the surface. However, researchers have not identified the wetting state conditions which contribute to the sliding performance on a hydrophobic surface. In addition, other factors such as the unbalanced contact area between the liquid and surface geometries have not been considered.

2.5.4 Droplet Contact Line

Wetting is an event involving the droplet contact line on a surface. With support of experimental data, Gao and McCarthy (2007) indicated that contact angle behavior, including advancing, receding and hysteresis, is determined by the interactions between the solid and the liquid at the three phase contact line alone, and it is irrelevant to the interfacial area within the contact perimeter. In other words, the Wenzel and Cassie theories are flawed within some of the regions, and they are only valid to the extent that the structures of the contact area reflects the

ground-state energies of the contact lines and the transition states between them. The contact angle and hysteresis are a function of the contact line structure and that the kinetics of droplet movement, rather than thermodynamics, dictates wettability. In other words, wettability including advancing and receding contact angles, and thus hysteresis, is a function of the activation energies that must be overcome in order for contact lines to move from one metastable state to another (Gao and McCarthy, 2009). It is important to know that the contact areas play no role in this case during the wetting process. In addition, it should be noted that the Wenzel and Cassie theories are incorrect in certain situations. As a result, it is necessary to characterize the wettability of a surface using advancing, receding and hysteresis, rather than only measuring the static contact angle.

2.6 Characterization of Droplet Wetting States

Micro-patterned surfaces have enormous potential in applications on artificial self-cleaning surfaces, such as the next generation of vehicle windshields, exterior paint for buildings, and solar panels (Sahoo and Kandasubramanian, 2014; Celia et al., 2013; Xia et al., 2012). It has become clear that the existence of air under a droplet governed by the Cassie and Baxter state on a hydrophobic micro-patterned surface is an essential element in achieving self-cleaning properties (Bormashenko, 2015; Bhushan and Jung, 2011; Bhushan et al., 2009). Different wetting states of

superhydrophobic surfaces, including the Wenzel state, the Cassie and Baxter state, the “Lotus” state, the transitional superhydrophobic state between Wenzel’s and Cassie’s states and the “Gecko” state, have been defined (Wang and Jiang, 2007). The petal effect refers to a water droplet on the structured surface, such as a red rose petal, with high static contact angle that cannot roll off, even when turned upside down due to the Cassie impregnating wetting state (Feng et al., 2008). Traditionally, verification of a droplet wetting state was only capable of identifying the Wenzel and the Cassie and Baxter regimes on isotopic micro-patterned surfaces. These mainly relied on a number of approaches such as observation of a droplet from the front (Yong et al., 2014; Li et al. 2010; Jung and Bhushan, 2007; Chen et al., 2005) or bottom views (Murakami et al., 2014; Park et al., 2009) captured by optical microscopy, or a comparison between the static contact angle measured experimentally and the calculated value from the Wenzel equation, as well as the Cassie and Baxter equation (Zhao and Law, 2012). The most commonly used method was to observe the existence of air under the droplet on the sample surface from the front view image. However, both the Cassie and Baxter state and partial wetting consist of solid-liquid-air interfaces which are in composite states. The main difference between these two regimes is that the Cassie and Baxter state is relatively stable due to the energy barrier resistance of the wetting transition

changing from the Cassie and Baxter regime to the Wenzel regime. However, in partial wetting a metastable state occurs during the wetting transition when the droplet partially penetrates into the grooves (Murakami et al., 2014; Ren, 2014; Song et al., 2015). In other words, the existence of air under the droplet, shown in the front view image, can only prove that the droplet consists of solid-liquid-air interfaces but not verify that the droplet is governed by the Cassie and Baxter state or is under partial wetting during transition. It is also difficult to directly observe the air existing between the droplet and the relatively small surface geometries. Although applying a light vibration on sample surfaces for measuring the most stable apparent contact angle might identify the difference between the Cassie and Baxter state and partial wetting (Merion et al., 2004; Marmur, 2006), this vibration actually is an external force which might overcome the energy barrier in wetting transition from the Cassie and Baxter regime to the Wenzel regime. Additionally, other traditional methods are either limited to transparent materials, by observing the bottom view of the sample, or are only based on the prediction from the calculation using the Wenzel model, as well as the Cassie and Baxter model. Thus, it is necessary to propose a better characterization method which is able to identify various wetting states, including the Cassie and Baxter state and partial wetting.

Observation of the droplet contact line may be one of the best solutions to

characterize the wetting states, especially the intermediate wetting states. Wetting behavior on isotropic surfaces is quite different from that on anisotropic surfaces (Zhao and Law, 2012; Cheng et al., 2016; Neuhaus et al., 2012). It is known that the wetting behavior is mainly governed by material factors (Neuhaus et al., 2012; Liu et al., 2015), the droplet contact line (Erbil 2014; Gao and McCathy, 2009; Gao and McCathy, 2007), and the surface geometries of the sample (Yong et al., 2014; Zhao et al., 2011; Ma et al., 2013; Rukosuyev et al., 2014; Davaasuren et al., 2014; Li et al., 2015). Surface geometry is therefore identified as one of the major factors affecting the wetting behavior, whereas the droplet contact line is important in determining wettability. It is found that there has been only limited research that focuses on investigation of the anisotropic wetting behavior of micro-directional grooved surfaces experimentally (Cheng et al., 2016; Ma et al., 2013; Li et al., 2015; Tanaka et al., 2013; Zhang et al., 2014; Jiang et al., 2015; Chen et al., 2011; Lee et al., 2013; Kooij et al., 2012), theoretically (Tie et al., 2015; Jansen et al., 2015) or by simulation modeling (Jiang et al., 2014; David et al., 2012; Jansen et al., 2012). The existence of a solid-air-liquid interface on the planar side walls of Polydimethylsiloxane (PDMS) microlines under a metastable state, during the wetting transition from the Cassie and Baxter regime to the Wenzel regime, has been recently proven (Luo et al., 2011). The derived theoretical relationships

indicated that the air-water interfaces might be stationary at the top corners and sidewalls of the microlines if the inclined angles of the microline sidewalls were less than 90° . Otherwise, the interfaces could only be stationary at the top corners of the microlines. However, there are very limited characterization methods capable of identifying that the droplet contacts the side walls of the grooves (Marmur, 2009). The limitation of the characterization of droplet wetting states further leads to an incomplete understanding of the influence of the intermediate wetting states, including partial wetting and droplet contact with the side walls of the grooves, on the sliding performance of the water droplet.

2.7 Modeling and Optimization Approaches

According to the literature, there are several conceptual models to illustrate the influence of roughness on hydrophobicity when a water droplet spreads and engulfs the surface topography of a flat or rough surface. The hydrophobicity of the sample surfaces can be mainly quantified as static contact angle, contact angle hysteresis, and sliding angle by various models. All of the models are introduced in detail in this section.

2.7.1 Static Contact Angle

In 1805, a physician, Young, suggested that an interface between two materials has a specific energy, the so-called interfacial energy, and it is proportional to the interfacial area. This concept has become the foundations of the wettability. It is well-known that the surface atoms/molecules of liquids/solids have higher energy than those in the interior. This results in surface free energy or surface tension to reach a stable state with a relatively low energy. Thus, the surface properties can be quantitatively evaluated by surface tension or free surface energy. The value is equal to the surface work required to keep one unit area of the surface at a constant volume and temperature. The units of γ commonly used are Jm^{-2} or Nm^{-1} . This can be interpreted either as energy per unit surface area or tension force per unit length of a contact line on the surface. During the nineteenth and twentieth centuries, thermodynamic theories postulated that superhydrophobicity is a wetting property but not particle cohesion. When a liquid (L) is in contact with a solid (S), the molecular attraction reduces the energy of the system and reaches an equilibrium value which is less than the sum of the two separated surfaces. The wetting process of the interface formation is governed by the thermodynamic principle of energy reduction. The total energy of the system is reduced by the elimination of the two surfaces to form an interface. The

thermodynamic condition of the wetting therefore can be represented as:

$$\gamma_{SA} \geq \gamma_{SL} \geq \gamma_{LA}$$

where γ_{SA} and γ_{LA} are the surface energies/tensions of the solid and liquid against air respectively, and γ_{SL} is the interface energy/tension between the solid and liquid. The work of adhesion can be expressed as:

$$W_{SL} = \gamma_{SA} + \gamma_{LA} - \gamma_{SL} \quad (2-1)$$

where W_{SL} is the work of adhesion per unit area between the solid and liquid surfaces. If a liquid droplet is placed on a solid surface, the cohesion of superficial particles at the surfaces of solid and liquid will give rise to the appropriate angle of the contact between the two surfaces as shown in Eq. 2-2 and Figure 2.14(a).

$$F_{SA} = F_{SL} + F_{LA} \cos \theta_Y \quad (2-2)$$

In other words, Young described that the interaction between the cohesion forces among the liquid and the adhesion force of the liquid to the solid determine whether the spreading of the liquid occurs over the surface, and results in an appropriate angle of contact between them. When the droplet is small enough, it is assumed that gravitational potential energy can be neglected. For a constant volume, the droplet will therefore form a contact angle with the solid surface, and the contact angle can be determined by Young's equation:

$$\cos\theta_Y = \frac{\gamma_{SA} - \gamma_{SL}}{\gamma_{LA}} \quad (2-3)$$

Regarding an ideal solid surface, the influences of roughness and chemical heterogeneity are neglected. Eq. 2-3 is deduced under the condition that the substrate is assumed to be perfectly smooth, chemically homogeneous, and rigid. However, there are no perfectly smooth ideal surfaces. As a result, it is necessary to understand how the contact angle functions on a rough surface.

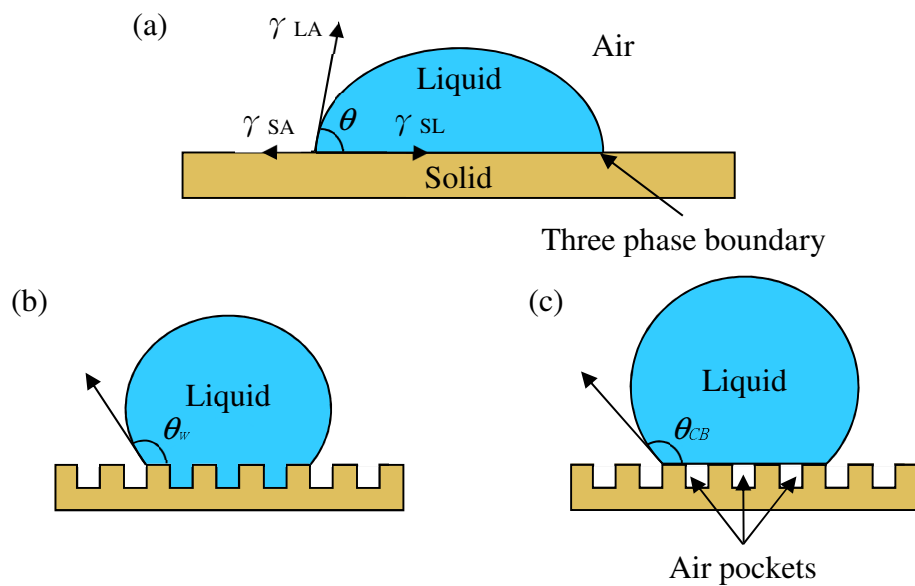


Figure 2.14 A liquid droplet (a) with force at three-phase contact line on a smooth surface, (b) under Wenzel state on a rough surface, and (c) under Cassie-Baxter state on a rough surface.

Wenzel (1936) was the first to establish a conceptual model for the theoretical study of the wetting behavior illustrating the influence of roughness on hydrophobicity when a water droplet on a rough surface spreads and engulfs the

surface topography, under a solid-liquid interface as shown in Figure 2.14(b). It is a homogenous solid-liquid interface which is undesirable for self-cleaning surfaces due to its high contact angle hysteresis and water roll-off angle (Marmur, 2004). Following Wenzel's model, Cassie and Baxter (1944) used the Wenzel model to propose a modified model to describe the phenomenon of entrapped gas under a droplet in the pits of a rough surface, resulting in a composite solid-liquid-air interface. It is a composite solid-liquid-air interface which is desirable for superhydrophobicity and self-cleaning surfaces, as shown in Figure 2.14(c) due to its low contact angle hysteresis and water roll-off angle (Marmur, 2004). At present, most researchers currently employ the Wenzel and the Cassie-Baxter models to calculate the apparent contact angle of a water droplet on a rough surface. The apparent contact angle of the liquid droplet, θ_w on a flat surface is calculated by Wenzel formula as shown below:

$$\cos \theta_w = r \cos \theta_Y, \quad (2-4)$$

where r is the ratio of the actual area of liquid-solid interface to the projected area on the horizontal plane of the rough surface (i.e. roughness factor) which is completely wetted under a homogeneous state, and θ_Y is the equilibrium contact angle of the liquid droplet on the corresponding flat surface as shown in Eq. (2-3).

Cassie and Baxter (1944) described the apparent contact angle, θ_{CB} of the

droplet on a solid-liquid-air interface by a formula which is modified from Wenzel formula as shown below:

$$\cos \theta_{CB} = f_1 \cos \theta_1 + f_2 \cos \theta_2 \quad (2-5)$$

where f_1 is the projected area of the liquid-air interfaces under the droplet on the rough surface, and f_2 is the projected area of the solid-liquid interfaces under the droplet on the rough surface. Due to the hydrophobicity of air, the contact angle of air (θ_2) is 180° . Hence, the value of $\cos \theta_2$ is -1 . In addition, $1 - f_1 = f_2$. The Cassie-Baxter model was modified according to Eq. (2-4) and Eq. (2-5). The modified Cassie-Baxter model is shown as Eq. (2-6).

$$\cos \theta_{CB} = rf \cos \theta_0 + f - 1 \quad (2-6)$$

where f is the fraction of the projected wet area of the solid-liquid-air interfaces under the droplet on the rough surface which is in a heterogeneous composite state as shown in Figure 2.14(c). If the top asperities of the rough surface is relatively flat, the roughness factor, r is assumed as 1. The Cassie-Baxter model as shown in Eq. (2-6) is then expressed as:

$$\cos \theta_{CB} = f(\cos \theta_0 + 1) - 1 \quad (2-7)$$

All the static contact angles are measured by the structures and the events at the droplet contact line. With regard to these estimation methods of the static contact angle, the roughness factor, r and the fraction of the projected wet area of

the liquid-air interfaces under the droplet, f should be calculated first with reference to the given dimensions of the specific surface geometries.

Regarding the optimization of hydrophobicity of a surface, the higher the static contact angle of the liquid droplet, θ_{CB} , the better the self-cleaning properties of the surface. According to the Cassie-Baxter formula, as shown in Eq. (2-6), the hydrophobicity of a surface can be improved by (i) increasing roughness factor, r , (ii) using a more hydrophobic material (increasing θ_0 when $90^\circ < \theta_0 < 180^\circ$), or (iii) decreasing the fraction of the projected wet area of the liquid-air interfaces under the droplet, f where $0 < f < 1$, since all of these approaches increase the value of θ_{CB} . However, if the roughness factor or the fractional flat geometric area of the liquid-air interfaces under the droplet cannot be defined accurately, this could lead to a discrepancy in calculation. In addition, these equations do not consider other factors such as pressurized air and unbalanced contact area between the liquid and solid surfaces.

2.7.2 Dynamic Contact Angle

The dynamic contact angle can be measured when the three-phase boundary of a liquid droplet is moving. In order to quantify the adhesion of a sample surface, the advancing and receding angles of the liquid droplet can be measured to

calculate the contact angle hysteresis (CAH). CAH is defined as the difference between the advancing contact angle (ACA) and the receding contact angle (RCA). Advancing and receding contact angles represent the maximum and minimum contact angles of a liquid droplet on a sample surface respectively. There are different characterization methods for contact angle hysteresis including the tilted plate method (Zhao and Law, 2012), the sessile drop method by increasing and decreasing liquid volume (Yeh and Chen, 2008), and the dragging method (Yong et al., 2014). Different characterization methods have their advantages and disadvantages.

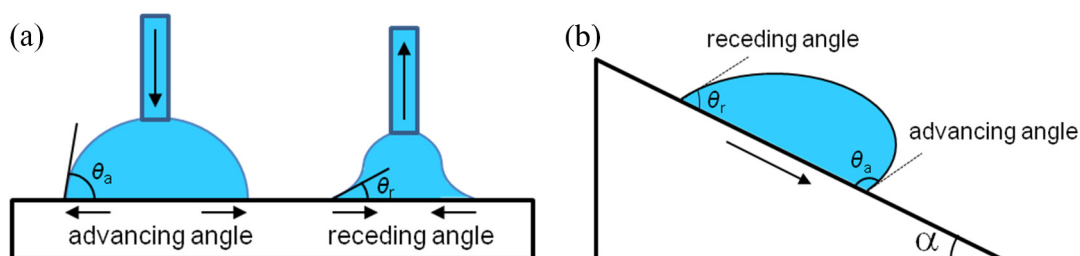


Figure 2.15 Contact angle hysteresis measurements using (a) sessile drop method, and (b) tilting plate method.

The sessile drop method is most commonly used to measure the CAH since it simply requires a water pump for increasing and decreasing liquid droplet volume as shown in Figure 2.15(a). However, this method is not appropriate for characterizing surfaces with high friction since the droplet shape and the observed contact angle may be distorted, especially when decreasing the liquid volume. This

is especially true for surfaces with large hysteresis (Eral et al., 2012). In contrast to the sessile drop method, the dragging method can avoid this problem since it is not necessary to decrease the liquid volume. This method simply requires a liquid syringe to drag the droplet on the sample. The distortion of the droplet being dragged is mostly caused by the adhesion of the droplet to the sample surface. Regarding the tilting method, the basic requirement for using this method is that the liquid droplet should be able to slide on a tilted surface at a specific angle, as shown in Figure 2.15(b).

To investigate the liquid droplet mobility on a sample surface, sliding angle measurement is one of the major approaches to quantify the mobility. The sliding behaviour of a liquid droplet on a sample surface is among the fundamental aspects of wettability (Lv et al., 2010; Miwa et al., 2000). The sliding angle is the basic characteristic of contact angle hysteresis of a sample surface. The sliding angle is defined as the angle at which both the advancing and receding contact lines of the liquid droplet start to move on the sample at a specific tilting angle. Furmidge (1962) developed a model to describe the relationship between the sliding angle, advancing contact angle, and receding contact angle, as shown in Eq. (2-8).

$$\frac{mg \sin \alpha}{w} = \gamma(\cos \theta_R - \cos \theta_A) \quad (2-8)$$

where α is the sliding angle, m is the weight of the water droplet, w is the bottom

width of the droplet, γ is free energy of the liquid at the liquid-gas interfaces, and θ_R and θ_A are the receding and the advancing contact angles respectively.

Wolfram et al. (1978) established an empirical equation to describe the sliding angle of a droplet on smooth surfaces of various materials as shown in Eq. (2-9).

$$\sin \alpha = k \frac{2r\pi}{mg} \quad (2-9)$$

where α is the sliding angle, r is the radius of the droplet contact circle, m is the droplet weight, g is the gravitational acceleration, and k is a proportionality constant.

2.8 Summary

Although extensive research has been conducted on fabrication methods for self-cleaning surfaces, the major factors for achieving self-cleaning properties, and characterization methods of droplet wetting states, some gaps in this research have been identified as follows:

- (i) Most of the conventional fabrication methods on manufacturing superhydrophobic surfaces are time-consuming, not suitable for fabricating large surfaces, or are only applicable to particular engineering materials such as metals, semiconductors, and alloys but are limited for plastics. Hence, there are very few one-step highly controllable manufacturing methods capable to fabricate bare

hydrophobic micro-patterned surfaces with good sliding performance for mass production.

- (ii) Conventional fabrication methods of superhydrophobic surfaces mainly focus on improving the self-cleaning performance but most did not consider combining it with optical properties. Therefore, it is necessary to develop an optimization model to strike a balance between the self-cleaning and optical properties for the next generation of advanced self-cleaning surfaces.
- (iii) Traditional verification methods of a droplet wetting state are only capable of identifying complete wetting, and the composite wetting state on isotopic micro-patterned surfaces, but cannot verify intermediate wetting states. This limitation further leads to an incomplete understanding of the influence of intermediate wetting states on the sliding performance of a water droplet. It is therefore necessary to propose a better characterization method to identify the droplet wetting states.

Chapter 3 Optimization Modeling of Biomimetic Structures for Self-cleaning and Optical Performance

3.1 Introduction

In this chapter, the methodology used for modeling and optimizing biomimetic structures for self-cleaning in ultra-precision machining is proposed for this research study.

Figure 3.1 shows a schematic diagram of the methodology for modeling and optimizing biomimetic structures for self-cleaning in ultra-precision machining. In the first step of this approach, a structure or design should be determined by defining the geometrical specifications qualitatively (i.e. number of geometrical parameter involved). A model considering the self-cleaning performance and optical performance of designed structure geometries are developed to estimate the static contact angle by determining the wetted contact or composite contact. The optical performance results including reflection and transparency of the designed structured geometries are also predicted. The 3D surface modeling of the designed structure geometry can be developed from the mathematical models, as shown in Section 3.3.

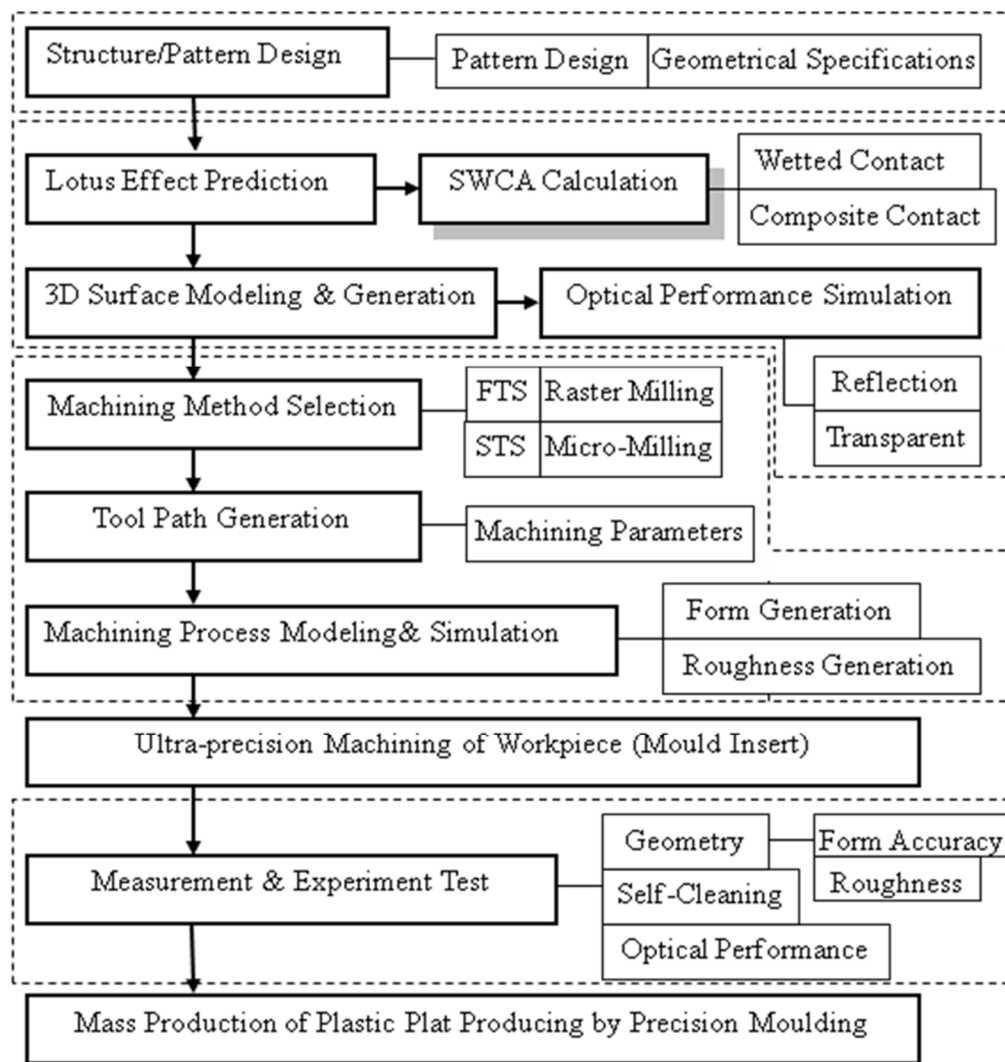


Figure 3.1 Schematic diagram of the methodology for modeling and optimizing biomimetic structures for self-cleaning in ultra-precision machining.

Based on the results obtained from the model described previously, the machining method of the corresponding surface geometry in ultra-precision machining, such as ultra-precision raster milling, micro-milling, single-point diamond turning (SPDT) with fast tool servo (FTS) or slow tool servo (STS) can then be determined. After given specific machining parameters in the tool path generation, a machining process modeling and simulation can be executed in order

to estimate the form generation and roughness generation. A fabricated sample or a mould insert of a workpiece with designed surface patterns can then be tested in order to find out the compensation factors for injection moulding. 3D surface topography measurements, such as for contact angle measurement is then followed in order to find out the actual dimensions of the surface geometry, such as form accuracy and surface roughness, self-cleaning performance (i.e. static and dynamic contact angle), and optical performance. At the final stage of this approach, a mass production of plastic plate or thin film can then be manufactured by precision die casting or hot rolling respectively.

3.2 Design Criteria of Surface Geometry

The design criteria of the surface geometry of self-cleaning surfaces are based on the three major requirements: self-cleaning performance requirements, optical performance requirements, and consideration of machining capability.

3.2.1 Self-cleaning Performance Requirements

According to the literature, Wenzel in 1936 was the first to establish a model to illustrate the influence of roughness on hydrophobicity when a water droplet on a rough surface spreads and engulfs the surface topography. The apparent contact angle of the drop, θ_w can be calculated by the Wenzel formula,

$$\cos \theta_w = r \cos \theta_Y \quad (3-1)$$

where r is the ratio of the actual area of liquid-solid interface to the projected area on the horizontal plane of the rough surface (i.e. roughness factor), and θ_Y is the equilibrium contact angle of the liquid drop on the corresponding flat surface. In other words, Wenzel's equation predicts that roughness will enhance the intrinsic wetting behaviour of a surface which is determined by its surface chemistry (i.e. surface material). If the contact angle on the smooth surface is higher than 90° , roughness will further increase the observed contact angle. On the other hand, if it is lower than 90° , roughness will further decrease the observed contact angle.

In case of the drop in contact angle, under the Cassie-Baxter state, involving wetting on composite solid-liquid-air interface surfaces, the apparent contact angle, θ_{CB} can then be calculated by the Cassie-Baxter formula,

$$\cos \theta_{CB} = rf \cos \theta_0 + f - 1 \quad (3-2)$$

where f is the fractional flat geometric area of the liquid-air interfaces under the droplet.

According to the given surface geometry parameters of the designed structured surfaces, the apparent contact angle can be estimated. However, the accuracy of the estimation will highly depend on the f value in which the calculated results can deviate from the experimental results due to the unbalanced contact

area of liquid on the measured surface.

Mathematical models based on Wenzel regimen and Cassie-Baxter regimen for the estimation of static contact angle of two typical structured surface design

(a) micro-grooves, and (b) micro-pillars (see Figure 3.2) are derived as follows:-

$$\begin{aligned}
 r &= (c - 2h \cot \alpha + s + 2h \csc \alpha) / (c + s) \\
 &= 1 + 2h(\csc \alpha - \cot \alpha) / (c + s) \\
 &= 1 + 2(\csc \alpha - \cot \alpha) / (c/h + s/h) \\
 &= 1 + A / (B + C)
 \end{aligned}
 \quad \left\{ \begin{array}{l} A = 2(\csc \alpha - \cot \alpha) \\ B = c/h \\ C = s/h \end{array} \right. \quad (3-3)$$

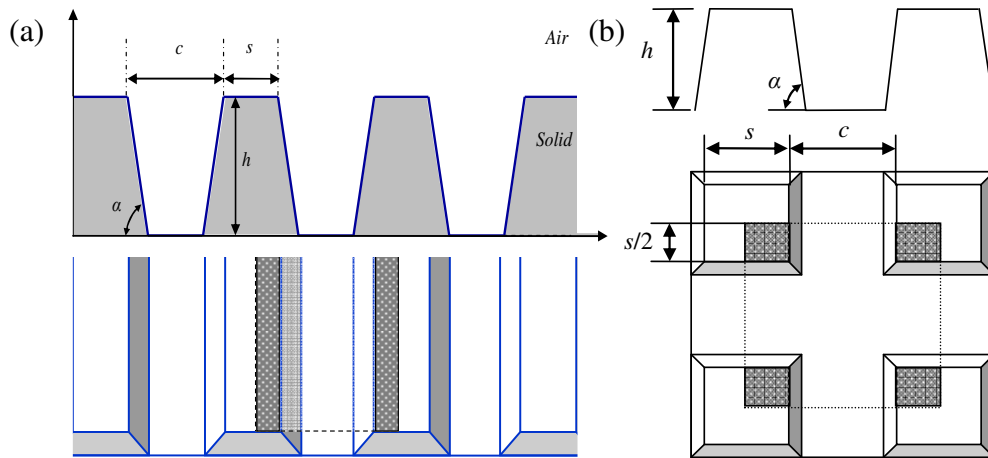


Figure 3.2 Two typical structures surface design (a) micro-grooves, and (b) micro-pillars (Kong et al., 2012).

Eq. 3-4 obtained is to describe the droplet under the Wenzel regimen on the designed structure surfaces.

$$\cos \theta_w = r \cos \theta_Y = [1 + A / (B + C)] \cos \theta_Y \quad (3-4)$$

Eq. 3-7 is expressed in terms of A, B, C and θ_Y to describe the droplet under the Cassie-Baxter regimen on the designed structure surfaces.

$$f = \frac{s}{(c+s)} = \frac{1}{(1+c/s)} = \frac{1}{(1+D)} \quad \{D = c/s \quad (3-5)$$

$$\cos \theta_{CB} = rf \cos \theta_Y + f - 1 \quad (3-6)$$

$$\cos \theta_{CB} = \frac{1}{(1+D)} \left[\left(1 + \frac{A}{B+C}\right) \cos \theta_Y + 1 \right] - 1 \quad \begin{cases} A = 2(\csc \alpha - \cot \alpha) \\ B = c/h \\ C = s/h \\ D = c/s \end{cases} \quad (3-7)$$

According to Eq. 3-7, when the apparent contact angle, θ_{CB} is high, the possibility of droplet rolling becomes higher. In other words, the value of $\cos \theta_{CB}$ should be small. Therefore, it requires a high value in θ_Y , B, C and D but a small value of A.

However, the equation does not consider other major factors such as pressurized air under the droplet and unbalanced contact area between the surface and the liquid. Pressurized air under the droplet can affect the value of apparent contact angle of droplet since it can change the reaction force acting on the droplet due to the surface geometry. Unbalanced contact area between the surface and the liquid also leads to a deviation in the equilibrium contact angle of the liquid drop, θ_Y . Partial wetting on the rough surface is another factor that also leads to a deviation of the prediction using the equations.

3.2.2 Optical Performance Requirements

As well as the basic self-cleaning properties, an advanced self-cleaning surface includes optical functions such as transparency and aberration in design. A mathematical equation of the transparency requirement for the two typical structured surface design (a) micro-grooves, and (b) micro-pillars (see Figure 3.2) is illustrated as follows (Kong et al., 2013):

$$OP = \frac{\text{Adjacent area of } \alpha \text{ within one period}}{\text{Flatten area within one period}} \rightarrow \text{minimum} \quad (3-8)$$

$$OP = \frac{2h \cot \alpha}{c - 2h \cot \alpha + s} \rightarrow \text{minimum} \quad (3-9)$$

Eq. 3-9 implies that the smaller the OP value obtained, the higher the transparency of the structured surface. The numerator of the OP value in Eq. 3-9 shows the inclination area of the surface geometry which is not desirable for transparency in the use of the optical function. Theoretically, the optimum OP value will be achieved when α approaches 90 degree. However, there must be an angle at the side wall of the grooves. Otherwise, it will be a problem for demolding the molded micro-patterns during the plastic injection molding process. Besides the parameter of α , there are still other parameters such as h affecting the OP value, even the machinability and the wetting transition of a micro-patterned surface. The values of c and s in the denominator of the OP value in Eq. 3-9 are defined as the flattened

area of the surface geometries which is desirable for the transparency of the optical performance. Therefore, the larger the value of c and s , the smaller the value of OP, so that the better the optical function of the surface geometry. Thus, one of the ways to achieve a better performance in transparency of the surface geometries is to minimize the OP value. This equation is one of the objective functions in the optimization model for investigating the equilibrium performance between self-cleaning performance and optical performance in ultra-precision machining surface geometries.

3.2.3 Consideration of Machining Ability

As well as meeting the self-cleaning and optical performance requirement, machining ability should also be considered in the design criteria of the surface geometry. The machining ability consists of the surface generation mechanism of the surface geometries (i.e. ultra-precision raster milling and single-point diamond turning with fast tool servo), cutting tool shape (i.e. acute tool, round tool or facet tool) as displayed in Figure 3.3, and cutting conditions (i.e. feed rate, step distance, and depth of cut). All of these factors directly affect the surface geometry manufactured by the ultra-precision machining. To protect the diamond cutting tool from wear, different numbers of cutting cycles were used to generate

individual grooves. The higher the pattern depth, the more the cutting cycles are required to generate individual grooves.

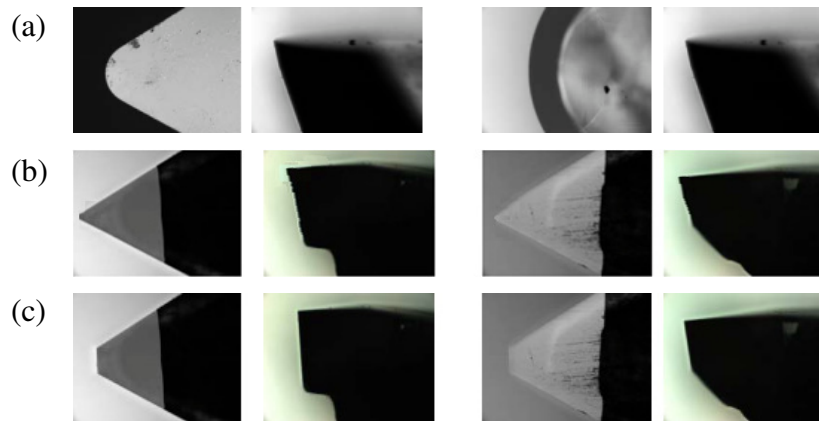


Figure 3.3 Optical images of (a) a round tool with a tool nose radius, (b) an acute tool with a rake angle, and (c) a facet tool with a tool width used in ultra-precision raster milling (Kong et al., 2013).

3.2.4 Design Challenge

As mentioned in sections 3.2.1 and 3.2.2, one of the major design challenges is to achieve both self-cleaning performance and optical performance in designing the surfaces geometries of advanced self-cleaning surfaces. However, it is found that if the surface geometry has too high density of micro-structures, the large water droplet contact area with the sample surface will increase the adhesive force of the water droplet to the material surface and also lower the optical performance of the sample surface. On the other hand, if the surface geometry has a too low density, the small water droplet contact area with the material surface will improve the optical performance of the material surface but it may not be able to achieve

self-cleaning performance due to the droplet being under the Wenzel state. The pattern depth should be high enough to prevent wetting transition of a micro-patterned surface. However, it is more difficult to manufacture micro-patterns with a higher pattern depth by plastic injection molding. The higher the pattern depth, the higher the difficulty for the material fills up individual grooves with the same groove width using plastic injection molding. As a result, there is a clear need to develop an optimization model to find the equilibrium performance between self-cleaning performance and optical performance. The optimization model includes the following steps:

- (i) To identify droplet wetting state.
- (ii) To maximize the static contact angle using Eq. 3-7 as the first constraint.
- (iii) To minimize the OP value using Eq. 3-9 as the second constraint.
- (iv) To strike a balance between the wetting and optical performance.

After the establishment of such an optimization model, the model will be validated experimentally.

3.3 Structure Design

According to the schematic diagram of the two typical designed structured surfaces (i.e. micro-grooves and micro-pillars) as shown in Figure 3.2, the

corresponding mathematical models have been constructed to act as the modeling foundation to facilitate the development of the optimization model of biomimetic structures for self-cleaning.

3.3.1 Mathematical Model of Micro-directional Grooved Surfaces

The mathematical model of micro-directional grooved surfaces, as illustrated in Figure 3.4, can be derived as Eq. (3-11). The ideal surface topographies of these micro-grooved surfaces can be simulated using MATLAB. The simulation results of the micro-grooved surfaces are shown as Figure 3.5.

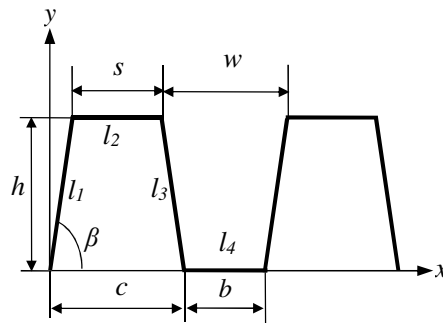


Figure 3.4 A mathematical model of micro-directional grooved surfaces.

The period of the grooves can be calculated by:

$$q = s + w \quad (3-10)$$

where s is the spacing of the grooves, and w is the width of the grooves.

Each period of the groove has four equations, and the equations for the cross sectional profiles of the grooves are thus derived as:

$$\left\{ \begin{array}{ll} l_1 : z = \tan \beta \left(x + \frac{c}{2} - mq \right) & -\frac{c}{2} + mq \leq x < -\frac{s}{2} + mq \\ l_2 : z = h & -\frac{s}{2} + mq \leq x < \frac{s}{2} + mq \\ l_3 : z = -\tan \beta \left(x - \frac{c}{2} - mq \right) & \frac{s}{2} + mq \leq x \leq \frac{c}{2} + mq \\ l_4 : z = 0 & \frac{c}{2} + mq \leq x \leq \frac{c}{2} + b + mq \end{array} \right. \quad (3-11)$$

For $m = 0, 1, \dots, n$, where n is a parameter related to the number of the grooves, $n-1$ is the number of the grooves. y in the Eq. (2) is expressed as $0 \leq y \leq 1$, where l is the length of the groove.

A set of design parameters in which α is 75° , $s = 5\mu\text{m}$, $c = 40\mu\text{m}$ and $h = 9\mu\text{m}$ is then being input into the model for validation. The 2D plot of profile and 3D plot of the frustum ridge by the mathematical model is shown in Figure 3.5.

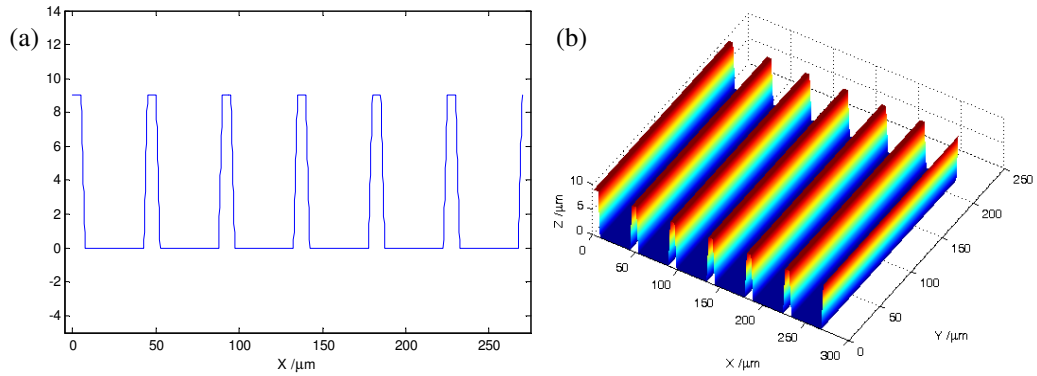


Figure 3.5 (a) 2D plot of profile, and (b) 3D Plot of frustum ridge by the mathematical model with input parameter: $\alpha = 75^\circ$, $s = 5\mu\text{m}$, $c = 40\mu\text{m}$ and $h = 9\mu\text{m}$.

3.3.2 Mathematical Model of Micro-pillar Surfaces

The mathematical model of the micro-pillar surfaces, as illustrated in Figure 3.6, can be derived as Eq. (3-12).

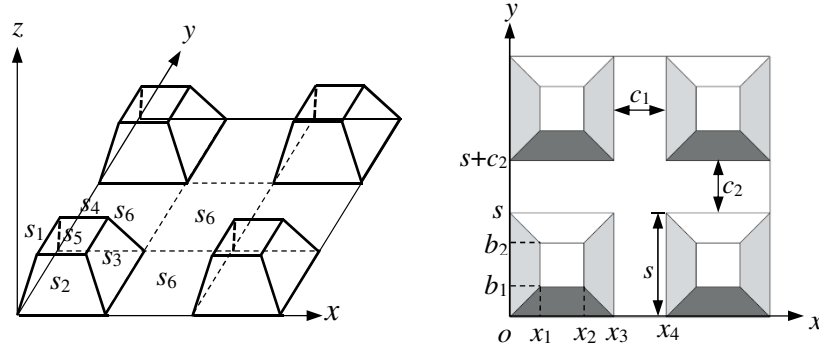


Figure 3.6 A mathematical model of micro-pillar surfaces.

The corresponding mathematical model of the micro-pillars is established as follows:

$$\begin{cases} s_1 : z = [x - nq] \tan \beta \\ s_2 : z = [x - mq] \tan \beta \\ s_3 : z = -\tan \beta [x - nq - c] \\ s_4 : z = -\tan \beta [y - mq - c] \\ s_5 : z = h \\ s_6 : z = 0 \end{cases} \quad (3-12)$$

Following the mathematical model of micro-directional grooved surfaces, a set of design parameters in which $\alpha = 75^\circ$, $s = 5\mu\text{m}$, $c = 40\mu\text{m}$ and $h = 9\mu\text{m}$ is also input into the model for validation after the complete construction of the model.

The 3D plot of a single pillar and a pillar array by the mathematical model are

demonstrated in Figure 3.7.

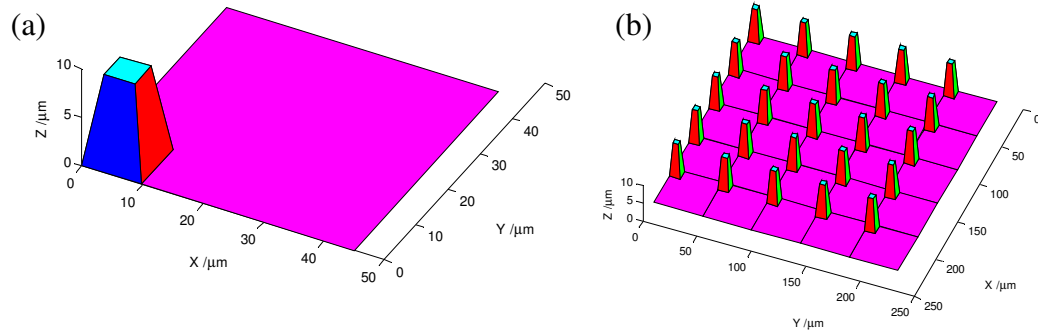


Figure 3.7 (a) 3D plot of a single pillar, and (b) 3D Plot of a frustum pillar array by the mathematical model with input parameter: $\alpha = 75^\circ$, $s = 5\mu\text{m}$, $c = 40\mu\text{m}$ and $h = 9\mu\text{m}$.

3.4 Experimental Procedures

Wang et al. (2009) investigated the micrometre surface topography of the lotus leaf, and found that the average height, width and distance between micro-pillars on the front surface of a fresh lotus leaf were $15\mu\text{m}$, $7\mu\text{m}$ and $20\mu\text{m}$ respectively. As a result, the testing range of surface geometric parameters of micro-structure patterns in this study refers to these measurement values.

3.4.1 Fabrication of Micro-patterns Using Ultra-precision Raster Milling

Polymethyl methacrylate (PMMA), which is a transparent thermoplastic, was chosen as the testing material. It is commonly applied as an alternative to glass due to its higher impact strength and lower density compared with glass. Besides, its natural hydrophilic properties help investigate whether the surface geometric

parameters catalytically ease the transition from the composite solid-liquid air interface to a homogeneous solid-liquid interface on hydrophilic materials. Nine samples of micro-grooved structures on PMMA surfaces with an approximately $9\mu\text{m}$ depth of groove, $5\mu\text{m}$ distance between grooves and different values of groove width (5, 10, 15, 20, 25, 30, 35, 40, $45\mu\text{m}$) were machined, using ultra-precision raster milling, by a Freeform 750G which is a 5-axis ultra-precision machine (see Appendix I). The wetting transition on the machined PMMA surfaces is studied by varying the width of groove. The designed micro-grooved pattern on the PMMA surface is shown in Figure 3.8. Microaperities consist of grooves with periodic depth a , width b and distance c . The machined area of each sample on PMMA is approximately $25\text{mm} \times 20\text{mm}$. The cutting conditions are summarized in Table 3.1.

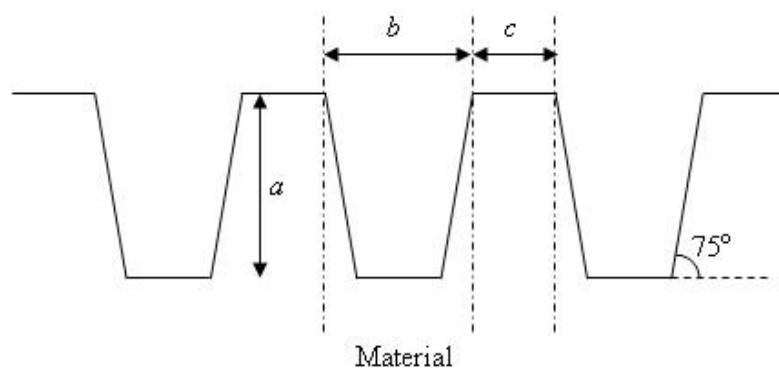


Figure 3.8 Schematic diagram of the periodic micro-grooved pattern on PMMA surface.

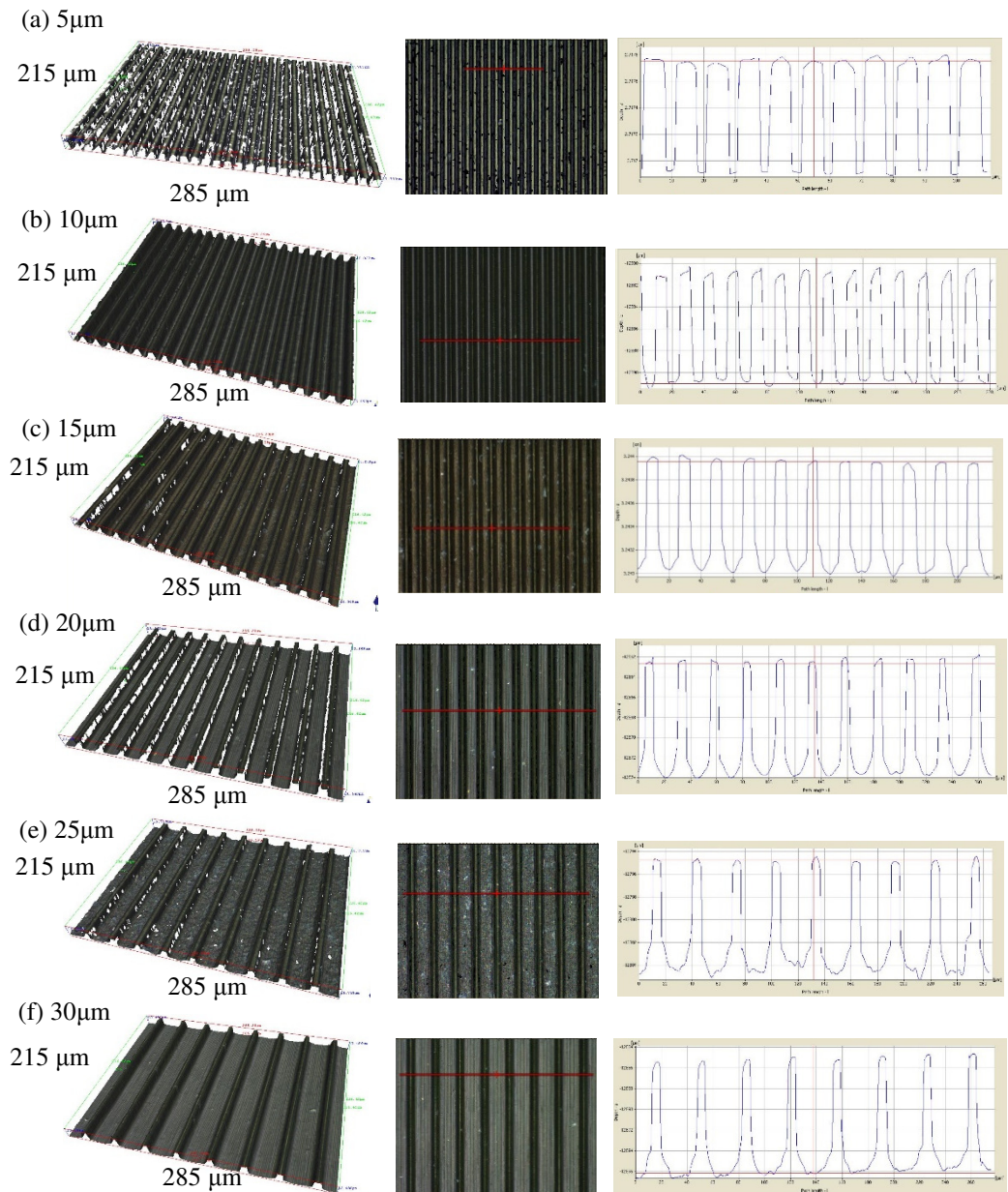
Table 3.1 Cutting conditions.

Conditions	Details
Diamond tool	Single-crystal diamond
Type	Tool A (PLF25.5)
Rake angle	25.5°
Clearance angle	12.5 °
Workpiece materials	PMMA
Spindle speed	4,000 rpm
Depth of cut	-
Swing distance	60mm
Feed rate	100mm/min
Step distance	0.1mm
Cutting strategy	Vertical cutting
Cutting environment	Lubricant off

3.4.2 Surface Topography Measurement

An optical profiler, Alicona InfiniteFocus (see Appendix IV), was used to measure the surface topography of the machined PMMA. It is an optical 3D surface measurement device which is able to measure complex components with various geometries and materials. 50x magnification, 1.80ms in exposure (brightness) and 1.20 in contrast were used for all 3D surface topography measurements of the samples. The measured surface height maps and 2-D profiles of the micro patterns on different samples are shown in Figure 3.9. The 2-D profiles of the micro patterns were measured using a cross-sectional plane cutting through the sample in the software interface. The results of the actual dimensions

are the mean values of ten measurements on different specimens, which are listed and compared with the designed dimensions in Table 3.2. Deviation between the actual and designed dimensions was found in the range of $0.06\mu\text{m} - 1.2\mu\text{m}$.



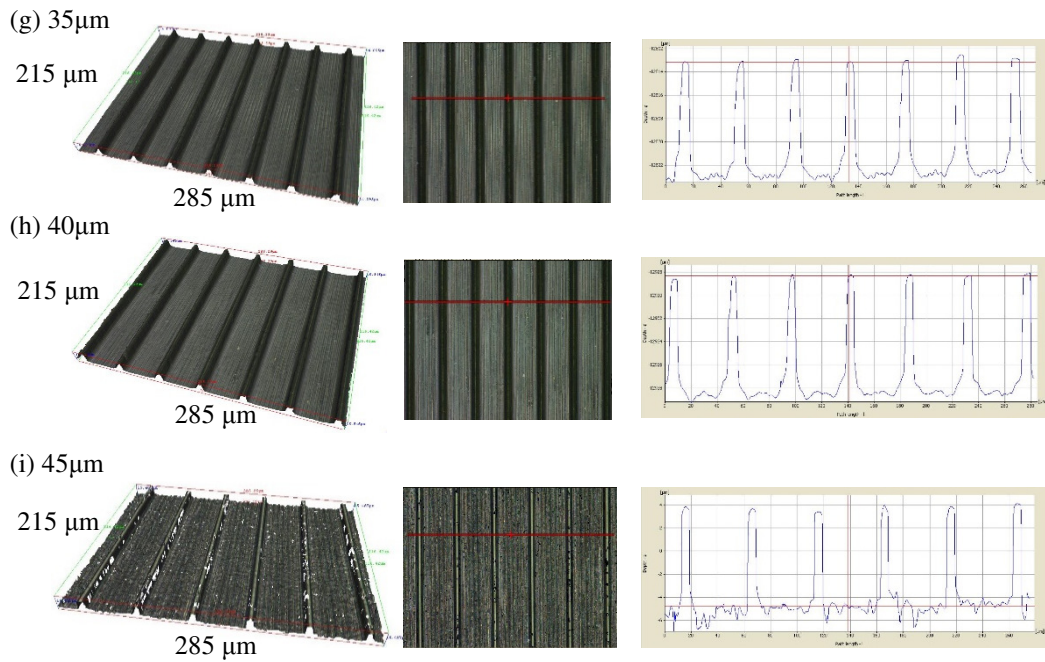


Figure 3.9 Surface height maps and 2-D profiles of the micro patterns on PMMA surfaces with various groove width of (a) 5 μm , (b) 10 μm , (c) 15 μm , (d) 20 μm , (e) 25 μm , (f) 30 μm , (g) 35 μm , (h) 40 μm , and (i) 45 μm by Alicona InfiniteFocus (50x).

Table 3.2 Measured dimensions of micro patterns with 9 μm depth, various widths and 5 μm distance between grooves by Alicona InfiniteFocus (50x).

Sample number	Designed depth of grooves (μm)	Designed width of grooves (μm)	Designed distance between grooves (μm)	Measured depth of grooves (μm)	Measured width of grooves (μm)	Measured distance between grooves (μm)
1	9	5	5	8.572	4.489	4.777
2	9	10	5	9.844	10.383	4.826
3	9	15	5	8.894	13.859	5.266
4	9	20	5	9.889	20.218	4.940
5	9	25	5	9.458	24.848	5.316
6	9	30	5	9.392	30.126	5.229
7	9	35	5	8.798	35.864	4.663
8	9	40	5	8.870	40.576	4.943
9	9	45	5	8.301	45.322	4.562

3.4.3 Contact Angle Measurement

The static contact angle measurement was carried out by a ramé-hart model 400 goniometer. The image of a sessile droplet on a surface was taken and analyzed by DROPimage Standard software using a secant fitting routine. The secant fitting method is often applied when fitting and measuring the contour of water droplets in which its static contact angle is lower than 90° , or for distorted water droplets. This contact angle measurement method aims to calculate the angle between the tangent calculated from the selected region in the arc of the water droplet in contact with the sample surface and the sample surface. This is a relatively accurate fitting method compared with the conic fitting routine. Regarding the water droplet size influencing the contact angle measurement, Nosonovsky and Bhushan (2006) found that increasing droplet size gives the same effect as increasing the period of roughness. In addition to this, a composite interface is less likely for larger droplets and larger asperities. A deionized water droplet of approximately $5\mu\text{l}$ was gently deposited onto sample using a microsyringe in the experiment (He et al., 2003). The gentle deposition of water droplet is for the purpose of minimizing the external force applied from the water droplet to the measured surface. This prevents any bouncing or pinning of the water droplet on the measured surface. The results of the static contact angle of

the water droplets were the mean values of measuring ten droplets placed in different positions on the sample surface. The observation direction in the static contact angle measurement was along the direction of the grooves on the machined surface. All contact angle measurements were conducted at $22^{\circ}\text{C} \pm 1^{\circ}\text{C}$ and $50 \pm 5\%$ relative humidity.

3.5 Results and Discussion

3.5.1 Static Contact Angle Measurement

As shown in Table 3.3, the measured static contact angle of the water droplets placed on a PMMA surface without machining was $77.7^{\circ} \pm 1.3$. After turning the sample 90° horizontally, the measured static contact angle was $76.3^{\circ} \pm 2.1$. As PMMA is a hydrophilic material with high surface energy due to its polar group, the static contact angle normally should be less than 90° . This result is consistent with the findings in the literature. The difference in static contact angle measured between these two directions is about 1.4° which is insignificantly small. This shows that a PMMA surface without machining is relatively isotropic with respect to the measurement of the static contact angle.

Table 3.3 Static contact angle (\pm SD) of PMMA surfaces without machining.

Direction	Static contact angle ($^{\circ}$)
A	77.6 ± 1.3
Perpendicular to direction	76.2 ± 2.1

The static contact angle of nine PMMA surfaces with micro patterns of various widths of groove are tabulated in Table 3.4. The data shows that the static contact angle of a hydrophilic material, PMMA, with micro patterns on nine sample surfaces is over 125° which is much higher than that of flat surface, 76.9° . It is interesting that these results of static contact angles on PMMA with micro patterns are different from the results reported by Jung and Bhushan (2006) who found that without a hydrophobic coating such as perfluorodecyltriethoxysilane, PFDTES, the PMMA nanopatterned surface manufactured by soft lithography achieved a static contact angle of less than 90° due to its intrinsic hydrophilic surface. This can be caused by the surface geometric parameters of the PMMA nanopatterned surface manufactured by soft lithography. The specific nanopatterned surface manufactured by soft lithography cannot support water droplets due to insufficient air pocket formation in the asperities. This implies that surface material is not a major factor which affects the static contact angle and

wetting transition, but surface geometry is. In addition to this, it also shows that a hydrophilic material without any hydrophobic coating can achieve a high static contact angle of water droplets through machining micro patterns on it.

Table 3.4 Static contact angle (\pm SD) of micro-patterned PMMA surfaces measured in the direction along the grooves.

Sample number	Width of groove (μm)	Static contact angle ($^{\circ}$)
1	5	133.8 ± 2.08
2	10	127.9 ± 3.01
3	15	136.6 ± 1.26
4	20	128.4 ± 1.93
5	25	136.2 ± 2.07
6	30	133.6 ± 2.82
7	35	132.8 ± 2.31
8	40	144.8 ± 2.96
9	45	120.9 ± 11.96

Most of the static contact angles of PMMA surfaces with micro patterns, from sample 1 to sample 7, achieve approximately 135° for a $5\mu\text{m}$ to $35\mu\text{m}$ width of groove, except the $10\mu\text{m}$ and $20\mu\text{m}$ widths of groove in samples 2 and 4. After being inspected in regard to the surface topographies and 2-D profiles, some of the top asperities' surfaces on sample 2 and sample 4 were found to have a slight slope, as circled in Figure 3.10. These uneven top asperities' surfaces can lead to a

reduction in the static contact angle of the micro patterns due to the unbalanced contact area with the water droplets. This explains why the static contact angle of PMMA surfaces with micro patterns decreases slightly from approximately 135° (i.e. the static contact angle of samples 1, 3, 5, 6 and 7) to 128° in sample 2 and sample 4 with a $10\mu\text{m}$ and $20\mu\text{m}$ widths of groove respectively.

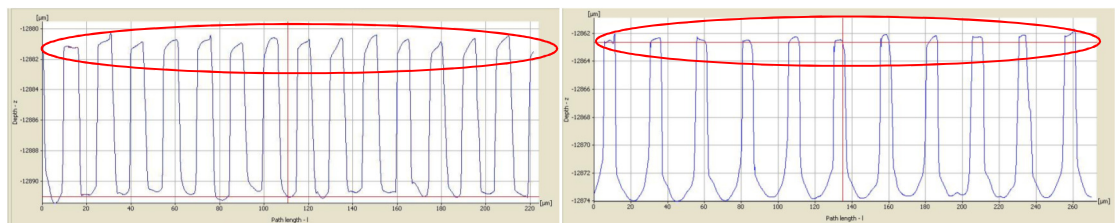


Figure 3.10 2-D profiles of the micro patterns on PMMA surfaces with (a) $9\mu\text{m}$ depth, $10\mu\text{m}$ width, $5\mu\text{m}$ distance between grooves, and (b) $9\mu\text{m}$ depth, $20\mu\text{m}$ width, $5\mu\text{m}$ distance between grooves.

The data in Table 3.4 shows that the static contact angle of PMMA surfaces with approximately $9\mu\text{m}$ depth of groove, $40\mu\text{m}$ width of groove and $5\mu\text{m}$ distance between grooves (i.e. sample 8) achieves 144.8° . Once the groove width increases from $40\mu\text{m}$ to $45\mu\text{m}$, the static contact angle decreases significantly from 144.8° to 120.9° . Furthermore, the standard deviation in the static contact angle measured on sample 9 is $\pm 11.96^\circ$. This shows that the air pocket formation nearly reaches the maximum level in the micro patterns with a $40\mu\text{m}$ groove width. Therefore, this dramatically increases the static contact angle from 135° to 144.8° which is the highest static contact angle for the nine samples in a range of between $5\mu\text{m}$ and

45 μm groove widths. The static contact angle decreases sharply from 144.8 $^\circ$ to 120.9 $^\circ$ when the groove width increases from 40 μm to 45 μm . This reveals that a water droplet will start to contact the bottom of the groove. This results in the changing of the wetting transition from the Cassie-Baxter regime to the Wenzel regime. Due to the manufacturing deviation in surface geometries of the micro patterns, some of the water droplets can still be supported by the air pocket in the asperities, as illustrated in Figure 3.11 but some have sunk and engulfed the surface topography. This induces fluctuating values of the static contact angle on the surface of sample 9, collected in the measurement. The high standard deviation of the static contact angle also implies that the wetting transition of a 5 μl water droplet is unstable when it is placed on a micro-grooved pattern, with approximately 9 μm depth of groove, 45 μm width of groove and 5 μm distance between grooves.

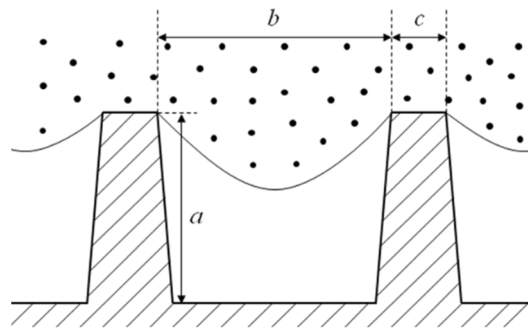


Figure 3.11 A water droplet suspended on a surface with periodic micro-grooved pattern.

The contact angles on PMMA surfaces with micro patterns are plotted as a function of groove width in Figure 3.12. According to the findings in our experiment, the dotted line drawn in Figure 3.12 indicates the boundary of wetting transition between composite solid-liquid air interface and homogeneous solid-liquid interface under a 5 μ l water droplet. This result is similar to the findings from Jung and Bhushan (2007) who reported that patterned Si with approximately 70 pitch values coated with PF₃ met the transition criteria from the Cassie-Baxter regime to the Wenzel regime.



Figure 3.12 Static contact angle as a function of geometric parameters of the micro patterns on PMMA surfaces with different groove width values with 5 μ l volume. A dotted line represents the boundary of wetting transition.

3.5.2 Length of Water Droplet Elongation

In order to verify the wetting transition on sample surfaces, the length of water droplet elongation along the grooves were also measured in this study. Table

3.5 summarizes the measured elongation length of a water droplet along the grooves. Figure 3.13 shows the elongation of a 5 μ l deionized water droplet in contact with PMMA surfaces, for different samples, captured during the contact angle measurement. All the elongation lengths were the mean values in measuring six droplets of water placed in different positions on the sample surface.

Table 3.5 Length of water droplet elongation (\pm SD) along the grooves of micro patterns on PMMA surfaces measured.

Sample number	Width of groove (μ m)	Length of elongation along the grooves (mm)
1	5	4.91 \pm 0.18
2	10	6.13 \pm 0.15
3	15	5.57 \pm 0.28
4	20	5.73 \pm 0.14
5	25	5.25 \pm 0.25
6	30	5.27 \pm 0.11
7	35	5.45 \pm 0.09
8	40	4.52 \pm 0.26
9	45	6.16 \pm 1.07

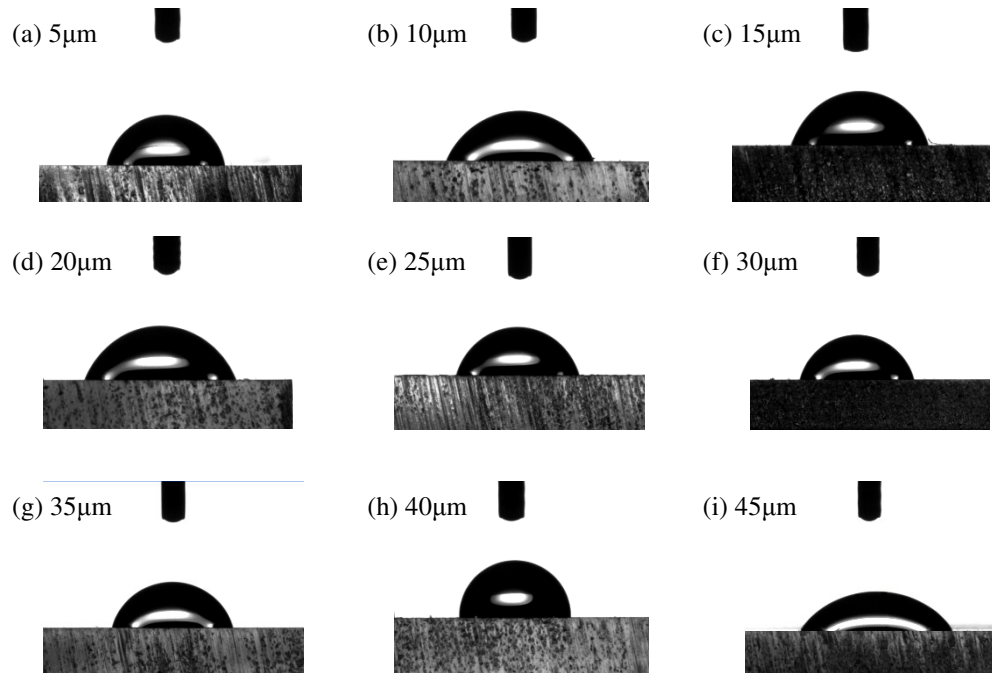


Figure 3.13 Images of a 5 μ l water droplet in contact with PMMA surface with different groove width of (a) 5 μ m, (b) 10 μ m, (c) 15 μ m, (d) 20 μ m, (e) 25 μ m, (f) 30 μ m, (g) 35 μ m, (h) 40 μ m, and (i) 45 μ m captured in the direction perpendicular to that of grooves.

The data in Table 3.5 shows that the length of elongation along the grooves in sample 2 with a 10 μ m groove width and sample 4 with a 20 μ m groove width are 6.13mm and 5.73mm respectively. These two elongation lengths are much longer compared with samples 1, 3, 5, 6 and 7 in which their elongation lengths were between 4.91mm and 5.57mm. These data are consistent with the static contact angle data shown in Table 3.4. As discussed previously, some uneven top asperities' surfaces were found in sample 2 and sample 4. These uneven top asperities' surfaces, leading to the unbalanced contact area with the water droplets,

not only cause a decrease in the static contact angle but also increase the elongation of the water droplet. As shown in Figure 3.13(h), the droplet is supported by an air pocket in the grooves and is in the Cassie-Baxter state. The sharp increase of static contact angle when the groove widths increased from $35\mu\text{m}$ to $40\mu\text{m}$ is believed to be the result of the air pocket being pressurized. The pressurized air trapped is eventually deflated when the grooves further increase to $45\mu\text{m}$. Once the width of groove is increased from $40\mu\text{m}$ to $45\mu\text{m}$, the length of elongation along the grooves increases from 4.52mm to 6.16mm . This proves that the droplet totally engulfs the surface topography, as shown in Figure 3.13(i). In other words, no entrapped air exists inside the grooves so the droplet is under the Wenzel regime. This phenomenon, however, triggers a problem of stabilization of the Cassie-Baxter regime.

As shown in the findings of this study, the highest and lowest static contact angles are found in sample 8 with a $40\mu\text{m}$ width of groove and sample 9 with a $45\mu\text{m}$ width of groove respectively. The surface geometry values between these two samples are very similar due to the difference between widths of groove being only $5\mu\text{m}$. If an external force is applied to the water droplet on the surface of sample 8, the water droplet will easily sink and contact the bottom of the groove. This will result in a changing transition from the Cassie-Baxter regime to the

Wenzel regime. Although sample 8 with a 40 μ m width of groove achieves the highest static contact angle, sample 1 to sample 7 may be more stable than sample 8 in keeping within the Cassie-Baxter regime due to leaving relatively more buffer in the air pocket formation by assuming that the droop of water with a fixed volume will decrease when the width of groove decreases under a fixed depth of groove.

3.5.3 Optical Testing of Biomimetic Structures

In order to validate the optical performance of the structured surface design of micro-grooves and micro-pillars mentioned in section 3.3, a micro-directional grooved surface and a micro-pillar surface with 10 μ m groove depth, 45 μ m groove width and spacing were machined by ultra-precision raster milling by a Precitech Freeform 705G (Precitech Inc., USA) 5-axes CNC UPRM machine. The sample material was cyclic olefin copolymer (Topas COC, 5013SL-01), copolymerized from norbornene and ethylene with a metallocene catalyst. The fundamental differences in material property of PMMA and COC have been compared as shown in Table 3.6. All the 20mm x 20mm COC sheets used in the experiment were prepared by plastic injection molding. Details of fabrication method, surface topography measurement, and wetting characteristics of the micro-patterned surfaces are further discussed in Chapter 4.

Table 3.6 Comparison between the material properties of COC and PMMA.

	Property	COC (TOPAS®5013)	PMMA
Physical properties	Density (g/cm ³)	1.02	1.15-1.19
	Water absorption (%)	<0.01	0.3-2
	Moisture absorption at equilibrium (%)	0.03	0.3-0.33
	Linear mould shrinkage (%)	0.4-0.7	0.3-0.65
	Melt flow, 115°C-260°C (g/10min)	24-48	0.9-27
Mechanical properties	Tensile strength (MPa)	46	47-79
	Elongation at break (%)	1.7	1-30
	Young modulus (MPa)	3200	2200-3800
	Impact strength (kJ/m ²)	13	1.2-20
	Notched impact strength (kJ/m ²)	1.6	11
Thermal properties	Melt temperature (°C)	240-300	130
	Thermal conductivity (W/m.K)	0.12-0.15	0.19-0.24
	Glass transition temperature (°C)	130	100-105
Optical properties	Light transmission (%)	91	80-93
	Refractive index	1.53	1.49-1.498

After the fabrication of the micro-grooves and pillars, practical tests were conducted to evaluate the optical performance. As shown in Figure 3.14, a flat COC sample is compared with the micro-grooves and micro-pillars. According to the experimental results, all the optical images displayed from the flat COC sample, the micro-directional grooved COC sample, and the micro-pillar COC sample are

clear with or without light reflection.

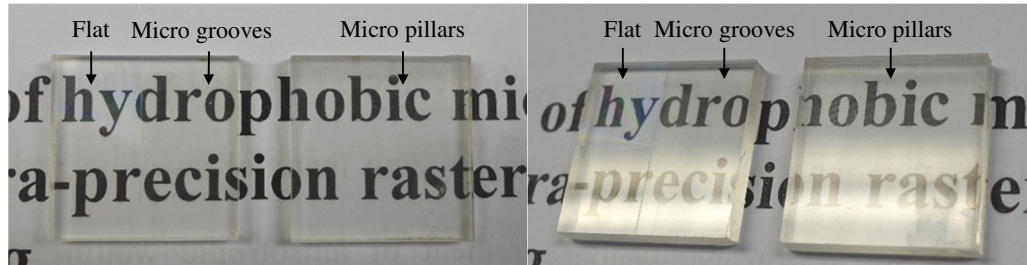


Figure 3.14 Optical images displayed from flat COC sample, micro-directional grooved COC sample, and micro-pillar COC sample (a) without light reflection, and (b) with light reflection.

In order to quantify the optical performance of the micro-patterned surfaces, the values of transmittance and haze were measured in the range of a transmittance spectrum from 420nm to 780nm wavelength using a Micro-Light MH-500 haze meter. Haze refers to the percentage of diffuse transmission to total transmission. As shown in Table 3.7, the transmittance of micro-grooves and micro-pillars are 91.35% and 89.60% respectively. These values are close to the transmission value of 91.56% measured from a flat surface. In addition, the haze of micro-grooves and micro-pillars are only 8.72% and 10.28% respectively. This shows that the haze values did not increase significantly after machining the micro-patterns when compared with a haze value of 1.73% measured from the flat sample. This implies that the roughness of the flat areas at the top and the bottom surfaces of the micro-patterns machined by UPRM can be controlled using a faceted single-crystal

diamond cutting tool. The micro-patterned surfaces are highly transparent for advanced self-cleaning surfaces.

Table 3.7 Optical performance of micro-patterned COC surfaces.

Sample	Depth of grooves (μm)	Width of grooves (μm)	Distance between grooves (μm)	Transmittance (%)	Haze (%)
Flat	-	-	-	91.56	1.73
Micro-grooves	10.0	45.5	45.1	91.35	8.72
Micro-pillars	8.3	45.1	45.5	89.60	10.28

3.6 Summary

Optimization modeling of biomimetic structures for advanced self-cleaning surfaces has been proposed to fabricate micro-patterned surfaces by considering the hydrophobicity and optical performance by ultra-precision machining. Experimental validation was conducted to evaluate both the wetting and optical performances of the micro-grooves and the micro-pillars fabricated by UPRM.

An investigation of the influence of the micro-patterns on the wetting transition in a hydrophilic material is presented. The effect of the micro patterns of a polymer, PMMA, on hydrophobicity was studied by analyzing the static contact angle and water droplet elongation along the grooves on the sample

surfaces. It was found that a micro pattern with an approximately $9\mu\text{m}$ depth of groove, $40\mu\text{m}$ width of groove and $5\mu\text{m}$ distance between grooves achieves the highest static contact angle for a $5\mu\text{l}$ water droplet in the range of $5\mu\text{m}$ to $45\mu\text{m}$ groove width. According to the findings in the experiment, surface geometry is identified as one of the major factors which govern the static contact angle. A hydrophilic material such as PMMA can become hydrophobic and achieve a high static contact angle (i.e. 144.8°) if a micro-pattern with an appropriate surface geometry is machined on its surface. As the surface material can mainly affect the contact angle hysteresis and water roll-off angle, it is construed as an essential factor in the self-cleaning properties in superhydrophobic surfaces.

The present work reveals that it is technically feasible to change the hydrophilic nature of PMMA by directly creating micro patterns on the surface using the ultra-precision raster milling technique. This one-step process provides additional flexibility in the fabrication of a wider variety of micro patterns with hydrophobicity when compared with other conventional methods. It was found that micro-patterns could lead to a higher static contact angle for a polymer, PMMA, at over 125° or even reaching 144.8° without any hydrophobic coating. The water elongation along the grooves of $45\mu\text{m}$ width is much longer than that with a $40\mu\text{m}$ width of groove (see Figure 3.13(h) and 3.13(i) due to the changing

of the wetting transition from the Cassie-Baxter regime to the Wenzel regime. Although the sample surface with a 40 μm width of groove in a micro-pattern achieves the highest static contact angle, sample surfaces with 5 μm to 35 μm widths of groove in micro-patterns may be more stable in keeping within the Cassie-Baxter regime due to leaving relatively more buffer in the air pocket formation.

Regarding the optical practical test, it was found that all the optical images displayed from the micro-grooves and micro-pillars on the COC samples was clear, with or without light reflection, by controlling the roughness of the flat areas at the top and the bottom surfaces of the micro-patterns using a faceted single-crystal diamond cutting tool. This shows that the transparency of the micro-patterns can be controlled using ultra-precision raster milling. Structural parameters for self-cleaning properties have been identified and provide an important guide for the development of advanced self-cleaning surfaces.

Chapter 4 Wetting Characteristics of Micro-patterned Surfaces Fabricated by Ultra-precision Raster Milling

4.1 Introduction

This chapter discusses the wetting characteristics of bare hydrophobic micro-patterned surfaces machined by a highly controllable one-step mechanical machining method, UPRM, which is potentially capable of manufacturing bare hydrophobic micro-patterned surfaces with good sliding performance for mass production in plastic injection molding. In the experiment, a micro-directional grooved surface and a micro-pillar surface were fabricated by UPRM. According to the mathematical models of micro-patterned surfaces, it was found from the experiment that the measured static contact angle of a water droplet agree with the static contact angle predicted by the models. This shows that the experimental data successfully validate the models. More importantly, the micro-patterned surfaces with high geometrical precision generated from UPRM define a more precise area fraction of the projected wet area for predicting the static contact angle accurately, and for investigating the feasibility of the application of the Wenzel as well as the Cassie and Baxter model. By studying the static contact angle, the interaction

between the water droplet and the sample surface, contact angle hysteresis, and sliding angle of the water droplet on micro-patterned surfaces machined by UPRM, the droplets governed by the Cassie and Baxter regimes are proven to have good sliding performance. These bare micro-patterned surfaces are shown to have great potential for mass production in microfluidic applications, such as artificial self-cleaning surfaces.

4.2 Experimentation

4.2.1 Experimental Setup

To prepare flat sample surfaces for machining micro-patterns, single-point diamond turning (SPDT) was employed to cut sample surfaces at the same level by a Nanoform 200 machine. This avoids the occurrence of various depths of micro-patterns on a large area of the workpiece surface due to the incorrect level of different workpieces. After the preparation, a Precitech Freeform 705G (Precitech Inc., USA) 5-axes CNC UPRM machine, as shown in Figure 4.1(a), was used to generate micro patterned surfaces on the workpieces which were attached by a specially designed fixture, as illustrated in Figure 4.1(b). During the machining process, a single crystal diamond faceted cutting tool with specific included angle and width of tool tip was selected and fixed on the spindle with a

certain swing distance. Figure 4.1(c) shows photos of the single crystal diamond faceted cutting tool with a 30° included angle, a 75° exterior angle (β), and a $14.0\mu\text{m}$ tool tip width, taken by a Hitachi TM3000 scanning electron microscope (SEM) (see Appendix II). The fixture, with four 90-degree corners, was manufactured on a traditional lathe and computer numerical control (CNC) milling machine. It consists of three workpiece slots that are parallel to each other. These designs provide a better alignment of different workpieces during the machining process and allow an accurate rotation of the fixture through 90 degrees using a linear variable differential transformer (LVDT) tool probe to generate the micro pillar surfaces. After the correct alignment of workpiece and the attachment of the fixture on the stationary machine table, micro patterned surfaces could be generated according to the input cutting conditions. All the cutting conditions of UPRM, including spindle speed, depth of cut, swing distance, feed rate, step distance, and cutting environment are shown in Table 4.1. The workpiece material for this study was cyclic olefin copolymer (Topas COC, 5013SL-01) which is copolymerized from norbornene and ethylene with a metallocene catalyst. All the $20\text{mm} \times 20\text{mm}$ COC sheets used in the experiment were prepared by plastic injection molding.

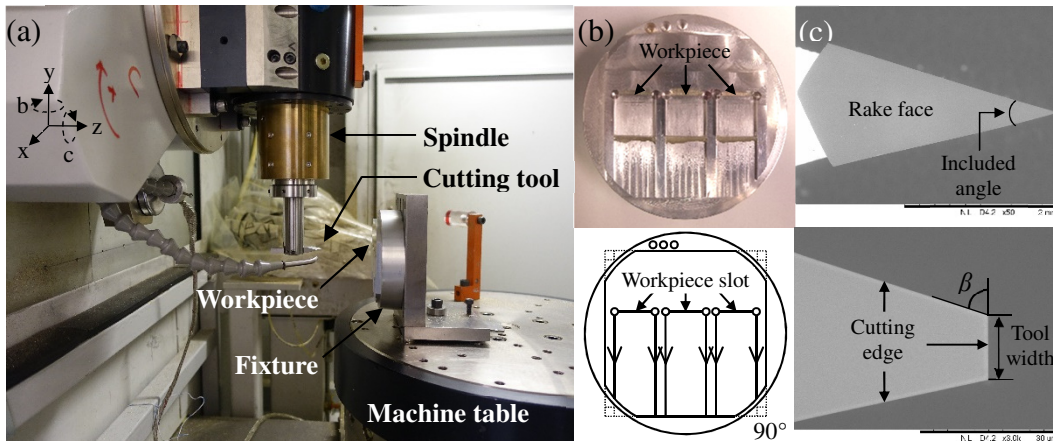


Figure 4.1 Hardware configuration of UPRM: (a) A Precitech Freeform 705G UPRM machine, (b) a workpiece fixture, and (c) SEM images of a diamond facet cutting tool tip.

Table 4.1 Cutting conditions.

Conditions	Details
Tool type	Single-crystal diamond faceted tool (14.0μm Width)
Included angle	30°
Spindle speed	4,000rpm
Depth of cut	Last depth of cut in 4μm
Swing radius	30.665mm
Feed rate	100mm/min
Step distance	0.05mm in vertical cutting strategy
Cutting strategy	Horizontal and vertical cutting
Cutting environment	Lubricant off

4.2.2 Fabrication of Micro-patterned Surfaces

In UPRM, there are two cutting strategies: horizontal cutting and vertical cutting. The main difference in the cutting geometry between these two cuttings is that the feed direction and the raster direction in horizontal cutting are opposite to

that in vertical cutting, as shown Figure 4.2.

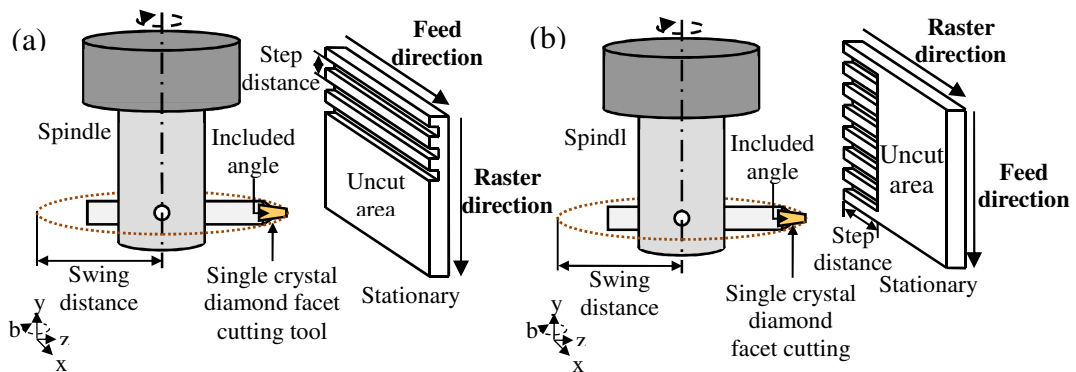


Figure 4.2 Schematic diagrams of cutting geometry by UPRM: (a) horizontal cutting, and (b) vertical cutting.

After consideration of the cutting efficiency and surface quality, a micro-directional grooved surface with $10\mu\text{m}$ depth, $45\mu\text{m}$ width, $45\mu\text{m}$ spacing, and a 75° angle were fabricated by tool path planning for surface generation. The unidirectional retreat method was employed to generate grooves on the whole single-point diamond turned sample surface by a horizontal cutting strategy, as shown in Figure 4.3(a). After the generation of the whole micro-grooved surface on the sample, vertical cutting with a step distance of 0.05mm was then employed to mill the whole sample surface by moving the cutting tool up with a specific value on the z-axis, as shown in Figure 4.3(b). The vertical cutting not only controls the depth of grooves but also can control the roughness at the top of the ridges using different cutting conditions such as feed rate and step distance (Cheng et al., 2008).

For the generation of the micro-pillar surfaces, a horizontal cutting strategy using a unidirectional retreat method was employed to first generate grooves in one direction, as illustrated in as shown in Figure 4.4(a). After the generation of the whole micro-grooved surface on the sample, the fixture was then rotated 90° along the z-axis, as shown in Figure 4.4(b). A horizontal cutting strategy using a unidirectional retreat method was employed to generate grooves perpendicular to the previous direction. The combination of the generated micro-grooves perpendicular to each direction forms a micro-pillar surface. Vertical cutting with a step distance of 0.05mm was then employed to mill the whole sample surface by moving the cutting tool up a specific amount along the z-axis, as shown in Figure 4.4(c). Due to the dimension differences between the geometries of the grooves and the cutting tool, and the protection of the diamond cutting tool from wear, different numbers of cutting cycles were used to generate individual grooves. Figure 4.5 shows a schematic diagram of each groove that was machined in four cycles by a faceted diamond tool. The depth of rough-cut in cycles 1 and 2 is over 10 μ m, whereas the depth of finish cut in cycle 3 and 4 is 4 μ m. It is known that cutting conditions and machine tool characteristics are major factors affecting the surface generation in UPRM. Therefore, surface quality evaluation is necessary and is discussed in the next session.

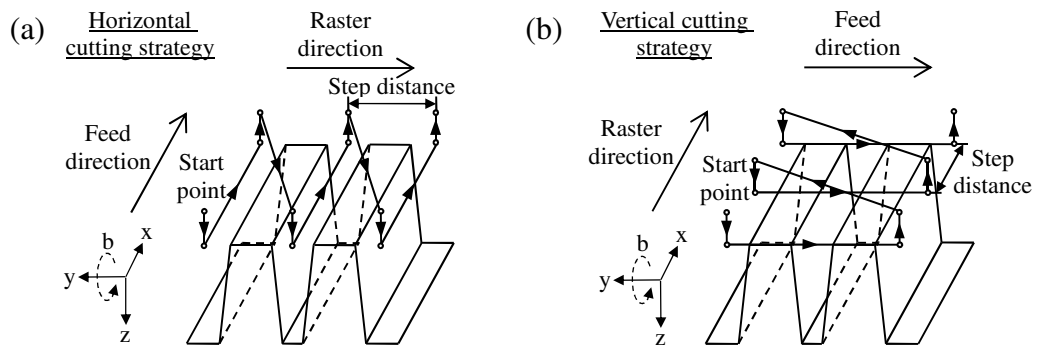


Figure 4.3 Tool path design of a micro directional grooved surface generation in sequence: (a) horizontal cutting on grooves, and (b) vertical cutting on ridges.

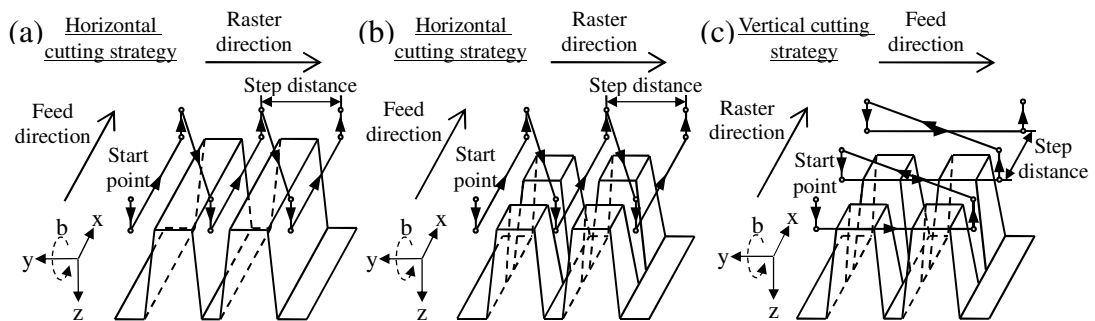


Figure 4.4 Tool path design of a micro pillar surface generation in sequence: (a) horizontal cutting on grooves, (b) horizontal cutting on grooves after a 90° turn of fixture, and (c) vertical cutting on ridges.

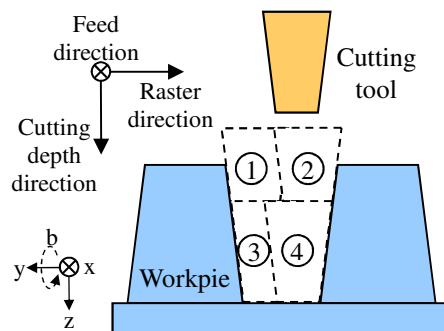


Figure 4.5 Cutting cycles of grooves on a workpiece in horizontal cutting strategy.

4.2.3 Micro-patterned Surface Topography

To measure the geometrical parameters of the micro-directional grooved and pillar surfaces machined in the experiment, a white light interferometer (Zygo

Nexview shown in Appendix III) was employed to capture the surface topographies. The system applied a non-contact method to measure surface roughness, step height and angle of slope, with vertical resolution in the nanometric range. Figure 4.6 and Figure 4.7(a) show the surface height maps, two dimensional (2D) profiles, and cross sectional view of a periodic grooved surface machined by horizontal cutting on grooves, without and with vertical cutting on ridges in 20x magnification respectively. In this comparison, cross section A-A in Figure 4.6 indicates that the edges of the ridges consist of material swelling after generating grooves by horizontal cutting on a single-point diamond turned flat surface. The material swelling directly affects the surface geometries of the micro directional grooves and the flatness at the top of the ridges. To solve the problem of material swelling, vertical cutting on the ridges was applied after generating grooves by horizontal cutting. As shown in cross section B-B in Figure 4.7(a), the vertical cutting successfully removed the material swelling and flattened the top asperities of the ridges, also providing numerical control of the height of the grooves. More importantly, this machining process generates surface geometries with higher precision. This helps to define a more accurate area fraction of the projected wet area to predict the static contact angle by the Cassie and Baxter models.

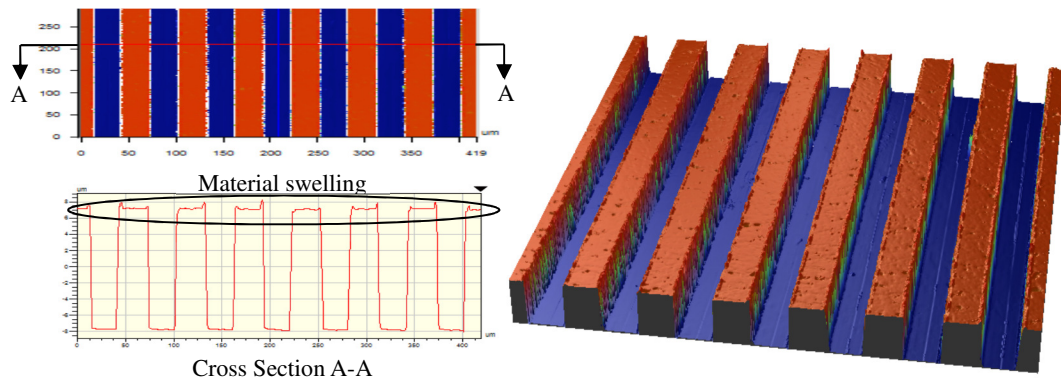


Figure 4.6 Surface topography of a micro directional grooved surface with material swelling.

Figure 4.7 shows the surface topography of micro-directional groove and pillar surfaces in 20x magnification respectively, from the experiment. It is found that the deviation between the designed and the measured dimensions of the micro-grooved and pillar surfaces are within $\pm 2\mu\text{m}$, as listed in Table 4.2. The measured angles of the slopes are around 75° , which is nearly equal to the angle formed by the tool geometry shown in Figure 4.1(c). The deviation between the designed and measured height of the pillars may be due to the material recovery of the cyclic olefin copolymer. At the bottom of the grooves, as shown in Figure 4.7(b), there is a step which shows a difference in the value of the pillar height, around $0.6\mu\text{m}$, in cross sections C-C and D-D. The measured experimental results show that the rotation of the designed fixture did not significantly affect the relative depth of cut by the tool on the sample surface, based on the datum of the fixture as shown in Figure 4.1(b), when applying horizontal cutting for generating the micro-pillars.

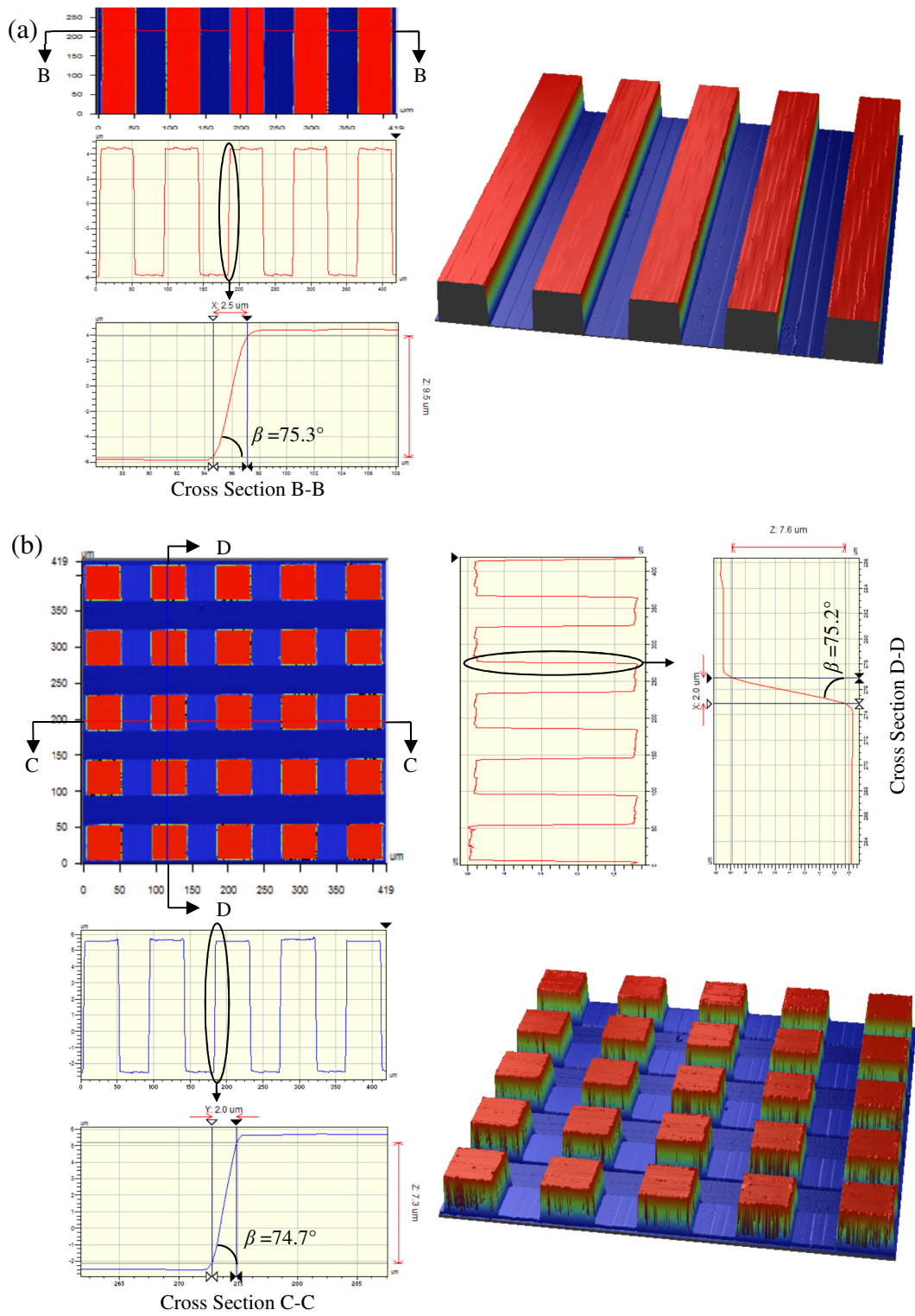


Figure 4.7 Surface topographies of (a) the micro-directional grooved surface, and (b) the micro-pillar surface from the experiment.

Table 4.2 Measured geometrical parameters of micro-patterned COC surfaces.

Surface pattern	Cross section	Design depth (μm)	Design width (μm)	Design spacing (μm)	Measured depth (μm)	Measured width (μm)	Measured spacing (μm)	Measured angle (°)
Groove	B-B	10	45	45	10.0	45.5	45.1	75.3
	C-C	10	45	45	8.6	44.7	45.9	74.7
Pillar	D-D	10	45	45	8.0	45.5	45.1	75.2

4.3 Results and Discussion

4.3.1 Comparison with the Theoretical Models

4.3.1.1 The Wenzel Model

Wenzel (1936) developed a model to describe a droplet that completely wetted a rough surface, forming a homogeneous solid-liquid interface, as shown in Figure 4.8. The static contact angle of the droplet under the Wenzel regime, θ_w can be calculated as follows:

$$\cos\theta_w = r \cos\theta_y \quad (4-1)$$

where r is the roughness ratio on the rough surface, and θ_y is the static contact angle of a droplet on a flat surface. As shown in Figure 4.8, the shaded regions and the dotted line regions represent the wetted area A_w and the projected area of the wetted regions A_{proj} on the micro-patterned surface respectively.

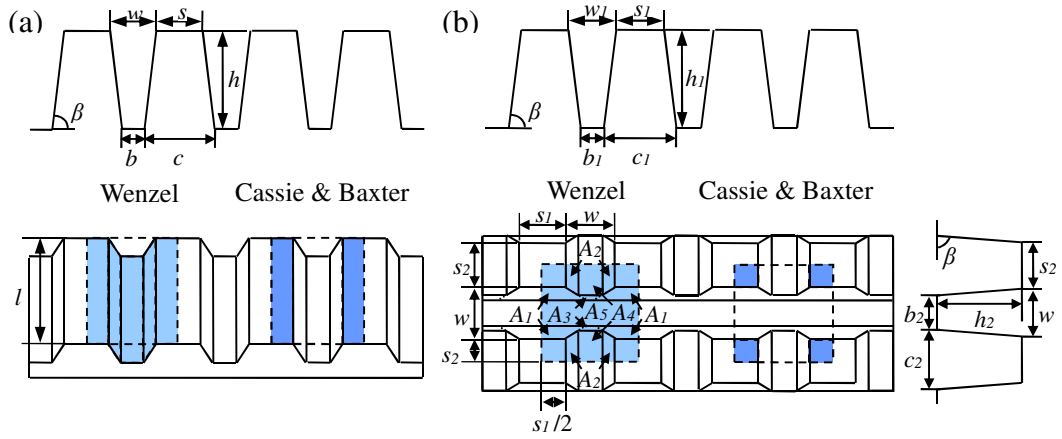


Figure 4.8 Schematic illustrations of the wetted area A_w and the projected area of the wetted regions A_{proj} on (a) micro-grooved surfaces, and (b) micro-pillar surfaces.

The roughness ratio, r of the micro-patterned surfaces is derived as follows:

$$r = \frac{A_w}{A_{proj}} \quad (4-2)$$

The wetted area on the micro-grooved surface is:

$$A_w = \left(b + \frac{2h}{\sin \beta} + s \right) \cdot l \quad (4-3)$$

where the width of the bottom of grooves, $b = w - \frac{2h}{\tan \beta}$, w is the width of grooves, h is the depth of grooves, s is the spacing between grooves, β is the exterior angle induced by the facet cutting tool, and l is the length of grooves on the micro-grooved surfaces, as illustrated in Figure 4.8(a).

$$A_w = \left(w - \frac{2h}{\tan \beta} + \frac{2h}{\sin \beta} + s \right) \cdot l \quad (4-4)$$

$$A_w = [s + w + 2h(\csc \beta - \cot \beta)] \cdot l \quad (4-5)$$

The projected area of the wetted region on the micro-grooved surface is determined as:

$$A_{proj} = (s + w) \cdot l \quad (4-6)$$

The roughness ratio, r of the micro-grooved surface is:

$$r = \frac{s + w + 2h(\csc \beta - \cot \beta)}{s + w} \quad (4-7)$$

Dividing the numerator and the denominator of r in Eq. 4-7 by h , r is expressed as:

$$r = 1 + \frac{2(\csc \beta - \cot \beta)}{\frac{s}{h} + \frac{w}{h}} \quad (4-8)$$

Hence, the Wenzel model of the micro-grooved surface is given by:

$$\cos \theta_w = \left(1 + \frac{2(\csc \beta - \cot \beta)}{\frac{s}{h} + \frac{w}{h}}\right) \cos \theta_y \quad (4-9)$$

$$\cos \theta_w = \left(1 + \frac{A}{B + C}\right) \cos \theta_y \quad (4-10)$$

where $\begin{cases} A = 2(\csc \beta - \cot \beta) \\ B = s/h \\ C = w/h \end{cases}$

The wetted area on the micro-pillar surface is:

$$A_w = \sum_{i=1}^5 A_i + s_1 s_2 \quad (4-11)$$

The projected area of the wetted region on the micro-pillar surface is determined as:

$$A_{proj} = (s_1 + w_1)(s_2 + w_2) \quad (4-12)$$

where A_i is the total wetted area of A_1, A_2, A_3, A_4 and A_5 , s_1 and w_1 are the spacing and width of pillars in one direction respectively, and s_2 and w_2 are the spacing and width of pillars in the direction perpendicular to the previous direction respectively, as illustrated in Figure 4.8(b).

The roughness ratio, r of the micro-pillar surfaces can be derived as follows:

$$r = \frac{\sum_{i=1}^5 A_i + s_1 s_2}{(s_1 + w_1)(s_2 + w_2)} \quad (4-13)$$

In the case where $h_1 < h_2$ (similar when $h_1 > h_2$), five areas on the micro-pillar surfaces are calculated, as shown in Figure 4.8(b). The same faceted diamond cutting tool with a 30° included angle is applied to generate two different directional grooves perpendicular to each other. Both the geometries of the micro-pillars in two different directions, therefore have the same angle β which is 75° , as shown in Figure 4.1(c). The five areas on the micro-pillar surfaces are derived as:

$$\left\{ \begin{array}{l} A_1 = 2(s_1 + s_1 + 2h_2 \cot \beta)h_2 \csc \beta / 2 \\ \quad = 2(s_1 + h_2 \cot \beta)h_2 \csc \beta \\ A_2 = 2(s_2 + s_2 + 2h_1 \cot \beta)h_1 \csc \beta / 2 \\ \quad = 2(s_2 + h_1 \cot \beta)h_1 \csc \beta \\ A_3 = 2(w_1 - 2h_1 \cot \beta + w_1 - 2h_2 \cot \beta)(h_2 - h_1) \csc \beta / 2 \quad (h_1 < h_2) \\ \quad = 2[w_1 - (h_1 + h_2) \cot \beta](h_2 - h_1) \csc \beta \\ A_4 = 2(w_1 - 2h_1 \cot \beta)[s_2 / 2 + w_2 / 2 - (h_2 - h_1) \cot \beta] \\ \quad = (w_1 - 2h_1 \cot \beta)[s_2 + w_2 - 2(h_2 - h_1) \cot \beta] \\ A_5 = (s_1 + w_1)(w_2 - 2h_2 \cot \beta) \end{array} \right. \quad (4-14)$$

Hence, the Wenzel model of the micro-pillar surface is given by:

$$\cos \theta_w = \frac{\sum_{i=1}^5 A_i + s_1 s_2}{(s_1 + w_1)(s_2 + w_2)} \cos \theta_Y \quad (4-15)$$

In the case where $s_1 = s_2 = w_1 = w_2$, the Wenzel model of a micro-pillar surface is expressed as:

$$\cos \theta_w = \frac{\sum_{i=1}^5 A_i + s_1^2}{4s_1^2} \cos \theta_Y \quad (4-16)$$

4.3.1.2 The Cassie and Baxter Model

Cassie and Baxter (1944) established a model based on modification of the Wenzel model to describe a droplet on a heterogeneous surface, with solid-liquid-air interfaces, as shown in Figure 4.8. The static contact angle of the droplet under the Cassie and Baxter regime θ_{CB} can be calculated as follows:

$$\cos \theta_{CB} = R_f f \cos \theta_F + f - 1 \quad (4-17)$$

where f is the area fraction of the projected wet area, and R_f is the roughness ratio on the wet area. As shown in Figure 4.8, the shaded regions and the dotted line regions represent the wetted area A_w and the projected area of the wetted regions A_{proj} on the micro-patterned surface respectively. The roughness ratio R_f on the wetting area of the top asperities on both the micro-grooved and pillar surfaces are assumed to be 1 in Eq. 4-17, since faceted diamond cutting is applied to generate an optical flat surface by vertical cutting.

The area fraction of the projected wet area, f of the micro-grooved surface is derived as:

$$f = \frac{s}{s + w} \quad (4-18)$$

Hence, the Cassie and Baxter model of the micro-grooved surface is given by:

$$\cos \theta_{CB} = \frac{s}{s + w} (\cos \theta_Y + 1) - 1 \quad (4-19)$$

Dividing the nominator and denominator of $\frac{s}{s + w}$ in Eq. 4-19 by s , $\cos \theta_{CB}$ is expressed as:

$$\cos \theta_{CB} = \frac{1}{1 + \frac{w}{s}} (\cos \theta_Y + 1) - 1 \quad (4-20)$$

$$\cos \theta_{CB} = \frac{1}{1 + D} (\cos \theta_Y + 1) - 1 \quad (4-21)$$

where $D = \frac{w}{s} = \frac{C}{B}$.

In the case where $s = w$, the Cassie and Baxter model of the micro-grooved surface is expressed as:

$$\cos \theta_{CB} = \frac{1}{2} (\cos \theta_Y + 1) - 1 \quad (4-22)$$

The area fraction of the projected wet area, f of the micro-pillar surface is derived as:

$$f = \frac{s_1 s_2}{(s_1 + w_1)(s_2 + w_2)} \quad (4-23)$$

Hence, the Cassie and Baxter model of the micro-pillar surface is given by:

$$\cos \theta_{CB} = \frac{s_1 s_2}{(s_1 + w_1)(s_2 + w_2)} (\cos \theta_Y + 1) - 1 \quad (4-24)$$

In the case where $s_1 = s_2 = w_1 = w_2$, the Cassie and Baxter model of the micro-pillar surface is expressed as:

$$\cos \theta_{CB} = \frac{1}{4} (\cos \theta_Y + 1) - 1 \quad (4-25)$$

By using Eqs. 4-10 and 4-21, the static contact angles from the Wenzel model as well as the Cassie and Baxter model on the micro-grooved surface can be predicted. Similarly, the static contact angles from the Wenzel model as well as the Cassie and Baxter model on the micro-pillar surface are predicted by using Eqs. 4-15 and 4-24.

4.3.2 Static Contact Angle from the Experiment

In order to validate the mathematical models of the micro-directional groove and pillar surfaces built in the previous section, the static contact angles of water droplets were measured by a Sindatek model 100SB video-based optical contact angle meter (see Appendix VI) using the sessile drop method. The images of water droplets on various sample surfaces captured by camera from the side view are presented in Figure 4.9. Each reported data of the static contact angle is the average of six to eight independent measurements by a deionized water droplet of approximately 5 μ l. Table 4.3 summarizes the experimental results and the

calculations from the Wenzel model as well as the Cassie and Baxter model, using wetting analysis of the micro-patterned surfaces.

Table 4.3 Wetting performance of the micro-patterned COC surfaces.

Material	Surface pattern	Observation direction	Calculated θ_W	Calculated θ_{CB}	Average static contact angle, θ	Sliding angle, α
COC	Groove	Parallel	88.0°	119.0°	$\theta_{\parallel} = 108.9^{\circ} \pm 1.6$	24°
		Orthogonal	88.0°	119.0°	$\theta_{\perp} = 145.9^{\circ} \pm 1.8$	Not slide
COC	Pillar	Parallel	87.7°	138.0°	$\theta_{\parallel} = 137.8^{\circ} \pm 1.6$	Not slide
		Orthogonal	87.7°	138.0°	$\theta_{\perp} = 138.1^{\circ} \pm 2.0$	Not slide
COC	Flat	-	-	-	$\theta = 88.3^{\circ} \pm 1.9$	Not slide

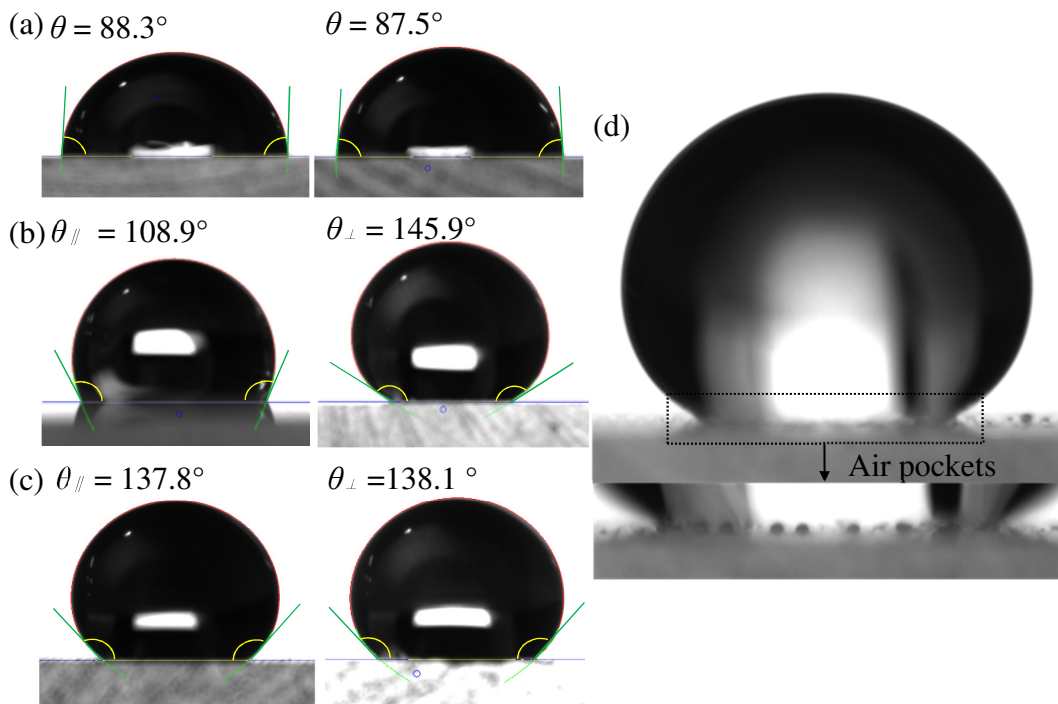


Figure 4.9 Static contact angles of water droplets on (a) the flat surface, (b) the micro-grooved surface, (c) the micro-pillar surface, and (d) air pockets under the droplet on micro-patterned surface.

The average static contact angle of the water droplets on a single point

diamond turned flat COC surface is 88.3° due to its intrinsic hydrophobic property, as shown in Figure 4.9(a). After the generation of micro-directional grooves on the flat COC surface by UPRM, the static contact angle of water droplet increases from 88.3° to 108.9° in the parallel direction, as shown in Figure 4.9(b). This reveals that the droplet freely advances on the ridges in the parallel direction, but is restricted by the periodic ridges that induce an energy barrier in the orthogonal direction (Zhao and Law, 2012; Neuhaus et al., 2012). The average static contact angle of a water droplet therefore greatly increases from 88.3° to 145.9° in the orthogonal direction. With respect to the micro-pillar COC surface, the static contact angle of the water droplet increases from 88.3° to 137.8° and 138.1° in the two directions perpendicular to each other, as shown in Figure 4.9(c). This indicates that the measured static contact angle of the water droplet greatly agrees with the static contact angle of 138.0° predicted by the Cassie and Baxter model. More importantly, this shows that UPRM is capable of manufacturing micro-patterned surfaces with high geometrical precision which defines a more accurate area fraction of the projected wet area for predicting the static contact angle by the Cassie and Baxter model, compared with other conventional fabrication methods such as lithography (Murakami, 2014), laser etching (Li et al., 2012), and chemical reaction (Tanaka et al., 2013). It is difficult to use these conventional methods to

manufacture micro-patterned surfaces with highly controllable geometrical precision and this definitely leads to the area fraction of the projected wet area in the Cassie and Baxter model not being clearly defined. Figure 4.9(d) shows that air pockets exist under the droplet on micro-patterned surfaces, and proves that the droplet is in a composite wetting state.

4.3.3 Droplet Anisotropy

To observe the anisotropy of the water droplet on various COC surfaces including a flat surface, a grooved surface and a pillar surface, the water droplet contour was captured by an optical microscope (see Appendix V) from the top view, as shown in Figure 4.10(a), Figure 4.10(b), and Figure 4.10(c). The droplet shape on the flat COC surface is circular and is nearly the same as its initial shape after deposition by a syringe. On the grooved surface, the droplet shape is elliptical which reveals that the droplet becomes slightly anisotropic due to the directional grooved surface geometries on the sample. Compared with the grooved surface, the droplet shape on the pillar surface is more rectangular. This reveals that the droplet becomes more isotropic due to the square pillars with equal spacing of the surface geometry on the sample.

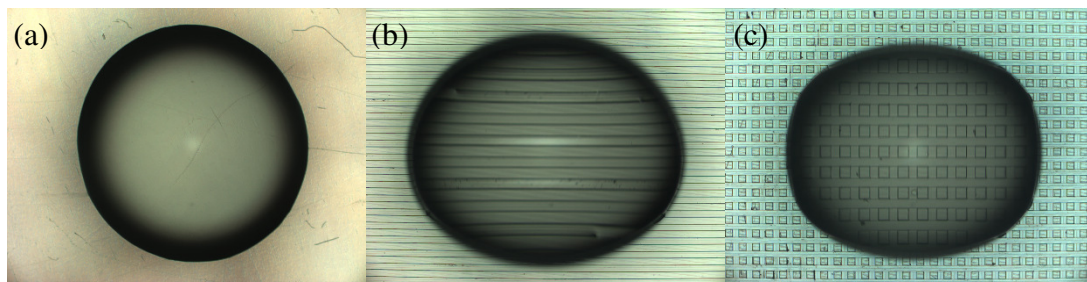


Figure 4.10 Anisotropy of a water droplet on (a) the flat surface, (b) the micro-grooved surface, and (c) the micro-pillar surface from the top view.

4.3.4 Droplet Contact Line

In order to quantify the droplet anisotropy, the lengths of the contact lines of the droplets on different samples in the parallel and orthogonal directions, from the side view in Figure 4.9, were measured using the software ImageJ. The length of the contact line is 3.249mm on the flat surface. On the micro-directional grooved surface, the lengths of the contact lines in the parallel and orthogonal directions are 2.083mm and 1.274mm respectively. On the micro-pillar surface, the lengths of the contact lines in the two directions are both equal to 1.471mm. These experimental results indicate that the micro-patterns have greatly reduced the lengths of the contact lines in the parallel and orthogonal directions compared to the flat surface.

In addition, the droplet on the micro-directional grooved surface elongated more in the parallel direction than that in the orthogonal direction. This can be explained by the droplet under the Cassie and Baxter state on the micro-directional

grooved surface freely advancing at the top of the ridges in the parallel direction after its deposition, but being restricted by the spacing between the pillars in the orthogonal direction. On the micro-pillar surface, the droplet under the Cassie and Baxter state was restricted by the equal spacing between the pillars in the parallel and orthogonal directions. The air in between the pillars induced equal amounts of energy barriers to the droplet, and this resulted in the same length of the contact line. As a result, the droplet on the micro-pillar surface is more isotropic than that on the micro-directional grooved surface.

According to the image of the water droplet contact line from the top view, as shown in Figure 4.11, the water droplet sits at the top of the ridges and the pillars on the micro-directional grooved and micro-pillar surfaces respectively. This may be due to the shaped edges induced by the machining process of vertical cutting on the ridges and pillars, which help stabilize the deposition of the water droplet. In other words, the shaped edges make the droplet sit at the top of the micro-pillars due to the pinning effect. This provides evidence that the droplet is governed by the Cassie and Baxter regime, and forms a solid-liquid-air interface with the micro-patterned surface. More importantly, this is one of the essential requirements in achieving hydrophobic self-cleaning surfaces.

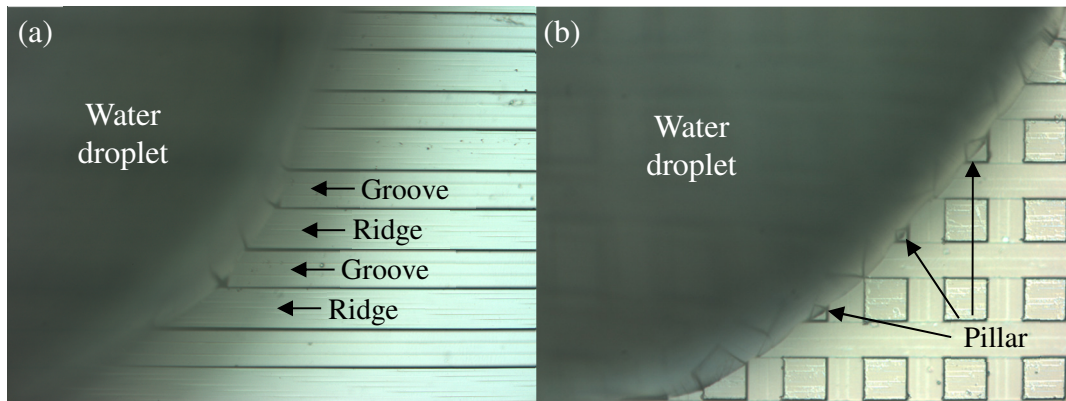


Figure 4.11 Water droplets acting on (a) the micro-grooved surface, and (b) the micro-pillar surface.

4.3.5 Contact Angle Hysteresis

In order to quantify the directional adhesion of the droplet anisotropy on three different samples, the advancing and receding angles of the water droplets were measured to calculate contact angle hysteresis (CAH) (Yong et al., 2014). There are different characterization methods for contact angle hysteresis, including the tilted plate method (Zhao and Law, 2012), the sessile drop method by increasing and decreasing liquid volume (Yeh and Chen, 2008), and the dragging method (Yong et al., 2014). Different characterization methods have their advantages and disadvantages. The reason for not using the sessile drop method is that this method may distort the droplet shape and the observed contact angle, especially when decreasing the liquid volume. This is especially true for surfaces with large hysteresis (Eral et al., 2012). Thus, it is not appropriate to characterize the contact angle hysteresis on these surfaces using the sessile drop method. In contrast to the

sessile drop method, the dragging method can avoid this problem since it is not necessary to decrease the liquid volume. The distortion of the droplet being dragged is mostly caused by the directional adhesion of the droplet to the micro-patterned surfaces. Hence, the dragging method is selected to measure the contact angle hysteresis of the fabricated sample surfaces. The droplets were dragged by a syringe on the flat surface, the micro-grooved surface, and the micro-pillar surface, as shown in Figure 4.12. In the case of a droplet not moving at the advancing and/or receding contact line(s), the angle(s) measured at the front and/or at the back is/are named as “distorted angle”.

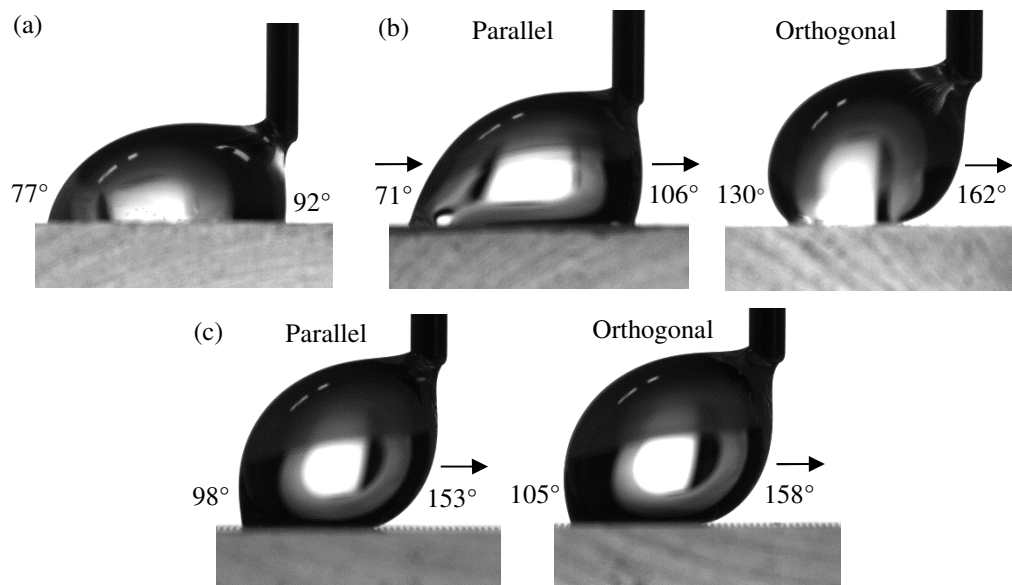


Figure 4.12 Snapshots of the advancing and the receding angle measurement on (a) the flat surface, (b) the micro-grooved surface, and (c) the micro-pillar surface.

According to the experimental results, only the droplet on the micro-grooved

surface in the parallel direction moved at the advancing and receding contact lines when being dragged, as shown in Figure 4.12(b). All the other droplets were either distorted in the original position, or just advanced but did not recede on the sample surface. This reveals that the droplet mobility of the micro-grooved surface in the parallel direction is higher than that on both the flat surface and the micro-pillar surface. This can be explained by the droplet under the Cassie and Baxter regime on the micro-grooved surface in the parallel direction being able to freely advance and recede at the top asperities of the continuous ridges when the droplet is being dragged (Zhao and Law, 2012; Yong et al., 2014). These free movements of the advancing and receding contact lines on the continuous ridges result in the relatively low advancing and receding angles (106° and 71°) in the measurement, as shown in Figure 4.12(b), when compared to the orthogonal direction and on the micro-pillar surface. The CAH of the micro-grooved surface in the parallel direction is 35° . However, the droplet on the micro-grooved surface in the orthogonal direction was highly restricted by the spacing between the continuous ridges. Some researchers indicated that surface friction is the main obstacle to droplet mobility on rough surfaces (Zhao and Law, 2012). It is believed that surface friction also plays a key role in this study. Thus, the friction induced by the continuous ridges acting on the droplet results in the highest advancing angle (162°)

and distorted angle at the back (130°), as shown in Figure 4.12(b).

In respect to the micro-pillar surface, the droplet under the composite wetting state only advanced but did not recede on the sample surface in both the parallel and orthogonal directions. The reason is that the movements of the droplet contact line in the two different directions are restricted by the equal spacing between the pillars (Gao and McCarthy, 2006). This makes the droplets require a similar amount of activation energy to overcome the barrier of the wetting and dewetting movements induced by the pillars at the advancing and receding contact lines when being dragged. All of these results have similar advancing angles (153° and 158°), and distorted angles at the back (98° and 105°) in the parallel and orthogonal directions respectively, as shown in Figure 4.12(c). Therefore, the differences between the advancing angle and the distorted angle at the back in the two directions are similar (55° and 53°).

Regarding the flat surface, the droplet under the complete wetting state was only distorted but did not move at the advancing and receding contact lines when being dragged, as shown in Figure 4.12(a). This implies that the adhesion force between the droplet and the surface is much higher than that between the syringe and the droplet. Thus, this leads to the droplet with a 88.3° average static contact angle remaining in its original position, and results in the distorted angle at the

front (92°), and the distorted angle at the back (77°). It is believed that the droplet wetting state is the dominant factor in this case.

4.3.6 Sliding Angle Measurement

To investigate the droplet mobility on the sample surfaces, sliding angle measurements were conducted on a flat surface, a grooved surface, and a pillar surface. Sliding behaviour of a water droplet on a sample surface is a fundamental aspect of wettability (Lv et al., 2010; Miwa et al., 2000). The sliding angle is the characteristic of contact angle hysteresis of the sample surface. The sliding angle is defined as the angle at which the droplet starts to move on the sample. During the sliding angle measurement, a $10\mu\text{l}$ water droplet was firstly deposited on the sample surface on a computer-controlled tilting stage in the horizontal position. The tilting angle was then increased until the droplet rolled off the surface. Figure 4.13 shows snapshots of the videos that recorded the sliding angle measurement of various sample surfaces. With respect to the flat COC surface, the water droplet did not slide, even at a 90° tilting angle, as shown in Figure 4.13(a). However, the water droplet on the grooved surface started to slide at 24° in the parallel direction, as shown in Figure 4.13(b). Compared with the grooved surface, the water droplet on the pillar surface did not slide, even at a 90° tilting angle, as shown in Figure

4.13(c). This reveals that the water droplet under the Cassie and Baxter regime still forms a solid-liquid-air interface with the micro-directional grooved surface due to the shape edge of the ridges during the tilting process, as shown in Figure 4.13(b).

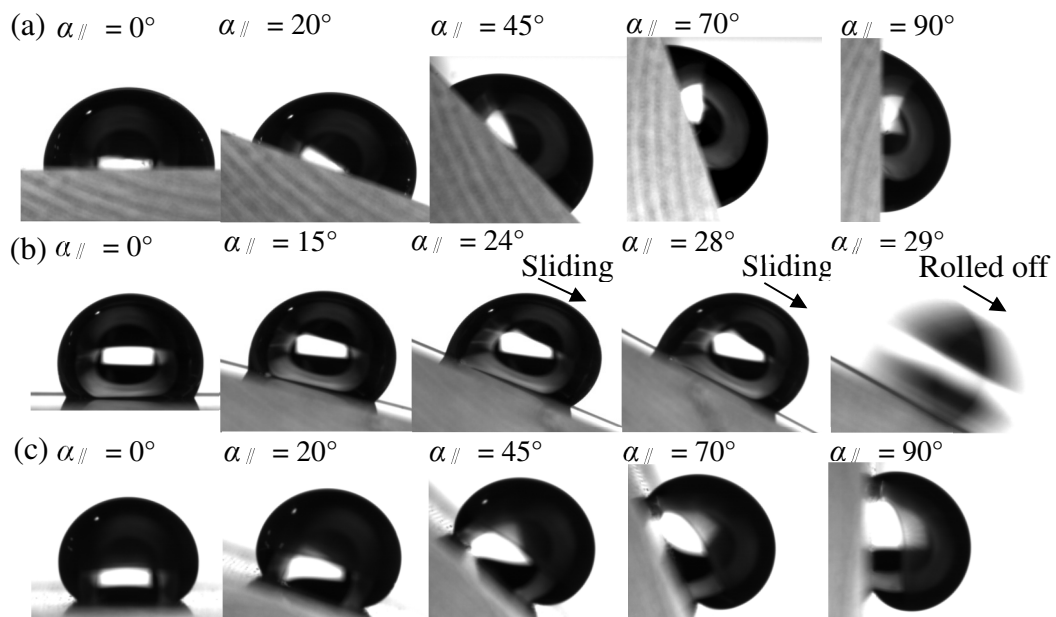


Figure 4.13 Snapshots of water droplets acting on the inclined (a) flat surface, (b) micro-grooved surface in the parallel direction, and (c) micro-pillar surface.

The sliding mechanism of a water droplet on micro-pillar surfaces is completely different from that on micro-directional grooved surfaces. The water droplet on the micro-pillar surface experiences a discrete wetting and dewetting process at the advancing and receding contact lines respectively due to the spacing between the pillars, the water droplet on the micro-directional surface experiences a continuous wetting and dewetting process which is related to the inertia of the

droplet when sliding on the continuous ridges in the parallel direction. Thus, discontinuous advancement of the droplet caused by the spacing between the pillars induced energy barrier results in the droplet not sliding on the inclined micro-pillar surface, even at a 90° tilting angle. However, the water droplet on the micro-grooved surface slides at 24° in the parallel direction due to the free advancement of the droplet on the continuous ridges.

Tilting a sample to an inclined angle is a dynamic situation which is different from the static contact angle measurement by the sessile drop method. Theoretically, although the contact area between the water droplet and the pillar surface is less than that on the grooved surface, one of the edges of the micro-pillars may act as an opposite force on an inclined surface to the sliding direction of the water droplet. This may greatly increase the friction acting on the water droplet. Additionally, the geometries of the micro-pillar surface provide more spacing for water droplet penetrating between the pillars. This may trigger the collapse of the droplet and its wetting state transits from the Cassie and Baxter regime to the Wenzel regime during tilting. All these results show that a water droplet on both the flat and the micro-pillar surface does not slide even at a 90° tilting angle, whereas a water droplet on the micro-grooved surface slides at 24° in the parallel direction. More importantly, the results from the sliding angle

measurement are consistent with those from the contact angle hysteresis measurement.

4.4 Summary

This chapter describes the wetting characteristics of bare hydrophobic micro-patterned cyclic olefin copolymer surfaces machined by a one-step fabrication method, ultra-precision raster milling (UPRM), which is potentially applicable for mass production in plastic injection molding. Due to the sharp edges induced by the numerical-controlled tool path of the material removal process in mechanical machining, the area fraction of the projected wet area on the micro-patterned surfaces can be defined accurately in the Cassie and Baxter model. This results in good agreement of the static contact angle predicted by the models with the measured static contact angle of the water droplet from the experiment. By studying the droplet anisotropy, and the interaction between droplet contact line and the micro-patterned surfaces, it is found that the water droplet governed by the Cassie and Baxter regime is stabilized by the shape edges at the top asperities of micro-grooves and micro-pillars after deposition on the sample surfaces. The experimental results from the contact angle hysteresis and sliding angle measurements show that a micro-directional grooved surface gives good sliding

performance which is important for the potential applications in microfluidic systems, such as artificial self-cleaning surfaces for mass production in plastic injection molding.

Chapter 5 Characterization of Intermediate Wetting States and Anisotropic Sliding on Micro-directional Grooved Surfaces

5.1 Introduction

This chapter discusses a characterization method which can identify various wetting states including partial wetting, droplet contact with the side walls of the grooves, complete wetting, and the Cassie and Baxter state from observation of the droplet contact line. It also covers the influences of the intermediate wetting states on the anisotropic sliding performance of the water droplet. Under the same area fraction of the projected wet area, bare micro-directional grooved surfaces with different groove widths and spacing were fabricated by ultra-precision raster milling (UPRM). According to observation of the droplet contact line, it was found that various wetting phenomena exist on micro-directional grooved cyclic olefin copolymer (COC) surfaces and polymethylmethacrylate (PMMA) surfaces with different surface geometries. By studying the droplet shape anisotropy, variation of the static contact angle against droplet deposition time, and comparison of the measured static contact angle with the Wenzel and the Cassie and Baxter models, various wetting phenomena have been identified. After characterization of the

droplet wetting states, the influence of the intermediate wetting states including partial wetting and droplet contact with the side walls of the grooves on anisotropic sliding performance of water droplet were investigated.

5.2 Experimentation

5.2.1 Fabrication of Micro-directional Grooved Surfaces using UPRM

Single point diamond turning (SPDT) was firstly employed to cut three sample surfaces at the same facing level in a Nanoform 200 machine. A Precitech Freeform 705G UPRM machine with a single crystal diamond faceted cutting tool, as illustrated in Figure 5.1(a), was then used to fabricate various periodic grooved surfaces of depth h , width w , spacing s , and an inclined angle β , as shown in Figure 5.1(b). Both horizontal and vertical cutting strategies of UPRM were applied to fabricate the grooves and the flat area at the top of the ridges respectively, on the micro-directional grooved surfaces with differences in the depth level of the h value (Cheng et al., 2016). Cyclic olefin copolymer (Topas COC, 5013LS-01) copolymerized from norbornene and ethylene using a metallocene catalyst and polymethylmethacrylate (PMMA) were chosen as the sample materials for this study due to the mediate hydrophobic nature of COC and the hydrophilic nature of PMMA. For the purpose of the experimental design, all the fabricated directional grooved COC samples had different groove width and spacing ($15\mu\text{m}$,

30 μm , and 45 μm) but the same f value (50%). The designed depth (h), width (w) and spacing (s) of the grooves on the three COC samples were 10 μm , 15 μm , 15 μm ; 10 μm , 30 μm , 30 μm ; and 10 μm , 45 μm , 45 μm respectively. It was expected that the designed dimensions of the surface geometries and the mediate hydrophobic property of COC would allow the droplets to have a wider range of wetting phenomena on the various micro-directional grooved surfaces in different directions, as illustrated in Figure 5.1(b). All the COC sheets used in the experiment were prepared by plastic injection molding. During the UPRM process, both the COC and PMMA sheets, of size 20mm \times 20mm \times 5mm, were machined to fabricate the micro-directional grooved surfaces based on the cutting conditions shown in Table 5.1. After the cutting process, ultra-sonic vibration was applied to clean any contamination from the sample surfaces in a water bath.

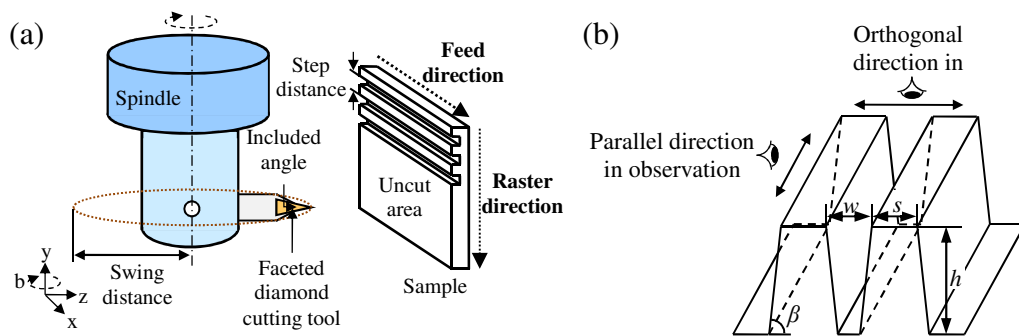


Figure 5.1 Schematic diagrams of (a) cutting geometry of UPRM, and (b) micro-periodic grooved surface.

Table 5.1 Cutting conditions.

Conditions	Details
Diamond tool	Single-crystal diamond
Tool type	Facet tool (5 μm and 14 μm width)
Included angle	30°
Spindle speed	4,000rpm
Depth of cut	4 μm
Swing distance	30.665mm
Feed rate	100mm/min
Step distance	0.05mm in vertical cutting strategy
Cutting strategy	Horizontal and vertical cutting
Cutting environment	Lubricant off

Table 5.2 Measurement data of the surface geometries on micro-directional grooved surfaces.

Material	Design depth, h (μm)	Design width, w (μm)	Design spacing, s (μm)	Measured depth, h (μm)	Measured width, w (μm)	Measured spacing, s (μm)	Measured angle, β (°)
COC	10	15	15	9.9	15.2	14.7	73.8
COC	10	30	30	9.9	30.3	29.9	73.5
COC	10	45	45	10.2	45.5	45.1	75.3
PMMA	9	15	5	9.8	15.2	5.1	74.8
PMMA	9	45	5	8.3	45.4	4.9	74.6

5.2.2 Micro-directional Grooved Surface Topography

After fabrication of the micro-directional grooved surfaces, their surface topographies were captured by a white light interferometer (Zygo Nexview), with 20x magnification, and a scanning electron microscope (Hitachi TM3000), with 500x magnification, as shown in Figure 5.2. It was found that the depth (h), width (w) and spacing (s) of the grooves on three COC samples were around 10 μm , 15 μm ,

15 μm ; 8 μm , 30 μm , 30 μm ; and 8 μm , 45 μm , 45 μm respectively. The inclined angle of the side walls of the ridges on all samples was around 75°. The deviation between each designed and measured dimension and the angle of the side walls were within $\pm 1\mu\text{m}$ and $\pm 1.5^\circ$ respectively, as shown in Table 5.2.

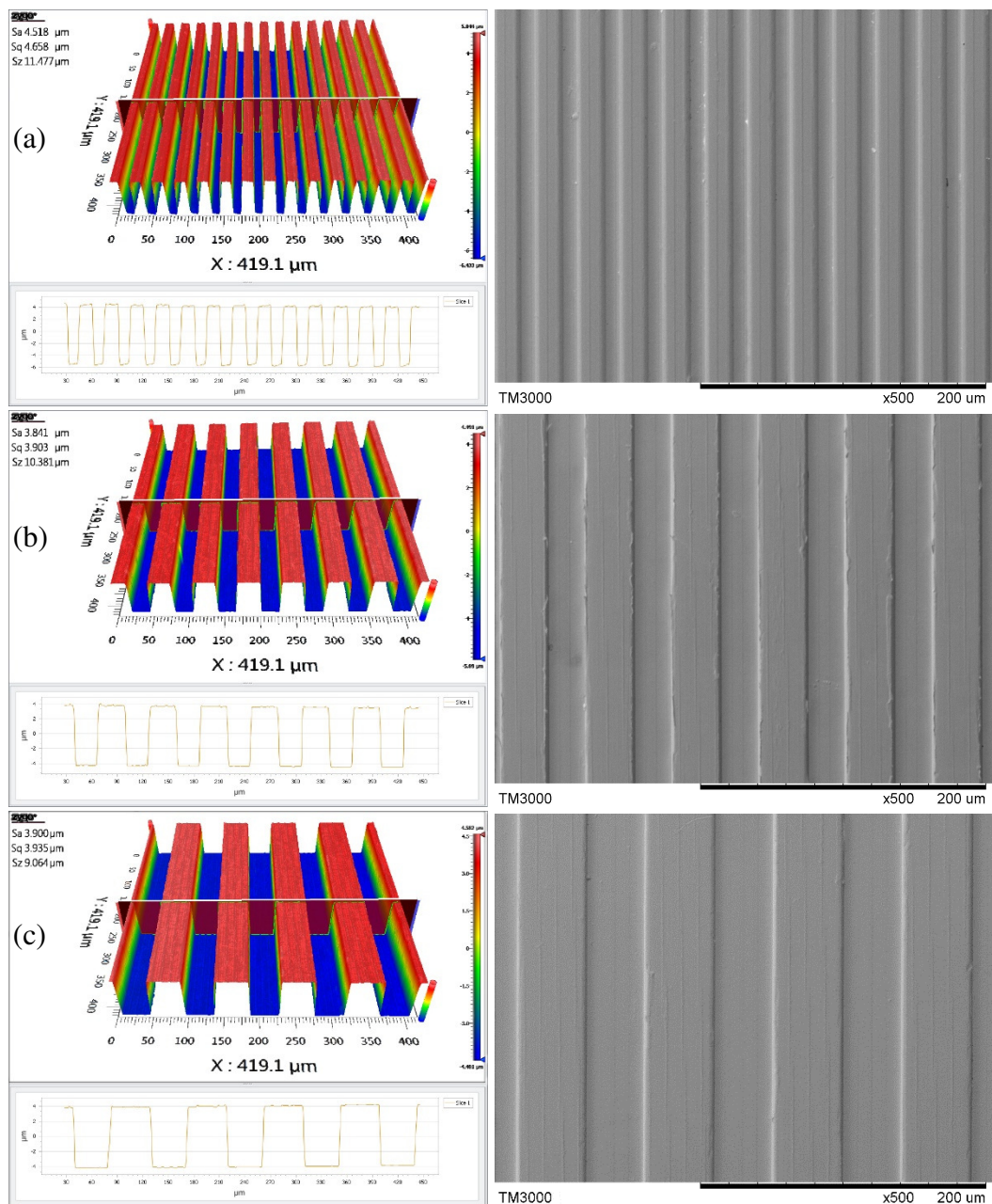


Figure 5.2 Surface topographies and SEM images of the directional grooved COC surfaces with (a) 15 μm , (b) 30 μm , and (c) 45 μm groove width and spacing.

5.3 Results and Discussion

5.3.1 Observation of Droplet Contact Line

Various possible droplet wetting states on the micro-directional grooved surfaces in the cross sectional view are illustrated in Figure 5.3. In order to investigate the anisotropic wetting behavior on micro-directional grooved surfaces, the droplet contour and contact line were observed from the top by 5x and 20x magnification respectively, using an optical microscope objective lens synchronized with a computer after a 5 μ l deionized water droplet was gently deposited onto the sample by a micro-syringe. Both the droplet contour and the contact line illustrate the interaction between the droplet and the surface geometry which can indicate the wetting behavior of droplets on micro-directional grooved surfaces.

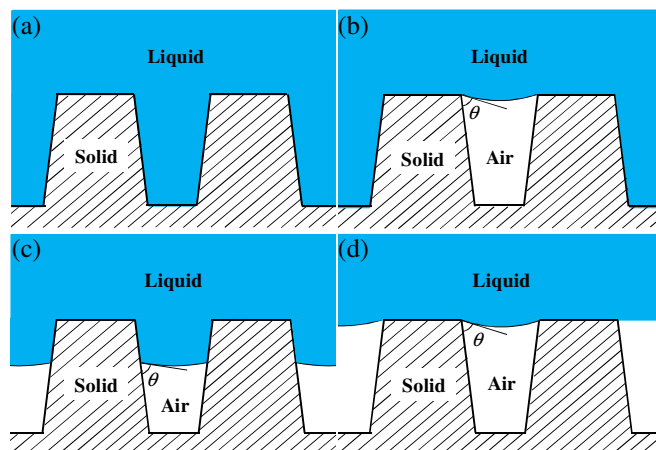


Figure 5.3 Schematic illustrations of a droplet (a) completely wetting in the Wenzel regime, (b) partially wetting, (c) contacting the side wall of the grooves, and (d) pinned at the top of the ridges in the Cassie and Baxter regime on micro-directional grooved surfaces.

Figure 5.4 shows the droplet contour and contact line on different micro-directional grooved surfaces. Various wetting phenomena were observed. It is known that the wetting transition can be triggered by external force or pressure, such as squeezing (Yao et al., 2010), vibration (Bormashenko et al., 2007), or impact (Bartolo et al., 2006). Thus, the various wetting phenomena could be caused by the squeezing of the droplet by the syringe or light vibration of the sample stage during the measurement. The droplet contact line is the magnification of the red-circled region of the droplet contour. Different arrows (see the remarks on Figure 5.4) represent different assumptions on the droplet wetting states.

On the 15 μm grooved surface, there are two different wetting phenomena, as shown in Figure 5.4(a) and 5.4(b). The droplet anisotropy shows that the shape of the droplet in Figure 5.4(a) is more rectangular than that in Figure 5.4(b), since the droplet may freely advance and elongate in the parallel direction after its deposition (Zhao and Law, 2012; Cheng et al., 2016). Figure 5.4(a) shows that the droplet contact line of the outer contour, indicated by the red diamond end arrows, becomes “sawtoothed”, right angled within the grooves. These imply that the droplet may have completely penetrated and wetted the bottom of the grooves on the sample surface, as illustrated in Figure 5.3(a).

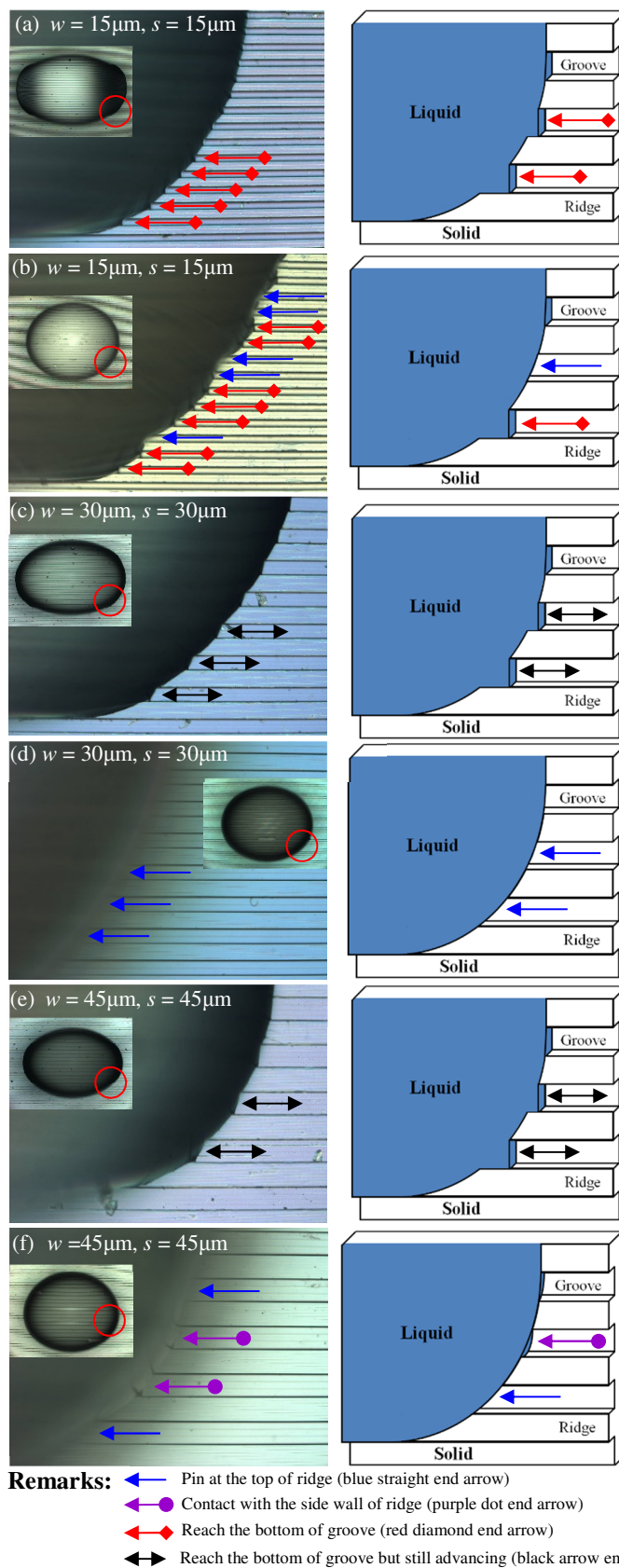


Figure 5.4 Images (left) and assumptions (right) of various droplet wetting states on droplet contact lines on micro-directional grooved COC surfaces.

This wetting transition to the Wenzel state may be triggered by the squeezing of the droplet by the syringe during its deposition (Yao et al., 2010). Thus, it results in a similar elongation to a droplet on a polymer coated micro-grooved PDMS in the literature (Tanaka et al., 2013). On the other hand, the shape of the droplet contour in Figure 5.4(b) is more circular. As indicated by the blue straight end arrows and the red diamond end arrows, part of the contact lines follows the contour of a regular ellipse but others become “sawtoothed” at right angles, as illustrated in Figure 5.4(a). These imply that part of the contact lines may be stably suspended on the grooves as the droplet is pinned at the top of the ridges on the near sides, whereas others may have completely penetrated and wetted the bottom of the grooves, as illustrated in Figure 5.3(b). This result is similar to the partial wetting phenomenon on the micro-grooved aluminum surface shown in the literature (Sommers and Jacobi, 2008). On both the 30 μm and 45 μm grooved surfaces, there are two different wetting phenomena, as shown in Figure 5.4(c), 5.4(d), 5.4(e) and 5.4(f) respectively. From observation of the droplet contact line in Figure 5.4(c) and 5.4(e), the droplet contour become “sawtoothed”, with obtuse angles of the contact line indicated by black arrow end arrows. These imply that the droplet may start to contact the side walls of the grooves after its deposition and having reached the bottom of the grooves, as illustrated in Figure 5.3(a). This

result is similar to the simulation result in the literature which showed a non-circular shape of the contact line on a micro-grooved surface that completely wetted the surface but had not yet reached the lowest surface energy in its equilibrium (Chen et al., 2005).

On the other hand, the droplet contours shown in Figure 5.4(d) and 5.4(f) are more circular. The contact lines in the regions indicated by blue straight end arrows are very smooth and follow the contour of a regular ellipse, whereas the contact lines indicated by purple dot end arrows show a small contact with the side walls of the grooves. These imply that the droplet may be stably suspended on the grooves as the droplet is mostly pinned at the top of ridges on both sides, as illustrated in Figure 5.3(d). However, some parts of the droplet make contact with the side walls of the grooves, as illustrated in Figure 5.3(c). Thus, the contact line shown in Figure 5.4(d) stably forms a solid-liquid-air interface which is governed by the Cassie and Baxter regime, as illustrated in Figure 5.3(d) resulting in a similar droplet contour on a bare micro-grooved PDMS which is under composite wetting state in the literature (Tanaka et al., 2013). In addition, the contact line indicated by purple dot end arrows, as shown in Figure 5.4(f), makes contact with the side walls of the grooves. This wetting phenomenon is similar to a reported computational result using the minimum energy path method. The water droplet

on some individual grooves was in an unstable wetting state and contacting the side walls of the grooves (Bartolo et al., 2006).

To validate the assumption of the contact line under complete wetting shown in Figure 5.4(a), 5.4(c) and 5.4(e), droplet contact lines on two micro-directional grooved PMMA, with a smaller value of groove spacing ($s=5\mu\text{m}$), were observed. This narrow groove spacing is to ensure that the droplets completely wet the bottom of the grooves on these two surfaces, with less support by the ridges, in a hydrophilic material. It is found that the wetting phenomena shown in Figure 5.5(a) and 5.5(b) are the same as the wetting phenomena shown in Figure 5.4(a), 5.4(c) and 5.4(e) respectively. These show that the droplet contact lines shown in Figure 5.4(a), 5.4(c) and 5.4(e) completely wet the micro-grooved COC surfaces, which is similar to both the simulation and experimental results in the literature (Chen et al., 2005; Kooij et al., 2012).

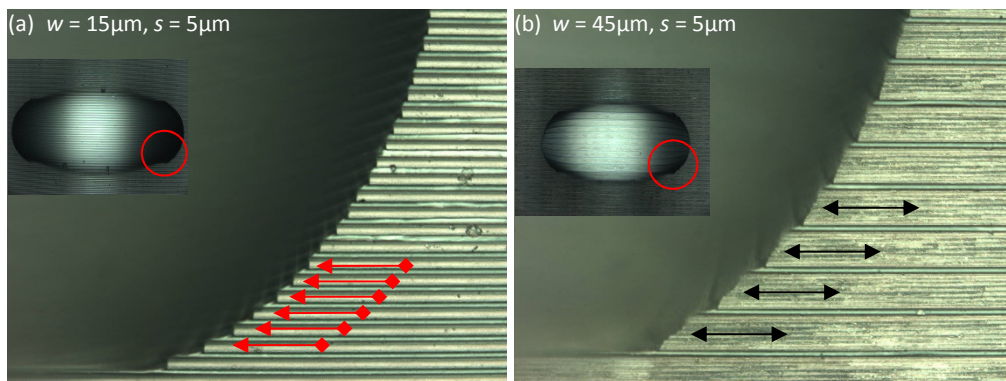


Figure 5.5 Wetting phenomena of droplet contact lines on micro-directional grooved PMMA surfaces.

In order to further identify the wetting phenomena, investigations of the anisotropic wetting behavior on micro-directional grooved COC surfaces, including variation of the static contact angle against droplet deposition time, and comparison of the measured static contact angle with the Wenzel and the Cassie and Baxter model, were conducted. After identification of the various wetting states, the influence of the intermediate wetting states on sliding performance of water droplet was determined.

5.3.2 Plot of Static Contact Angle against Droplet Deposition Time

To further identify the wetting states on the droplet contact line, the static contact angle of a deionized water droplet, of approximate volume 5 μ l, using the sessile method, was plotted against the droplet deposition time. The change of the static contact angle can be observed using a Sindatek model 100SB goniometer, which consists of a camera, a computer-controlled automatic liquid deposition unit, a computer-controlled tilting stage, and computer-based image-processing software called Magic Droplet. The angle was found by the computer software by determining the tangent line at the contact points optically, with a deterministic error of $\pm 0.1^\circ$. Figure 5.6 shows the representative static contact angle, θ , plotted against the droplet deposition time on different samples in the parallel direction,

θ_{\parallel} and in the orthogonal direction, θ_{\perp} as shown in Figure 5.1(b).

As illustrated in the graphs of Figure 5.6(a), the local static contact angle of the droplets on the 15 μm grooved surface in the parallel direction, θ_{\parallel} , keeps decreasing and becomes stable 10s to 15s after the droplet deposition, and reaches 91.3° and 106.2° respectively. This means that the droplets tend to an equilibrium state after 10s to 15s after droplet deposition on the sample surfaces. This may be because the droplet, in the case of a static contact angle of 91.3°, may reach the bottom of the grooves and advance along the grooves but is opposed by the friction of the side walls under a metastable state due to the relatively narrow groove width (i.e. 15 μm), as shown in Figure 5.2(a). Thus, the droplet needs 10s to reaches a relatively stable equilibrium state, as illustrated in Figure 5.3(a). This is consistent with other findings in the literature which showed that the droplet has not yet reached its ground energy level during the wetting transition to the Wenzel regime in equilibrium but completely wetted the bottom of the grooves (Chen et al., 2005; Pashos et al., 2015).

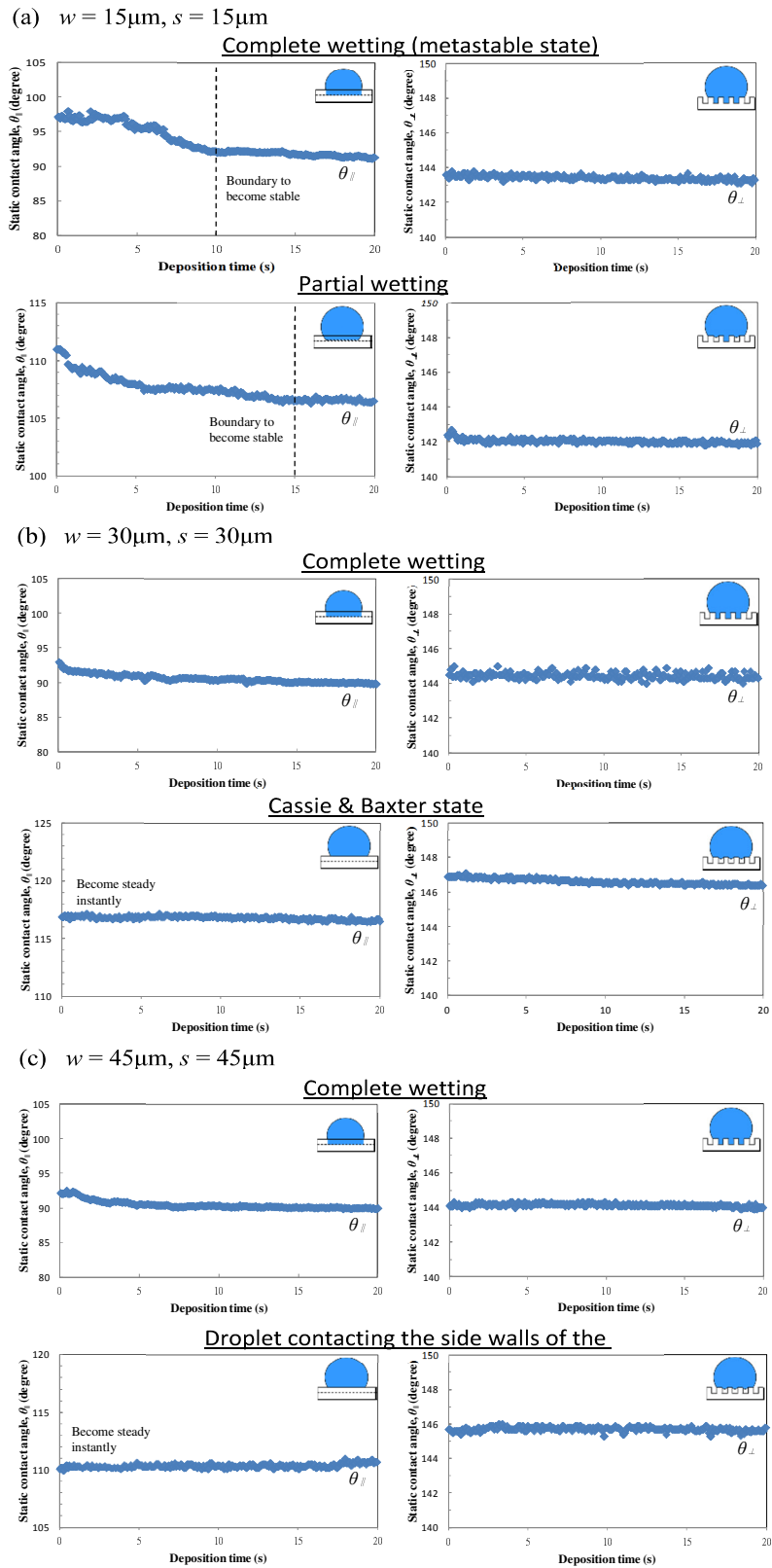


Figure 5.6 Representative static contact angles, θ plotted against the droplet deposition time on the sample surface with (a) $15\mu\text{m}$, (b) $30\mu\text{m}$, (c) $45\mu\text{m}$ groove width and spacing in the parallel direction (left) and the orthogonal direction (right).

The droplet, in the case of a static contact angle of 106.2° , needs 15s to reach a relatively stable equilibrium state. This may be because parts of the droplet reach the bottom of the grooves but other parts are pinned at the top of the ridges. In other words, the droplet may partially wet the surface, as illustrated in Figure 5.3(b). Thus, the droplet needs a relatively longer time (15s) to reach an equilibrium state and results in a relatively high static contact angle (106.2°). This experimental result is consistent with other findings in the literature which showed that the droplet partially wetted the grooved surface (Sommers and Jacobi, 2008).

The local static contact angle of the droplet on the $30\mu\text{m}$ grooved surface in the parallel direction, θ_{\parallel} , becomes instantly stable (within 1s) after deposition and reaches 90.1° and 116.8° respectively, as shown in Figure 5.6(b). This means that the droplet tends to an equilibrium state within a very short time. This may be because the droplet, in the case of a static contact angle of 90.1° , reaches the bottom of the grooves, as shown in Figure 5.3(a). A wider groove width ($30\mu\text{m}$) provides more spacing for the droplet to freely advance within the grooves, compared with the $15\mu\text{m}$ grooved surface. Thus, the droplet reaches its ground energy level within a shorter time. This is different from the droplet in the case of a static contact angle of 91.3° on the $15\mu\text{m}$ grooved surface that needs around

10s to reaches a relatively stable equilibrium state. The droplet in the case of a static contact angle of 116.8° becomes steady instantly (within 1s). Based on the relatively high measured value of the static contact angle, this implies that the droplet is pinned at the top of the ridges on the grooved surface once it is deposited, following the Cassie and Baxter regime, as illustrated in Figure 5.3(d). This experimental result is consistent with other findings in the literature which showed that the static contact angle of the droplet on a grooved polystyrene surface in the parallel direction followed the Cassie and Baxter regime (Zhang and Low, 2007).

The local droplet on the $45\mu\text{m}$ grooved surface in the parallel direction, θ_{\parallel} , becomes stable after deposition and reaches 89.9° and 110.2° respectively as shown in Figure 5.6(c). The static contact angle of 89.9° is similar to that of the $30\mu\text{m}$ grooved surface of 91.3° possibly caused by both droplets being under complete wetting. The static contact angle of 110.2° on the $45\mu\text{m}$ grooved surface is lower than that in the 116.8° case for the $30\mu\text{m}$ grooved surface. This implies that some parts of the droplet on the $45\mu\text{m}$ grooved surface may contact the side walls of the grooves, as indicated in Figure 5.4(f). This results in a decrease of the static contact angle since the area fraction of the projected wet area increases.

All the static contact angles on the various sample surfaces in the orthogonal direction, θ_{\perp} , become instantly steady after deposition on the $15\mu\text{m}$, $30\mu\text{m}$ and

45 μ m grooved surfaces. This shows that the energy barrier induced by the pinning effect from the sharp edge of the ridges stabilizes the droplet spreading in the orthogonal direction, regardless of the droplet state (the Wenzel regime, the Cassie and Baxter regime, droplet contact with the side walls of the grooves, or partial wetting) (Cheng et al., 2016; Neuhaus et al., 2012).

In summary, the results from the plots of static contact angle, θ , against the deposition time of a droplet on the micro-grooved surface in the parallel direction are in agreement with the various wetting states characterized from observation of the droplet contact line, and provide more detailed information on anisotropic wetting behaviour. However, it is limited to identifying the droplet wetting state in the orthogonal direction due to the pinning effect induced by the sharp edges of the ridges.

5.3.3 Comparison with the Theoretical Models

A comparison between the average static contact angle from the experiments and the models were made to further identify the various wetting states on the droplet contact line. Wenzel developed a model (1936) to describe a droplet on a rough surface in a completely wetted homogeneous state, with a solid-liquid interface, as illustrated in Figure 5.3(a). To apply this equation for predicting the

static contact angle on a rough surface, the surface should be completely wetted by the droplet and reach its ground energy level after the wetting transition. The static contact angle of a droplet in the Wenzel regime, θ_w , can be calculated as follows:

$$\cos \theta_w = r \cos \theta_Y \quad (5-1)$$

where r is the roughness ratio on the rough surface, and θ_Y is the static contact angle of a droplet on a flat surface.

Cassie and Baxter (1944) modified the Wenzel model to describe a droplet on a heterogeneous surface with a solid-liquid-air interface, as illustrated in Figure 5.3(d). The area fraction of the projected wet area should be defined clearly. If a droplet is under partial wetting or contacting the side walls of the grooves on the sample surface, as illustrated in Figure 5.3(b) and 5.3(c) respectively, it will lead to a discrepancy in the prediction by the model. The static contact angle of a droplet in the Cassie and Baxter regime, θ_{CB} , can be calculated as follows:

$$\cos \theta_{CB} = R_f f \cos \theta_Y + f - 1 \quad (5-2)$$

where f is the area fraction of the projected wet area, and R_f is the roughness ratio on the wet area. The roughness ratio R_f on the wetting area of the top asperities on all the micro-directional grooved surfaces is assumed to be 1 in Eq. 5-2, since the

top and the edge of the ridges of the samples fabricated by UPRM are relatively smooth and sharp, as shown in the topographies in Figure 5.2.

Table 5.3 summarizes the average static contact angles of the water droplets on various COC fabricated surfaces, including a flat COC surface machined by a Moore Nanotech 350FG single point diamond turning machine in two directions, as illustrated in Figure 5.1, 20s after deposition of the droplet by a goniometer. Each reported data is an average of six to eight independent measurements, with a standard deviation of ± 2 . The static contact angle of the flat surface is about 88.3° , which is consistent with the findings of previous studies (Jena, et al., 2012).

Figure 5.7 illustrates the images of sessile water droplets on a COC flat surface and different micro-directional grooved COC surfaces, captured in the parallel and the orthogonal directions. Isotropic and anisotropic wetting behaviour can also be observed in the water droplets on the flat surface and the micro-directional grooved surfaces respectively. The droplets on a flat surface machined by ultra-precision diamond turning are circular in shape, from the top view, as shown in Figure 5.7(a). The shape of the droplets under the Cassie and Baxter state or when contacting the side walls of the grooves on the $30\mu\text{m}$ and $45\mu\text{m}$ grooved surface are nearly circular, whereas the shape of the droplets on other micro-directional grooved surfaces under the Wenzel regime or partial wetting are more

elliptical. The droplet in the Wenzel state on the 15 μm grooved surface is even rectangular in shape. This means that the surface geometry parameters not only control the anisotropy of the droplet shape and wetting direction, but the droplet wetting states on the sample surface also affect it.

Table 5.3 Deionized water contact angle data on micro-directional grooved COC surfaces.

Surface geometries (w, s)	Observation direction	Average static contact angle, θ	θ_{CB}	θ_W	Sliding angle, α
15 μm	Parallel	$\theta_{\parallel} = 88.6^{\circ} \pm 2.0$	119.0 $^{\circ}$	87.5 $^{\circ}$	Not slide
	Orthogonal	$\theta_{\perp} = 143.2^{\circ} \pm 1.2$	119.0 $^{\circ}$	87.5 $^{\circ}$	Not slide
30 μm	Parallel	$\theta_{\parallel} = 113.6^{\circ} \pm 2.1$	119.0 $^{\circ}$	87.9 $^{\circ}$	$\alpha_{\parallel} = 35^{\circ}$
	Orthogonal	$\theta_{\perp} = 145.9^{\circ} \pm 1.8$	119.0 $^{\circ}$	87.9 $^{\circ}$	Not slide
45 μm	Parallel	$\theta_{\parallel} = 108.9^{\circ} \pm 1.6$	119.0 $^{\circ}$	88.0 $^{\circ}$	$\alpha_{\parallel} = 24^{\circ}$
	Orthogonal	$\theta_{\perp} = 145.9^{\circ} \pm 1.5$	119.0 $^{\circ}$	88.0 $^{\circ}$	Not slide
Flat	-	$\theta = 88.3^{\circ} \pm 1.9$	-	-	Not slide

The average static contact angle of the droplets at 101.0 $^{\circ}$ and 93.9 $^{\circ}$ on the 15 μm and 45 μm grooved surface respectively in the parallel direction, as shown in Figure 5.7(b) and 5.7(d), are not even close to the values predicted by the Wenzel model (87.5 $^{\circ}$ /88.0 $^{\circ}$) and the Cassie and Baxter model (119.0 $^{\circ}$). These may be caused by the droplet, in the case of a static contact angle of 101.0 $^{\circ}$, being under partial wetting, and the droplet in the case of a static contact angle of 93.9 $^{\circ}$ completely wets the grooves but has not yet reached its ground energy level on the contact line during the wetting transition to the Wenzel state (Chen et al., 2005; Pashos et al.,

2015). Thus, the complete wetting state of the droplet further decreases the static contact angle of the droplet when compared with the one under partial wetting, since the area fraction of the projected wet area (f value) in Eq. 5-2 increases. Some researchers have also reported this deviation of the static contact angle predicted by the Wenzel equation (Tanaka et al., 2013; Erbil and Cansoy, 2009; Gao and McCarthy, 2009; Gao and McCarthy, 2007). Although the droplet reaches the bottom of the grooves, the droplet contact line opposed by the friction on the grooved surface can still advance very slowly, and the contact area therefore does not reflect the ground state of energy of the contact line during the transition from the Cassie and Baxter state to the Wenzel state (Murakami et al., 2014). This explains why the droplet, under a complete wetting state, has a higher static contact angle compared to the one predicted by the Wenzel model.

In the cases of the average static contact angles of the droplets of 88.6° and 88.1° on the $15\mu\text{m}$ and $45\mu\text{m}$ grooved surface respectively, in the parallel direction, as shown in Figure 5.7(b) and 5.7(c), the angles 88.6° and 88.1° were nearly equal to the values predicted by the Wenzel model ($87.5^\circ/88.0^\circ$), as shown in Figure 5.8. This proves that the droplet reaches the bottom of the grooves and has reached its ground energy level on the contact line during the wetting transition to the Wenzel state.

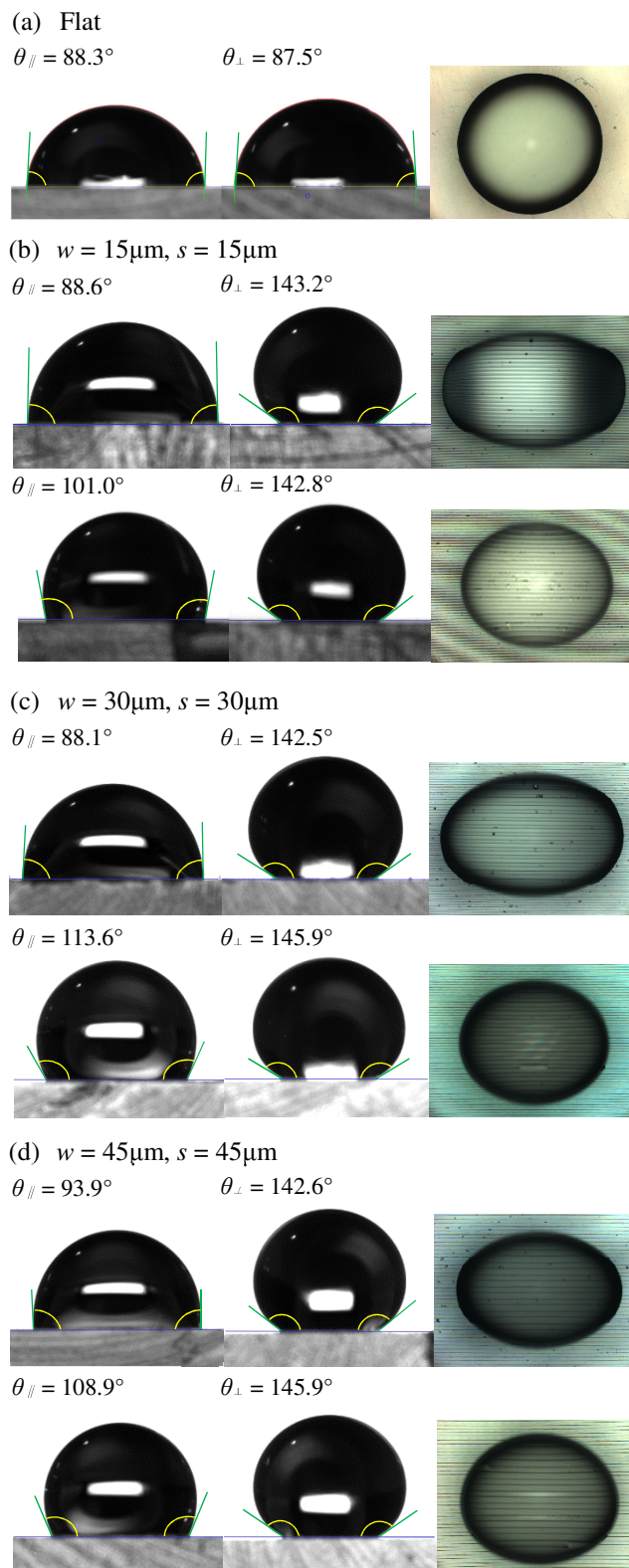


Figure 5.7 Images and schematics of a water droplet in contact with (a) flat COC surface, (b) 15µm, (c) 30µm, (d) 45µm groove width and spacing of directional grooved COC surfaces captured from side and top views.

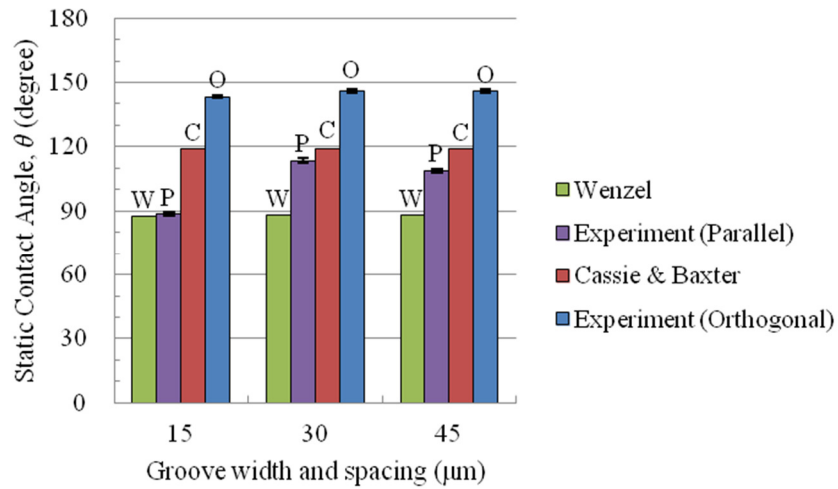


Figure 5.8 Comparison of the static contact angles of water measured on grooved COC surfaces in the parallel and orthogonal direction to the Wenzel model as well as the Cassie and Baxter model.

In the cases of the average static contact angles of the droplets of 113.6° and 108.9° on the $30\mu\text{m}$ and $45\mu\text{m}$ grooved surface respectively, in the parallel direction, as shown in Figure 5.7(c) and 5.7(d), 113.6° is close to the calculated values from the Cassie and Baxter model (119°) as shown in Figure 5.8. Similar to the finding reported in the literature, the droplets are governed by the Cassie and Baxter regime (Zhang and Low, 2007). However, 108.9° deviates from the calculated values from the Cassie and Baxter model (119°). This may be caused by part of the droplet on the $45\mu\text{m}$ grooved COC surface, as shown in Figure 5.7(d) making contact with the side walls of the grooves, as indicated by the purple arrows in Figure 5.4(f). This results in a decrease in the static contact angle since the area fraction of the projected wet area (f value) in Eq. 5-2 increases.

All the static contact angles of the droplets on micro-directional grooved surfaces in the orthogonal direction, θ_{\perp} , are approximately 145° which is far away from the values calculated from the Wenzel model or the Cassie and Baxter model, as shown in the bar chart in Figure 5.8. It was reported that neither the Wenzel equation nor the Cassie and Baxter equation can describe the weak dependency of the static contact angle of a droplet in the orthogonal direction in regard to the periodicity of the micro-patterns on both bare and sP(EO-stat-PO)-coated PDMS substrates in various surface geometries (Zhao et al., 2011). It is known that a potential free-energy barrier is formed on a groove, and induces the pinning of the fluid at the edge of the solid strips which results in the high static contact angle in the orthogonal direction, θ_{\perp} (Chen et al., 2005; Zhao and Law, 2012; Cheng et al., 2016). More importantly, both the results from the change of static contact angle against its deposition time, and the comparison of the average static contact angle with the theoretical models provide evidence that the characterization method by the droplet contact line can successfully identify various wetting states, including the intermediate wetting states.

5.3.4 Anisotropic Sliding Behavior

The sliding angle is one of the major measures to quantify the performance of droplet mobility on sample surfaces (Lv et al., 2010; Miwa et al., 2000). Anisotropic sliding behavior of water droplets was studied on various micro-directional grooved COC surfaces under the same area fraction of the projected wet area. The sliding test is aimed at showing the influence of the intermediate wetting states under partial wetting and droplet contact with the side walls of the grooves on the sliding performance of water droplets on micro-directional grooved surfaces. This can also enable investigation of the effect of micro-directional grooved COC surfaces with different groove widths and spacing, but under the same area fraction of the projected wet area to the anisotropic sliding performance. The sliding angle measurement was conducted by tilting the sample stage at a constant rate of $1^\circ/\text{s}$ with a $10\mu\text{l}$ deionized water droplet on the sample surface. The sliding angle is defined as the minimum angle at which the advancing and receding contact lines of the droplet start to move or slide from the original position.

Figure 5.9 shows snapshots of a $10\mu\text{l}$ droplet captured on flat and micro-grooved COC surfaces with $15\mu\text{m}$, $30\mu\text{m}$ and $45\mu\text{m}$ groove widths and spacing respectively, during the tilting process in the parallel direction. In order to identify

the wetting states of various droplets before the sliding angle measurement, the static contact angles and the droplet contact lines on various micro-grooved surfaces were measured and observed. It was found that the static contact angles on different samples when $\alpha_{\parallel} = 0^{\circ}$, as shown in Figure 5.9, are almost equal to 89° , 102° , 113° , and 109° , which are consistent with the findings shown in Figure 5.7. From observation of the droplet contact lines, the wetting states of the droplets on the micro-grooved COC surfaces with $15\mu\text{m}$, $30\mu\text{m}$ and $45\mu\text{m}$ groove widths and spacing are under complete wetting, partial wetting, the Cassie and Baxter regime, and contacting the side walls of the grooves respectively.

The experimental data show that the water droplet under a complete wetting state on the $15\mu\text{m}$ grooved COC surface only advanced but did not recede, even when tilted upright, as shown in Figure 5.9(b). The reason is that the droplet on the grooved surface forms a solid-liquid interface which greatly increases the contact area between the droplet and the sample surface when compared with the flat COC surface shown in Figure 5.9(a). Thus, the gravitational force acting on the droplet cannot overcome the adhesion force between the droplet and the sample surface on the receding contact line during tilting. This leads to the droplet being elongated due to advancing only, but is still stuck on the sample surface even when

tilted upright which is similar to that on the flat COC surface shown in Figure 5.9(a).

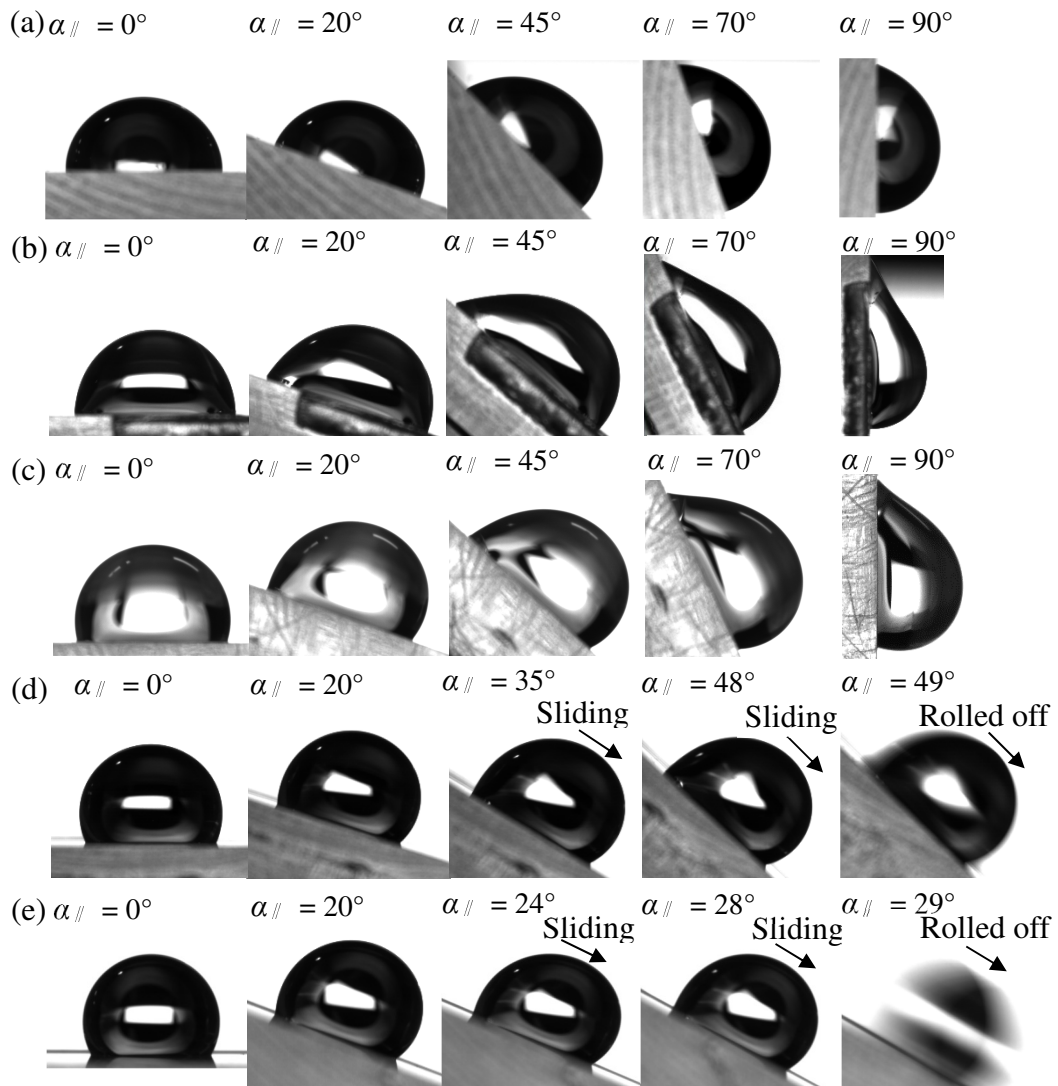


Figure 5.9 Snapshots of a water droplet (a) under complete wetting on the flat surface, (b) under complete wetting on the 15µm grooved surface, (c) under partial wetting on the 15µm grooved surface, (d) under the Cassie-Baxter state on the 30µm grooved surface, and (e) contacting the side walls of the 45µm grooved surface during the sliding measurement in the parallel direction.

Regarding the droplet under partial wetting on the 15 μm grooved COC surface, the droplet advanced and receded very slowly when tilted upright but still stuck to the sample surface, as shown in Figure 5.9(c). The reason is that, although parts of the droplet contact lines are pinned at the top of the ridge as indicated by the blue straight end arrows and form solid-liquid-air interfaces, other droplet contact lines completely wet the bottom of the grooves as indicated by the red diamond end arrows and form solid-liquid interfaces. Thus, the gravitational force acting on the droplets during the tilting process still cannot overcome the resultant adhesion force between the droplet and the sample surface. This results in the droplet just being elongated on the grooved surface, even when tilted upright. Figure 5.10 provides evidence that the droplet under a partial wetting state on the 15 μm grooved COC surface still remained its partial wetting state, and water stains were left in some grooves behind the receding contact line on the sample surface, after being tilted upright.

In respect to the droplet under the Cassie and Baxter regime on the 30 μm grooved surface and the droplet in contact with the side walls of the grooves on the 45 μm grooved surface, the droplet on the 30 μm grooved surface slid at 35° and rolled off at 49°, as shown in Figure 5.9(d), and the droplet on the 45 μm grooved surface slid at 24° and rolled off at 29°, as shown in Figure 5.9(e). These imply

that the droplets governed by the Cassie and Baxter regime or contacting the side walls of the grooves on the 30 μm and 45 μm grooved surfaces did not collapse during the tilting, sliding and roll-off processes. It is believed that the wetting state of a droplet is a dominant factor in determining the droplet sliding ability on micro-directional grooved surfaces (Bormashenko, 2015; Bhushan and Jung, 2011; Bhushan et al., 2009). Therefore, both the droplet contact lines under a composite wetting state still remain solid-liquid-air interfaces during the tilting process. The composite wetting state greatly reduces the contact area and the adhesion force between the droplets and the sample surface, and result in the droplet sliding and rolling off from the surfaces.

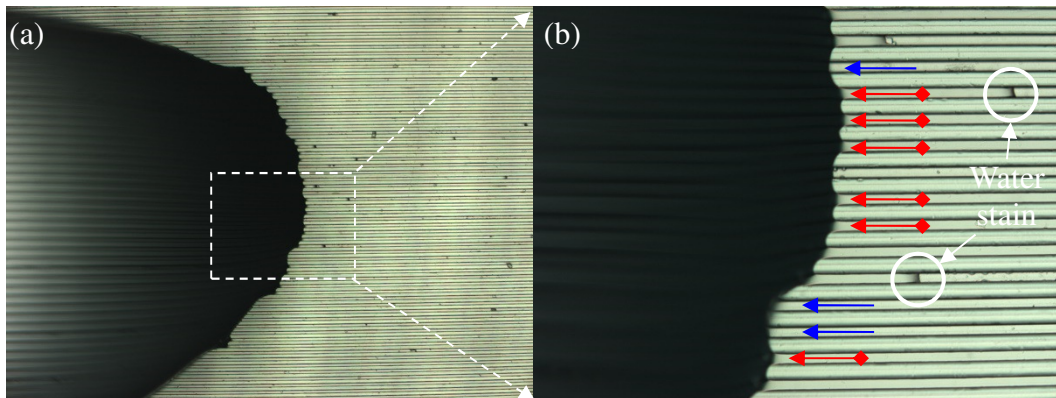


Figure 5.10 Receding contact lines of a droplet under partial wetting state after tilting a 90 degree on the 15 μm grooved COC surface in (a) 5x magnification, and (b) 20x magnification.

Nevertheless, the experimental data indicate that the sliding angle of a water droplet on the 45 μm grooved surface (i.e. $\alpha_{\parallel} = 24^{\circ}$) is lower than that of the 30 μm grooved surface (i.e. $\alpha_{\parallel} = 35^{\circ}$) along the groove axes, as shown in Figure 5.9. This reveals that the area fraction of the projected wet area, the f value, may not be the key factor affecting the sliding angle of a droplet on micro-directional grooved surfaces, as the f value of both samples are the same (i.e. 50%) but, rather, the groove width and spacing is the key factor. Friction is believed to be the major obstacle to droplet mobility on rough surfaces (Cheng et al., 2016; Lv et al., 2010; Nosonovsky, 2007). In this case, wider groove widths and spacing in a geometric design may decrease the friction of the grooved surface along the grooves' axes per unit area, resulting in a lower sliding angle of the droplet.

Interestingly, droplets on 30 μm and 45 μm grooved surfaces experience different sliding durations. The droplets on the 30 μm grooved surfaces keep sliding when the tilting angle increases from 35° to 48° , within 13s, and then roll off at 49° . On the other hand, droplets on the 45 μm grooved surfaces keep sliding when the tilting angle increases from 24° to 28° , within 4s, and then roll off at 29° . This implies that a water droplet on a wider groove width and spacing requires a shorter duration and a lower tilting angle to slide and roll off from the surface. As mentioned in a previous study, the sliding mechanism of a water droplet on the

micro-grooved surfaces in the parallel direction results in a continuous wetting and dewetting process at the droplet contact lines (Cheng et al., 2016). A wider groove width and spacing may decrease the friction acting on the droplet by the continuous ridges in the parallel direction during sliding. This leads to the droplet requiring less energy to overcome the barrier induced by the friction under the composite wetting state, sliding more easily on a wider groove width and spacing under the same area fraction of the projected wet area. More importantly, all of these show that, besides the Cassie and Baxter state, a droplet contacting the side walls of the grooves is still a favorable wetting state for anisotropic sliding on the micro-grooved surfaces, whereas partial wetting state represents the sliding boundary of micro-grooved surfaces.

5.4 Summary

A characterization method for droplet wetting states, significantly affecting sliding performance on hydrophobic surfaces, has been proposed from observations of the droplet contact lines on micro-directional grooved surfaces fabricated by UPRM. This characterization method is capable of identifying intermediate wetting states including partial wetting and droplets contacting the side walls of the grooves from the Cassie and Baxter state, which all have solid-

liquid-air interfaces, but it is difficult to use traditional verification methods for identification. By studying the droplet anisotropy, variation of the static contact angle against droplet deposition time, and comparison with the static contact angle predicted from the Wenzel and the Cassie and Baxter models, various wetting states characterized by the droplet contact lines, including partial wetting, droplet contact with the side walls of the grooves, complete wetting, and the Cassie and Baxter regime have been verified. The experimental results from anisotropic sliding measurement show that the partial wetting state is the sliding boundary of the micro-grooved surfaces, whereas a droplet contacting the side walls of the grooves is still a favorable wetting state for anisotropic sliding on the micro-directional grooved surfaces. It is also interesting to note that the groove width and spacing are key factors, resulting in different sliding angles and durations before roll-off from surfaces with the same area fraction of projected wet area (50%) in the parallel direction of the anisotropic sliding measurement. More significantly, it is believed that this research broadens understanding of the characterization of droplet wetting states, and identifies the sliding conditions of the immediate wetting states on the micro-grooved surfaces, which have huge potential in applications in microfluidic devices, such as artificial self-cleaning surfaces.

Chapter 6 Anisotropic Wetting of Micro-Micro Hierarchical Structures Fabricated by Ultra-precision Machining

6.1 Introduction

This chapter discusses the anisotropic wetting of bare micro-micro hierarchical structured surfaces fabricated by highly controllable one-step mechanical machining methods. Single layer microstructures such as micro-pillars and micro-grooves can achieve high static contact angles on both hydrophobic and hydrophilic materials. It has also been shown that micro-directional grooved surfaces can achieve good sliding performance (Cheng et al., 2016). However, the stability of the droplet composite wetting state on the surfaces may be a problem, since wetting transition can be triggered by external force or pressure, such as squeezing (Yao et al., 2010), vibration (Jung and Bhushan, 2009; Bormashenko et al., 2007), or impact (Jung and Bhushan, 2009; Bartolo et al., 2006). To increase the stability of the composite wetting state, scientists have tried to fabricate multi-layer structures, such as micro-nano (Rukosuyev et al., 2014; Shao et al., 2014; Guo et al., 2014; Radha et al., 2013; Li et al., 2013; Ebert and Bhushan, 2012; Feng et al., 2011; Kim et al., 2011; Boreyko et al., 2011; Bhushan et al., 2009) and

micro-micro hierarchical structured surfaces (Chu et al., 2014; Kang et al., 2013; Huovinen et al., 2012; Yang and Jiang, 2010; Zhang and Low, 2007) using various fabrication methods. It was reported that the stability of the droplet composite wetting state on micro-nano hierarchical structured surfaces increases compared with that on the single layer micro-pillar surface, due to the increase of the energy barrier for the wetting transition. However, most of the manufacturing processes are complicated in chemical treatment, time-consuming, not suitable for fabricating large surfaces, or only applicable to engineering materials such as metals, semiconductors, and alloys but are limited for plastics. Thus, there are very few methods that can be used to manufacture micro-nano or micro-micro hierarchical structured surfaces for mass production.

Mechanical machining would be one of the best solutions to fabricate bare hydrophobic micro-micro hierarchical structured surfaces with good sliding performance and stable composite wetting state for mass production, due to numerical control of machine tool path during the material removal process. Motivated by this, the present study aims to investigate the anisotropic wetting of micro-micro hierarchical structured surfaces fabricated by different ultra-precision machining methods in terms of measurement of the static contact angle, contact line, and sliding angle of the water droplet.

6.2 Regular Micro-Micro Hierarchical Structures Fabricated by UPRM

This section describes the wetting characteristics of regular micro-micro hierarchical structures fabricated by ultra-precision raster milling (UPRM).

6.2.1 Experimental Setup

Single-point diamond turning (SPDT) was employed to cut sample surfaces at the same level initially in a Nanoform 200 machine for preparing flat sample surfaces. This avoids the occurrence of varying depths of micro-micro hierarchical structures on a large area of the sample surface due to incorrect levels of different samples when machining the hierarchical structures. After the preparation, a Precitech Freeform 705G (Precitech Inc., USA) 5-axes CNC UPRM machine was used to generate the hierarchical structured surfaces on the sample surfaces, which were attached by a specially designed fixture. During the machining process, a single crystal diamond faceted cutting tool with 30° included angle and 14.0μm width of tool tip was selected and fixed to the spindle with a certain swing distance (Cheng et al., 2016). All the cutting conditions of UPRM, including spindle speed, depth of cut, swing distance, feed rate, step distance, and cutting environment are shown in Table 6.1. The workpiece material for this study was cyclic olefin

copolymer (Topas COC, 5013SL-01) which is copolymerized from norbornene and ethylene with a metallocene catalyst. All the 20mm x 20mm COC sheets used in the experiment were prepared by plastic injection molding from the raw material.

Table 6.1 Cutting conditions.

Conditions	Details
Tool type	Single-crystal diamond facet tool (14.0 μ m Width)
Included angle	30°
Spindle speed	4,000rpm
Depth of cut	Last depth of cut in 4 μ m
Swing radius	30.665mm
Feed rate	100mm/min
Step distance	0.05mm in vertical cutting strategy
Cutting strategy	Horizontal and vertical cutting
Cutting environment	Lubricant off

6.2.2 Fabrication of Regular Micro-Micro Hierarchical Structures

After consideration of the cutting efficiency and surface quality, a micro-directional grooved surface of 10 μ m depth, 45 μ m width, 45 μ m spacing, and a 75° angle were fabricated by tool path planning for surface generation. Due to the dimensional differences between the geometries of the grooves and the cutting tool, and to protect the diamond cutting tool from wear, different numbers of cutting cycles were used to generate an individual groove. Figure 6.1(a) shows a schematic diagram of each groove that was machined in four cycles by a faceted diamond tool. The depth of the rough-cut in cycle 1 and 2 was over 10 μ m, whereas the depth

of finish cut in cycle 3 and 4 was $4\mu\text{m}$.

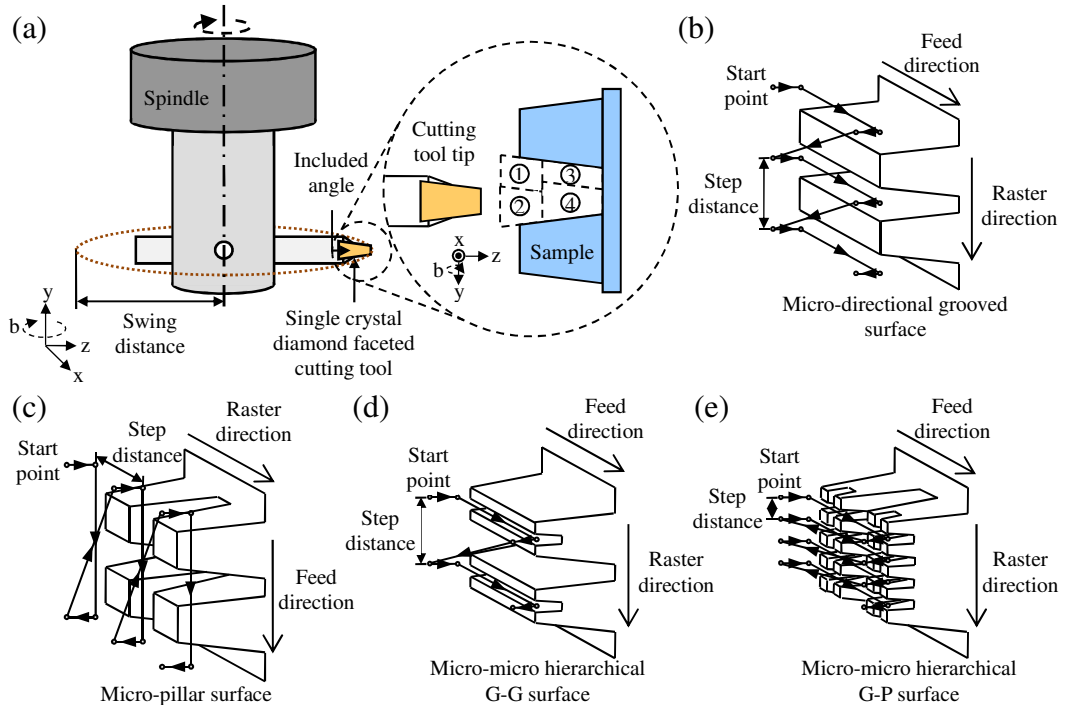


Figure 6.1 (a) Cutting geometry of UPRM, and the tool path design of surface generation in (b) micro-grooved surfaces, (c) micro-pillar surface, (d) micro-micro hierarchical G-G surface, (e) micro-micro hierarchical G-P surface by UPRM.

To fabricate the micro-grooved surfaces, the unidirectional retreat method was employed to generate grooves on the whole single-point diamond turned sample surface by the horizontal cutting strategy shown in Figure 6.1(b). After the generation of the whole micro-grooved surface on the sample, vertical cutting with a step distance of 0.05mm was then employed to mill the whole sample surface by moving the cutting tool up with a specific value on the z-axis.

For the generation of the micro-pillar surfaces, a horizontal cutting strategy using a unidirectional retreat method was employed to first generate grooves in

one direction as illustrated in Figure 6.1(b). After generation of the whole micro-grooved surface on the sample, the fixture was then rotated 90° along the z-axis, as shown in Figure 6.1(c). A horizontal cutting strategy using a unidirectional retreat method was employed to generate grooves perpendicular to the previous direction. The combination of the generated micro-grooves perpendicular to each direction forms a micro-pillar surface. Vertical cutting with a step distance of 0.05mm was then employed to mill the whole sample surface by moving the cutting tool up a specific amount along the z-axis.

Regarding the fabrication of the micro-micro hierarchical groove-groove (G-G) surface as shown in Figure 6.1(d), a horizontal cutting strategy using a unidirectional retreat method was employed to generate grooves at the top of the micro-grooved surface, after the generation of the micro-grooved surface, as shown in Figure 6.1(b).

With regard to the fabrication of the micro-micro hierarchical groove-pillar (G-P) surface shown in Figure 6.1(e), a horizontal cutting strategy using a unidirectional retreat method was employed to generate grooves at the top of the micro-micro hierarchical groove-groove (G-G) surface as shown in Figure 6.1(d), after the fixture was rotated 90° along the z-axis. It is known that cutting conditions and machine tool characteristics are major factors affecting the surface generation

in UPRM. Therefore, surface quality evaluation is necessary and it is discussed in the next section.

6.2.3 Surface Topography Measurement

To measure the geometrical parameters of the micro-patterned surfaces machined in the experiment, a white light interferometer (Zygo Nexview) was employed to capture the surface topographies. The system applied a non-contact method to measure surface roughness, step height and angle of slope with a vertical resolution in the nanometric range. Figure 6.2 shows the surface height maps and cross sectional view of the machined surfaces with 20x magnification. It is found that the deviation between the designed and the measured dimension of micro-grooved and pillar surfaces are within $\pm 2\mu\text{m}$, as listed in Table 6.2.

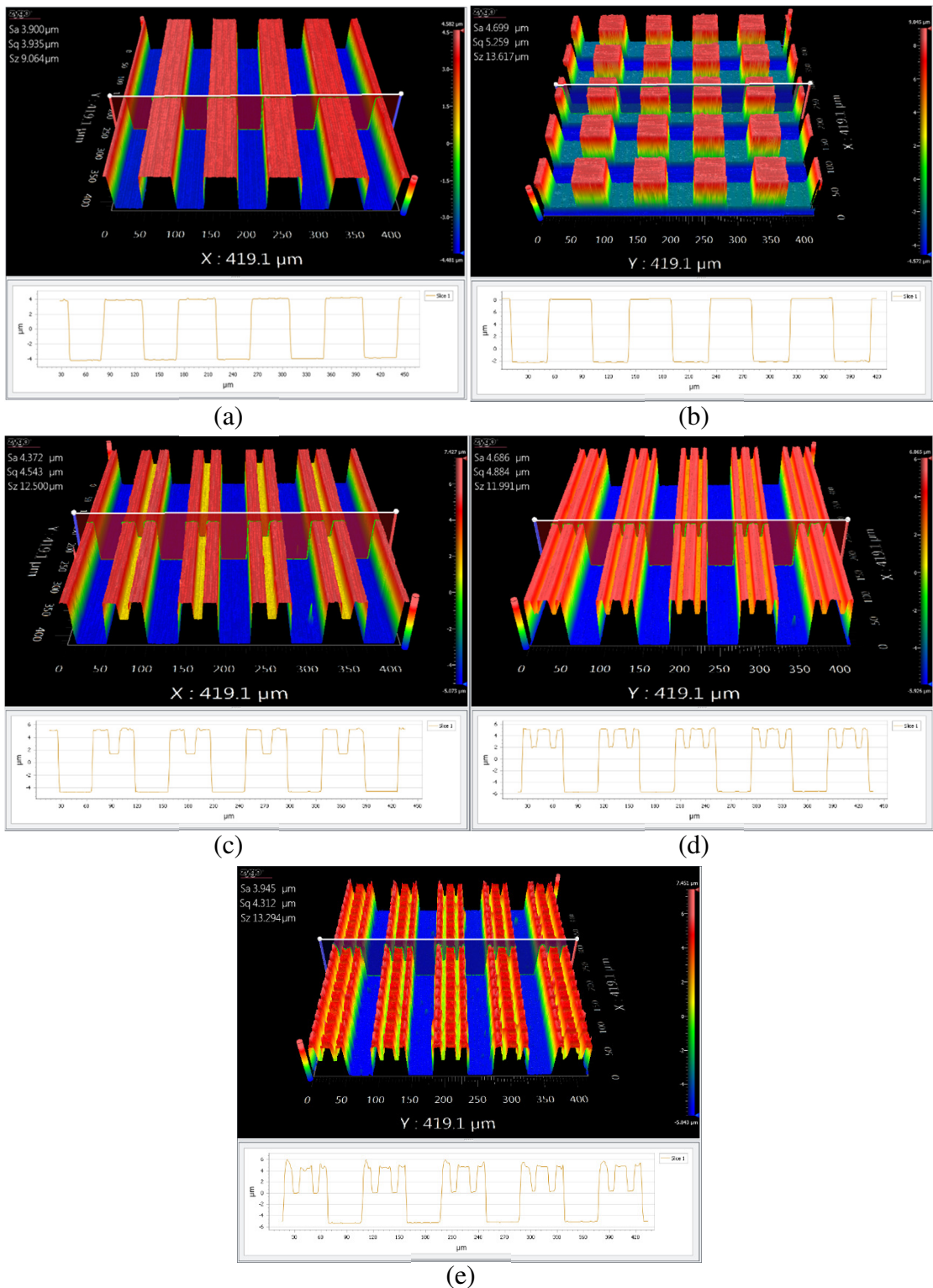


Figure 6.2 Surface topographies of (a) micro-grooves, (b) micro-pillars, (c) micro-micro hierarchical G-G structure I, (d) micro-micro hierarchical G-G structure II, and (e) micro-micro hierarchical G-P structures fabricated by UPRM. (Remarks: G-G = Groove-Groove, G-P = Groove-Pillar)

Table 6.2 Measured geometrical parameters of micro-patterned COC surfaces.

Surface structure	Lower			Upper			Measured angle, β (°)
	Depth, h (μm)	Width, w (μm)	Spacing, s (μm)	Depth, h' (μm)	Width, w' (μm)	Spacing, s' (μm)	
Micro-grooves	12.5	45.5	44.2	-	-	-	75.2
Micro-pillars	12.5	45.5	45.1	-	-	-	74.9
Micro-micro	9.9	44.2	45.1	4	15.2	15.2	75.1
hierarchical G-G structure I							
Micro-micro	10.8	45.5	45.1	3.4	10	7~12	75.1
hierarchical G-G structure II							
Micro-micro	10.0	44.7	45.5	4.4	10~12	7~10	74.3
hierarchical G-P structure							

6.2.4 Results and Discussion

In order to investigate the anisotropic wetting of micro-micro hierarchical surfaces fabricated by UPRM, the static contact angles of water droplets have been measured by the sessile drop method. The images of the water droplets on various sample surfaces captured by camera from the side view are presented in Figure 6.3. Each reported data point of the static contact angle is the average of six to eight independent measurements on a deionized water droplet of approximately 5 μl , as shown in Table 6.3.

After the generation of hierarchical micro-grooves on the spacing between the micro-directional grooved surface by UPRM, the static contact angle of the water droplet increased from 108.9° to 123.6° in the orthogonal direction on

micro-micro hierarchical G-G structure I, as shown in Figure 6.3(a) and 6.3(c). This reveals that the droplet freely advances on the micro-micro hierarchical ridges in the parallel direction, but is restricted by the periodic hierarchical ridges that induce an energy barrier in the orthogonal direction (Zhao and Law, 2012; Neuhaus et al., 2012). As a result, the average static contact angle of the water droplet further increases from 145.9° to 152.0° in the orthogonal direction.

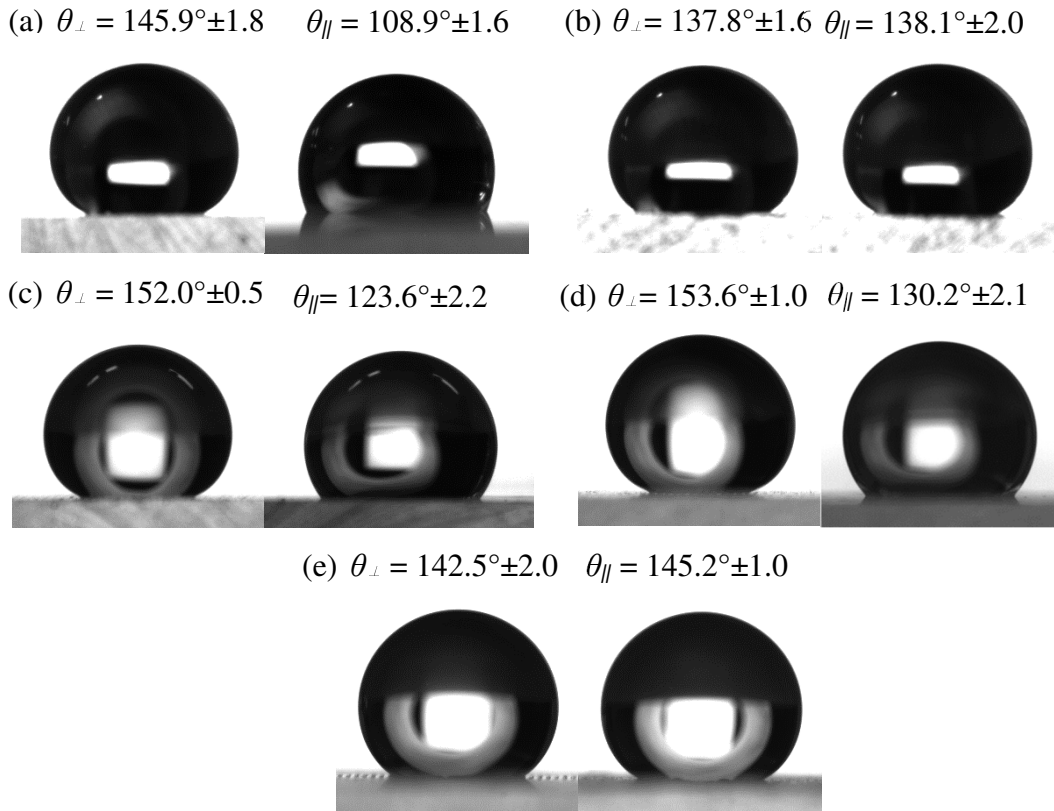


Figure 6.3 Static contact angles of $5\mu\text{l}$ water droplets on (a) micro-grooves, (b) micro-pillars, (c) micro-micro hierarchical G-G structure I, (d) micro-micro hierarchical G-G structure II, and (e) micro-micro hierarchical G-P structure.

Table 6.3 Wetting performance of the micro-patterned COC surfaces.

Surface structure	Static contact angle	Sliding angle, α	Roll-off angle, ζ
Flat	$88.6^\circ \pm 2.0$	Not slide	Stuck
Micro-grooves	$\theta_\perp = 145.9^\circ \pm 1.8$ $\theta_\parallel = 108.9^\circ \pm 1.6$	$\alpha_\parallel = 24^\circ$	$\zeta_\parallel = 29^\circ$
Micro-pillars	$\theta_\perp = 137.8^\circ \pm 1.6$ $\theta_\parallel = 138.1^\circ \pm 2.0$	Not slide	Stuck
Micro-micro hierarchical G-G structure I	$\theta_\perp = 152.0^\circ \pm 0.5$ $\theta_\parallel = 123.6^\circ \pm 2.2$	$\alpha_\parallel = 24^\circ$	$\zeta_\parallel = 28^\circ$
Micro-micro hierarchical G-G structure II	$\theta_\perp = 153.6^\circ \pm 1.0$ $\theta_\parallel = 130.2^\circ \pm 2.1$	$\alpha_\parallel = 24^\circ$	$\zeta_\parallel = 28^\circ$
Micro-micro hierarchical G-P structure	$\theta_\perp = 142.5^\circ \pm 2.0$ $\theta_\parallel = 145.4^\circ \pm 1.0$	Not slide	Stuck

Among the two samples of the micro-micro hierarchical G-G structures, structure II gives a higher static contact angle of 130.2° in the parallel direction than that of 123.6° on structure I, and similar static contact angles of 152.0° and 153.6° in the orthogonal direction, as shown in Figure 6.3(c) and 6.3(d). This reveals that the static contact angle further increases after adding more grooves in the top asperities of the micro-micro hierarchical structures. This is due to the contact area between the solid and liquid interface on structure II being less than that on structure I when both droplets are under the Cassie and Baxter state. According to the Cassie and Baxter model, the static contact angle increases when the area fraction of the projected wet area decreases. The relatively high values of

the static contact angles also imply that both droplets may stand at the top of the micro-micro hierarchical structures. It is believed that the micro-grooves at the top of the micro-micro hierarchical G-G structures are the dominant factor in the wetting process.

In respect to the micro-micro hierarchical G-P structure, the static contact angles in the parallel and orthogonal directions are similar (142.5° and 145.2°), as shown in Figure 6.3(e). This implies that the droplet may be under the Cassie and Baxter, the same as the droplet on the micro-pillars shown in Figure 6.3(b). When the droplet is under the Cassie and Baxter regime, it stands at the top of the micro-micro hierarchical G-P surface. Thus, the spreading of the droplet after deposition is restricted by the spacing between the micro-pillars in both the orthogonal and parallel directions. All of these results for similar and higher static contact angles (142.5° and 145.2°) are shown in Figure 6.3(e) when compared with those on the micro-pillars (137.8° and 138.1°).

When the static angle measured on the micro-micro hierarchical G-P structure is compared to that on the micro-micro hierarchical G-G structure II shown in Figure 6.3(d), the static contact angle decreases from 153.6° to 142.5° and increases from 130.2° to 145.2° in the orthogonal and parallel directions respectively. This reveals that the droplet is restricted by the periodic hierarchical

pillars on the micro-ridges that induce an energy barrier in both the orthogonal and parallel directions. It is believed that the micro-pillars at the top of the micro-micro hierarchical G-P structures are the dominant factor in the wetting process.

To investigate the droplet mobility on the sample surfaces, sliding angle measurements were undertaken on a micro-grooved surface, a micro-pillar surface, two micro-micro hierarchical G-G structures, and a micro-micro hierarchical G-P structure. The sliding behaviour of a water droplet on a sample surface is among the fundamental aspects of wettability (Lv et al., 2010; Miwa et al., 2000). The sliding angle is defined as the angle at which the droplet starts to move on the sample. During the sliding angle measurement, a 10 μ l water droplet was firstly deposited on the sample surface on a computer-controlled tilting stage in the horizontal position. The tilting angle was then increased until the droplet rolled off the surface. Figure 6.4 shows snapshots of the videos that recorded the sliding angle measurement of various sample surfaces.

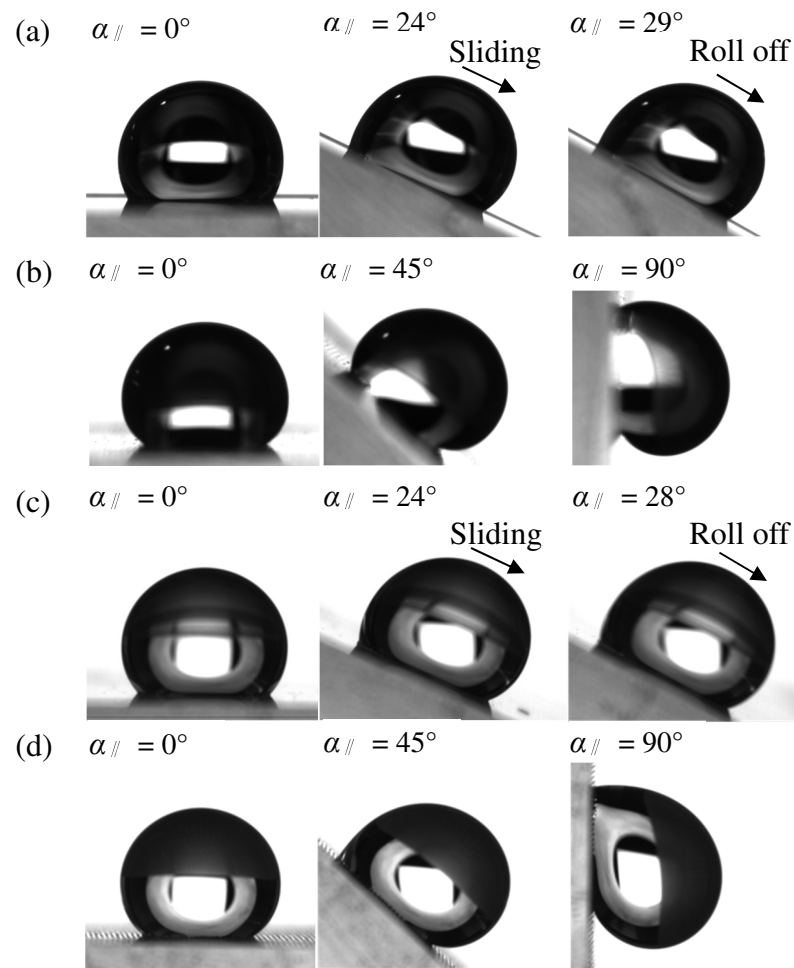


Figure 6.4 Sliding performance of water droplets on (a) micro-grooved surface, (b) micro-pillar surface, (c) micro-micro hierarchical G-G structure, and (d) micro-micro hierarchical G-P surface.

In the sliding angle measurement of the micro-micro hierarchical G-G structure, the 10 μ l water droplet started to slide at 24° and rolled-off at 28° in the parallel direction, as shown in Figure 6.4(c). Although the micro-micro hierarchical G-G structure gives a higher static contact angle than that of the micro-grooved surface, the sliding performance is nearly the same as that of the micro-grooved surface, as shown in Figure 6.4(a). The reason may be that the

water droplet in a composite wetting state on the micro-micro hierarchical G-G structure also experiences a continuous wetting and dewetting process which is related to the inertial mass of the droplet when sliding on the continuous hierarchical ridges or micro-ridges in the parallel direction.

Although the micro-micro hierarchical G-P structure gives a higher static contact angle than that of the micro-pillar surface, the water droplet on the micro-micro hierarchical G-P structure did not slide even at a 90° tilting angle, as shown in Figure 6.4(d). The sliding performance is the same as that of the micro-pillar surface shown in Figure 6.4(b). This can be explained by the sliding mechanism of a water droplet on micro-pillar surfaces. The explanation can also be applied to that on the micro-micro hierarchical G-P structure when the droplet is under a composite wetting state. The discontinuous advancement of the droplet caused by the spacing between the pillars induces an energy barrier which prevents the droplet sliding on the inclined micro-pillar surface, even at a 90° tilting angle. One of the edges of the hierarchical pillars may act as an opposing force on an inclined surface in the sliding direction of the water droplet. This can greatly increase the friction acting on the water droplet.

6.3 Irregular Micro-Micro Hierarchical Structures Fabricated by EFCS

This section discusses the wetting characteristics of irregular micro-micro hierarchical structures fabricated by the end-fly-cutting servo (EFCS) method and compares it with that of regular micro-micro hierarchical structures fabricated by UPRM in section 6.2.

6.3.1 Experimental Setup

Single-point diamond turning (SPDT) was employed at the beginning to cut sample surfaces at the same level using a Nanoform 200 machine for preparing flat sample surfaces. This avoids the occurrence of varying depths of micro-micro hierarchical structures on a large area of the sample surface due to the incorrect level of different samples in machining the hierarchical structures. After the preparation, a Moore Nanotech 350FG 4-axes CNC SPDT machine was used to generate the irregular hierarchical structured surfaces on the sample surfaces which were attached by a specially designed fixture. During the machining process, a single crystal diamond faceted cutting tool, with 30° included angle and $14.0\mu\text{m}$ width of tool tip was selected and fixed to the spindle with a certain swing distance (Cheng et al., 2016). All the cutting conditions of EFCS, including spindle speed,

depth of cut, swing distance, feed rate, step distance, and cutting environment are given in Table 4.1. The workpiece material used in this study was cyclic olefin copolymer (Topas COC, 5013SL-01), copolymerized from norbornene and ethylene with a metallocene catalyst. All the 20mm x 20mm COC sheets used in the experiment were prepared by plastic injection molding from the raw material.

6.3.2 Fabrication of Irregular Micro-Micro Hierarchical Structures

After the consideration of feed rate, depth of cut, and spindle speed, EFCS, as shown in Figure 6.5(a), was used to fabricate an irregular micro-micro hierarchical G-G surface and an irregular micro-micro hierarchical G-P surface. During the cutting process of the irregular micro-micro hierarchical G-G surface, a vertical cutting mode, as shown in Figure 6.5(c), was used to generate the hierarchical structures after the fabrication of the micro-grooved surfaces at the PB position shown in Figure 6.5(b).

Regarding the fabrication of the irregular micro-micro hierarchical G-P surface, a horizontal cutting mode was applied to generate the hierarchical pillars at the PD position, as shown in Figure 6.5(b), after fabrication of the irregular micro-micro hierarchical G-G surface.

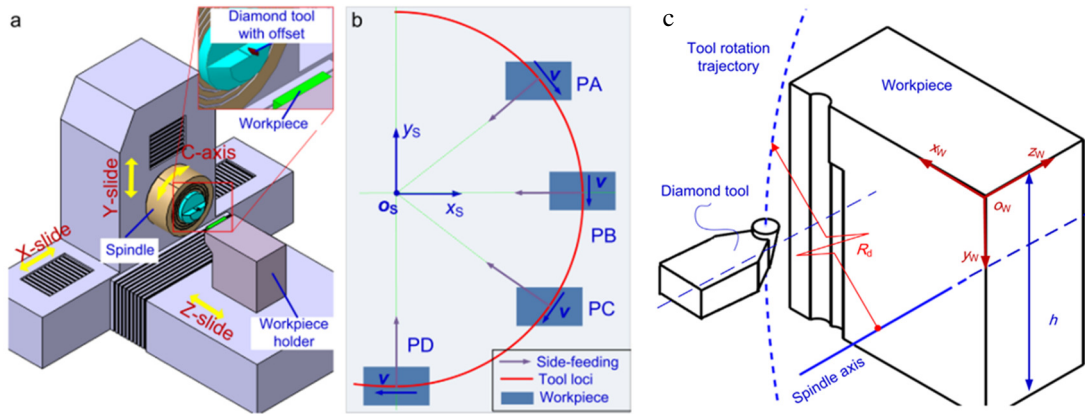


Figure 6.5 Configuration of (a) the EFCS system, (b) the cutting model, and (c) the vertical cutting mode (Zhu et al., 2015).

6.3.3 Surface Topography Measurement

To measure the geometrical parameters of the irregular micro-patterned surfaces machined from the experiment, a white light interferometer (Zygo Nexview) was employed to capture the surface topographies. Figure 6.6 shows the surface height maps and cross sectional view of the machined surfaces with 20x magnification. Some irregular micro-grooves and micro-pillars were found at the top of the micro-micro hierarchical G-G surface and the micro-micro hierarchical G-P surface of approximate sizes $10\mu\text{m}$ groove depth, $45\mu\text{m}$ groove widths and spacing.

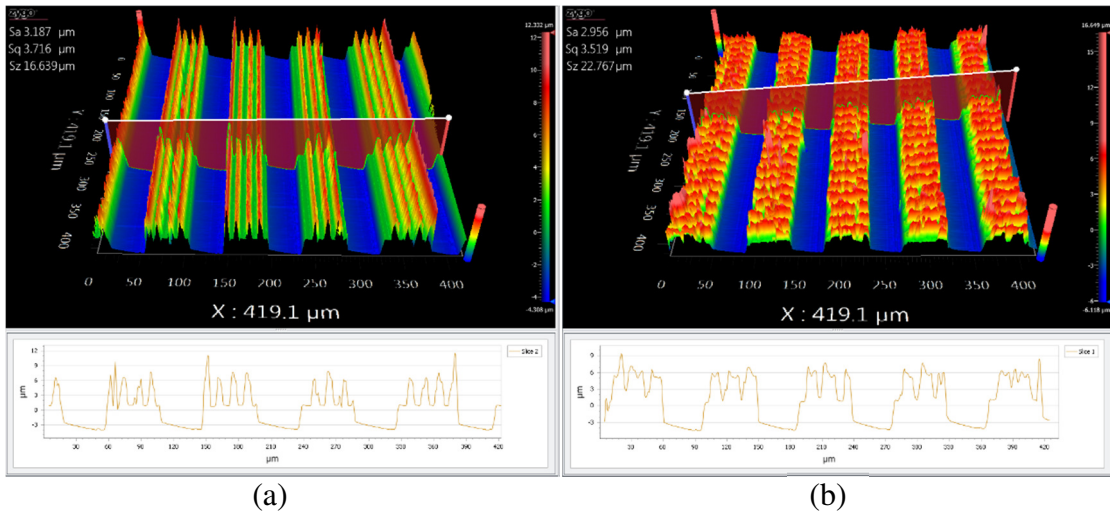


Fig. 6.6 Surface topographies of irregular (a) micro-micro hierarchical G-G surface, and (b) micro-micro hierarchical G-P surface fabricated by end-fly-cutting-servo diamond machining.

6.3.4 Results and Discussion

In order to investigate the difference in anisotropic wetting between the regular and irregular micro-micro hierarchical surfaces, the static contact angles of the water droplets were measured by the sessile drop method. The images of water droplets on two sample surfaces captured by camera from the side view are presented in Figure 6.7. Each reported data point of the static contact angle is the average of six to eight independent measurements on a deionized water droplet of approximately 5 μl .

The experimental data shows that the average static contact angles on the irregular micro-micro hierarchical G-G surface are 151.1° and 106.9° in the orthogonal and parallel directions respectively, as shown in Figure 6.7(a). This

reveals that the droplet freely advances on the ridges in the parallel direction, but is restricted by the periodic ridges that induce an energy barrier in the orthogonal direction (Zhao and Law, 2012; Neuhaus et al., 2012). Compared to the irregular micro-micro hierarchical G-G surface, the average static contact angles measured on the irregular micro-micro hierarchical G-P surface increase from 106.9° to 137.6° in the parallel direction as shown in Figure 6.7(b). These findings imply that the droplets are under the Cassie and Baxter state. This can be explained by the hierarchical pillars on irregular micro-micro hierarchical G-P surface successfully inducing an energy barrier to the spreading of the droplet after its deposition in both the orthogonal and parallel directions. This results in the increases of the average static contact angles in the two directions.

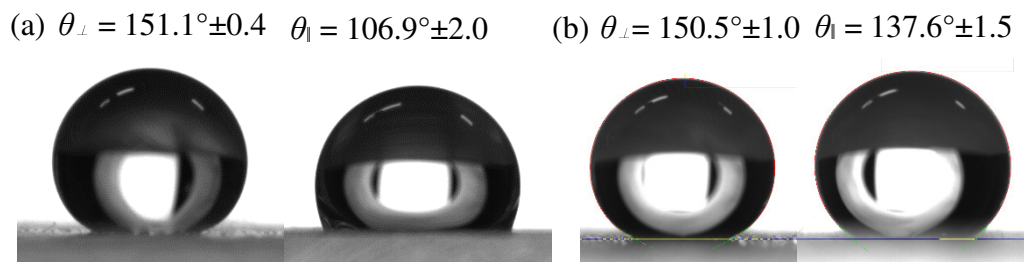


Figure 6.7 Static contact angles of $5\mu\text{l}$ water droplets on irregular (a) micro-micro hierarchical G-G surface, and (b) micro-micro hierarchical G-P surface.

Figure 6.8 shows the images of the wetting process and the contact area of the solid-air-liquid interface of a water droplet with regular micro-micro hierarchical G-G structures, and irregular micro-micro hierarchical G-G structures.

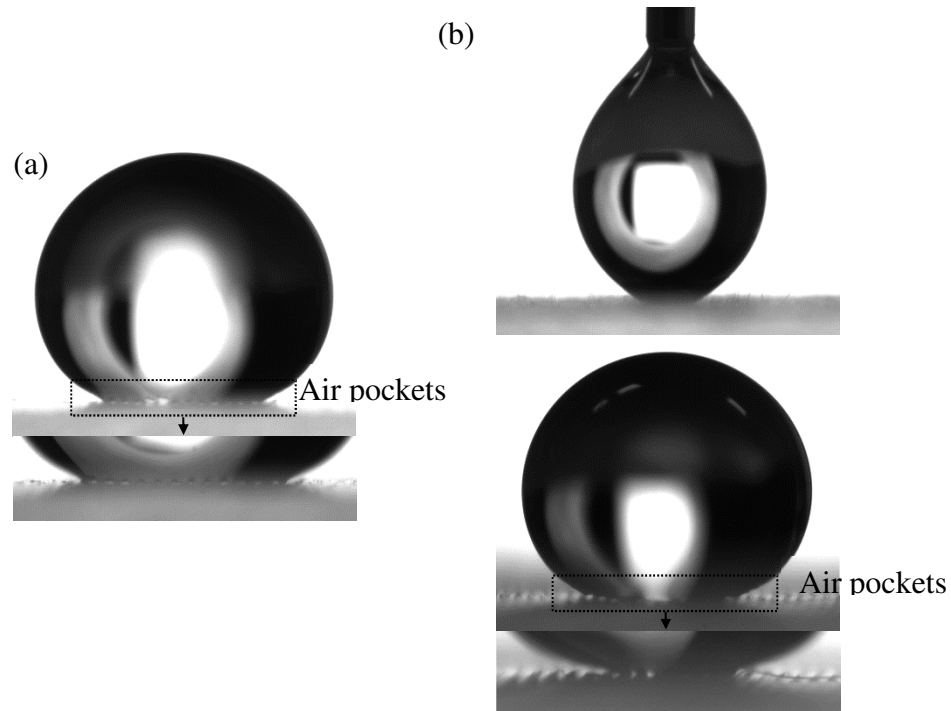


Figure 6.8 The wetting process and the contact area of solid-air-liquid interface of a water droplet with (a) regular micro-micro hierarchical G-G structure, and (b) irregular micro-micro hierarchical G-G structure.

It was found that the contact area of the solid-air-liquid interface of a water droplet with irregular micro-micro hierarchical G-G structures is less than that with regular hierarchical G-G structures. This can be explained by the top asperities of the upper grooves being relatively flat on regular micro-micro hierarchical G-G structures, as shown in Figure 6.2(c) and 6.2(d). The relatively flat area induces large support for the landing and wetting of the water droplet. On the other hand, the sharp upper structures shown in Figure 6.6(a) on the irregular micro-micro hierarchical G-G structures do not provide enough support to the landing of the water droplet, thus inducing a higher energy barrier during the

wetting process.

In the sliding angle measurement on the irregular micro-micro hierarchical G-G structure, a 10 μ l water droplet started to slide at 44° and rolled-off at 45° in the parallel direction, as shown in Figure 6.9(a). Compared with the irregular micro-micro hierarchical G-P structure, the water droplet did not slide even at a 90° tilting angle, as shown in Figure 6.9 (b). This reveals that the water droplet under the Cassie and Baxter regime still forms a solid-liquid-air interface with the irregular micro-micro hierarchical G-G structure due to the sharp edge of the ridges during the tilting process, as shown in Figure 6.6(a).

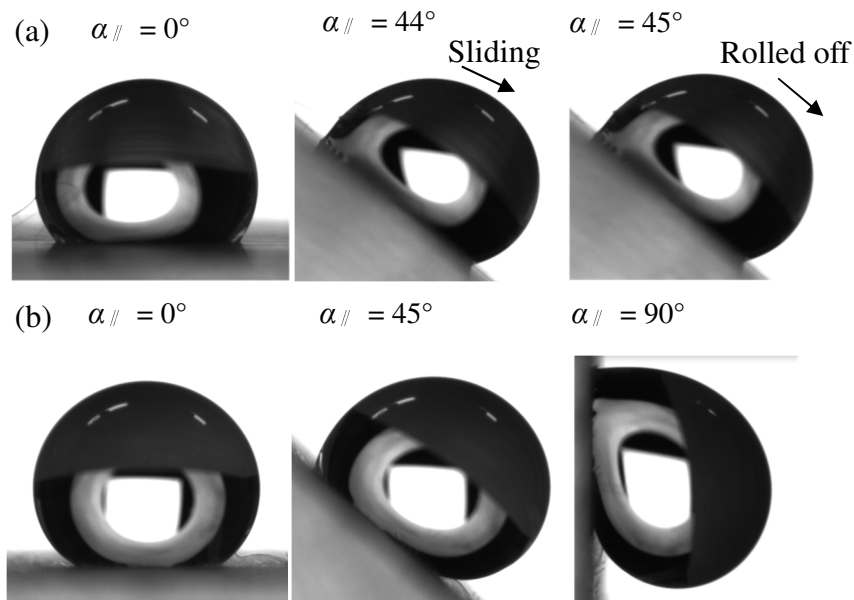


Figure 6.9 Sliding performance of water droplets on irregular (a) micro-micro hierarchical G-G surface, and (b) micro-micro hierarchical G-P surface.

The sliding mechanism of a water droplet on irregular micro-micro

hierarchical G-G structures is completely different from that on irregular micro-micro hierarchical G-P structures. A water droplet on the hierarchical G-P structures experiences a discrete wetting and dewetting process at the advancing and receding contact lines respectively, due to the spacing between the pillars. On the other hand, a water droplet on the hierarchical G-G structures experiences a continuous wetting and dewetting process which is related to the inertial mass of the droplet when sliding on the continuous ridges in the parallel direction. Thus, the discontinuous advancement of the droplet caused by the spacing between the upper pillars induces an energy barrier prevents in the droplet sliding on the inclined hierarchical G-P structures, even at a 90° tilting angle, whereas the water droplet on the hierarchical G-G structure slides at an angle of 44° in the parallel direction due to the free advancement of the droplet on the continuous ridges.

6.4 Multi-level Hierarchical Structures Fabricated by EFC

Motivated by the wetting performance of the irregular micro-micro hierarchical G-G structures, micro-micro hierarchical G-G structures with single and double patterns, as shown in Figure 6.10, are designed accordingly in order to investigate the influence of multi-level structures on the wetting performance of hierarchical G-G structures fabricated by end-fly-cutting (EFC).

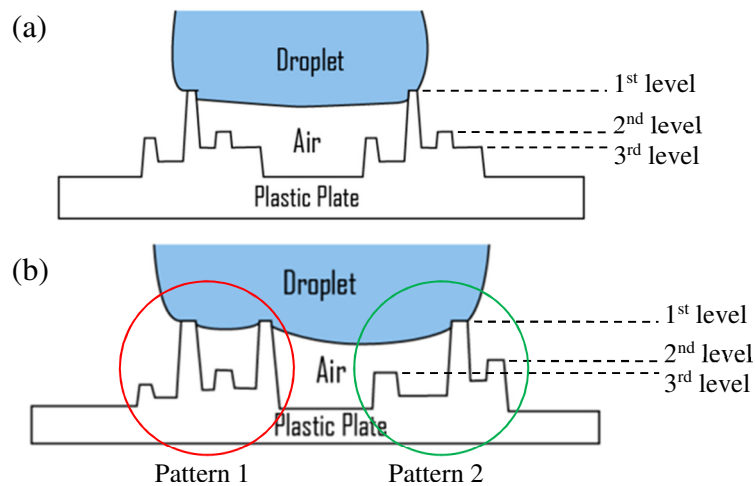


Figure 6.10 Schematic diagrams of the multi-level design of (a) hierarchical G-G structure III with one pattern, and (b) hierarchical G-G structure IV with two patterns.

6.4.1 Experimental Setup

Single-point diamond turning (SPDT) was employed at the beginning to cut sample surfaces at the same level using a Nanoform 200 machine for preparing flat sample surfaces. This avoids the occurrence of varying depths of micro-micro hierarchical structures on a large area of the sample surface in machining the hierarchical structures. After the preparation, a Moore Nanotech 350FG 4-axes CNC SPDT machine was used to generate the micro-micro hierarchical structured surfaces with multi-level design, as shown in Figure 6.10. During the machining process, a single crystal diamond faceted cutting tool with 30° included angle and $12.0\mu\text{m}$ width of tool tip was selected and fixed to the spindle allowing a certain swing distance (Cheng et al., 2016). All the cutting conditions of EFCS, including

spindle speed, depth of cut, swing distance, feed rate, step distance, and cutting environment are given in Table 4.1. The workpiece material for this study was cyclic olefin copolymer (Topas COC, 5013SL-01) copolymerized from norbornene and ethylene with a metallocene catalyst. All the 20mm x 20mm COC sheets used in the experiment were prepared by plastic injection molding from the raw material.

6.4.2 Fabrication of Multi-level Hierarchical Structures

Differing from the end-fly-cutting servo method, the workpiece and the fixture were placed on the spindle of a Moore Nanotech 350FG machine during the EFC process. A diamond cutting tool was mounted on a stationary tool holder for EFC. After consideration of the cutting efficiency and surface quality, the unidirectional retreat method was employed to generate two micro-micro hierarchical G-G structures by movement of the spindle in the Y slide, as shown in Figure 6.5. The main difference between two micro-micro hierarchical G-G structures is that micro-micro hierarchical G-G structure III only consists of one pattern on the whole surface, but micro-micro hierarchical G-G structure IV consists of two patterns on the whole surface.

6.4.3 Surface Topography Measurement

To measure the geometrical parameters of micro-micro hierarchical G-G structures with multi-level design in the experiment, a white light interferometer (Zygo Nexview) was employed to capture the surface topographies. Figure 6.11 shows the surface height maps and cross sectional view of the machined surfaces with 20x magnification. It was found that multi-level hierarchical G-G structure III with a single pattern and micro-micro hierarchical G-G structure IV with double patterns, having approximately 10 μm groove depths, 45 μm groove widths and spacing were successfully fabricated.

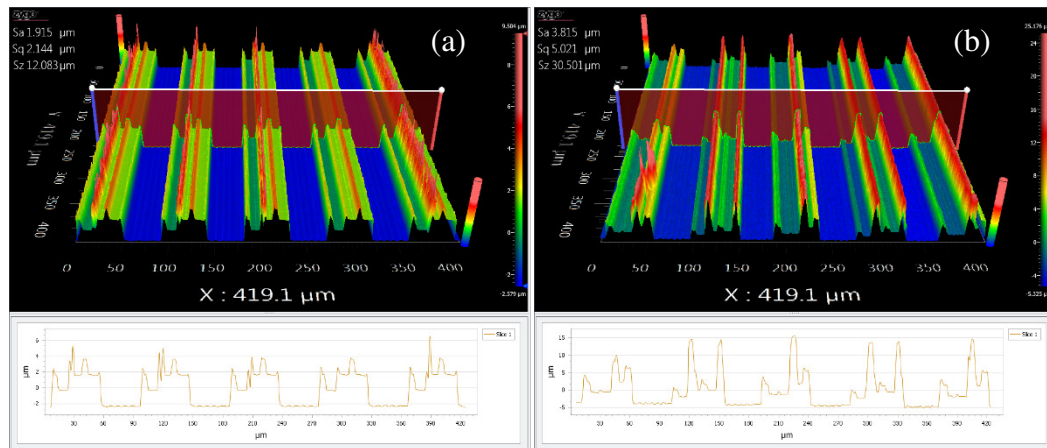


Figure 6.11 Surface topographies of the multi-level design of (a) hierarchical G-G structure III with one pattern, and (b) hierarchical G-G structure IV with two patterns fabricated by ultra-precision vertical cutting.

6.4.4 Results and Discussion

The static contact angles of the water droplets on two micro-micro

hierarchical G-G structures were measured by the sessile drop method. Images of the water droplets on various sample surfaces were captured by camera from the side view, and are presented in Figure 6.12. Each reported data point of the static contact angle is the average of six to eight independent measurements by a deionized water droplet of approximately volume 5 μ l.

Compared to the irregular micro-micro hierarchical G-G surface, the average static contact angles on micro-micro hierarchical G-G structure III with a single pattern increases from 146.4° to 151.5°, and from 106.9° to 122.5° in the orthogonal and parallel directions respectively, as shown in Figure 6.7(a) and 6.12(a). This implies that the multi-level design successfully enhances the static contact angle of micro-micro hierarchical G-G structures. This is because the different height levels of the surface geometry of the hierarchical structures can reduce the contact area of the solid-liquid interface, reserving more buffers for air pocket formation, as shown in Figure 6.13(a). Figure 6.12(c) shows that the contact area between the water droplet and the structures are very small during the air pocket formation.

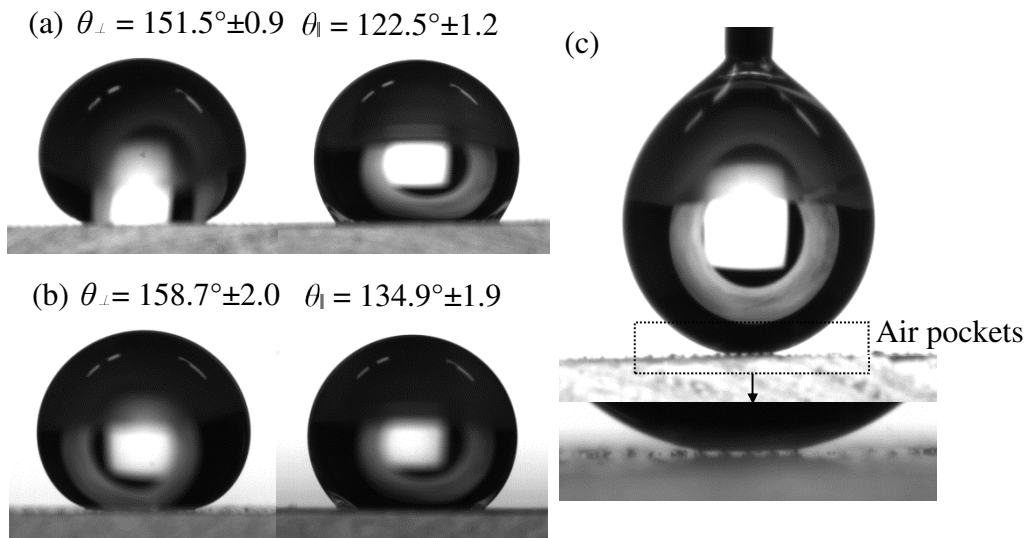


Figure 6.12 Static contact angles of 5 μ l water droplets on the multi-level (a) hierarchical G-G structure III with one pattern, and (b) hierarchical G-G structure IV with two patterns, and (c) the air pockets formation between the water droplet and the structures.

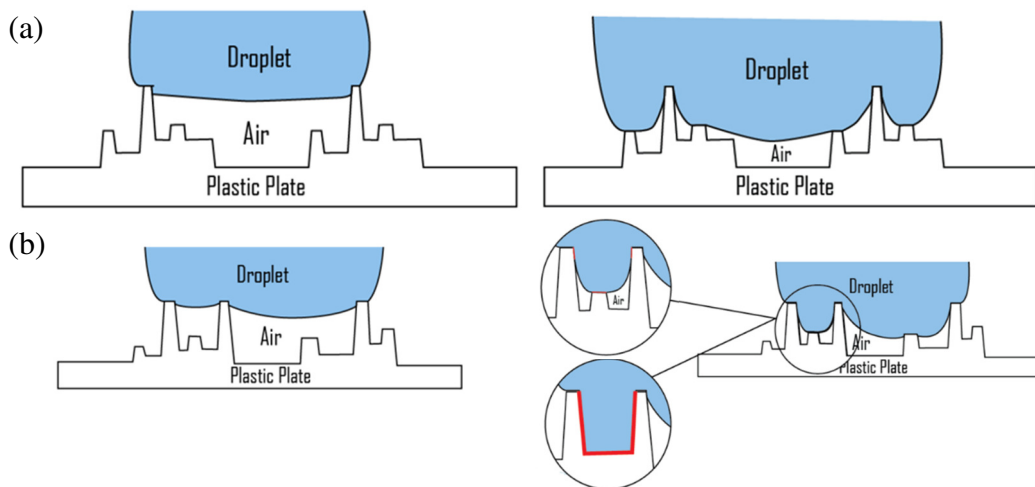


Figure 6.13 Wetting models on the multi-level of (a) hierarchical G-G structure III with one pattern, and (b) hierarchical G-G structure IV with two patterns.

In respect to the micro-micro hierarchical G-G structure IV with two patterns, the average static contact angles further increase to 158.7° and 134.9° in the orthogonal and parallel directions respectively, as shown in Figure 6.12(b) when

compared to the micro-micro hierarchical G-G structure III with a single pattern. This implies that the double pattern design further enhance the static contact angle of the water droplet when compared with the single pattern design. This can be explained by the larger variation of the height levels of the hierarchical structures further reducing the contact area of the solid-liquid interface, so as to reserve more buffers to the air pocket formation, as shown in Figure 6.13(b). Applying the multi-level design of the hierarchical G-G structure with double patterns, the water static contact angle can even reach 161.5° , which is the highest contact angle measured in the whole study, as shown in Figure 6.14.

In order to identify the wetting states of the two micro-micro hierarchical G-G structures with multi-level design, the droplet contact line were observed by an optical microscope from the top view, as shown in Figure 6.15. It can be seen that the water droplets are at the top of the two hierarchical G-G structures. This may be due to the sharp edges induced by the machining process in the vertical cutting of the hierarchical structures, which help stabilize deposition of the water droplets. In other words, the sharp edges make the droplet sit at the top of the hierarchical structures. This provides evidence that the droplet is governed by the Cassie and Baxter regime, and forms a solid-liquid-air interface with the hierarchical structures. More importantly, this is one of the essential requirements to achieve

hydrophobic self-cleaning surfaces.

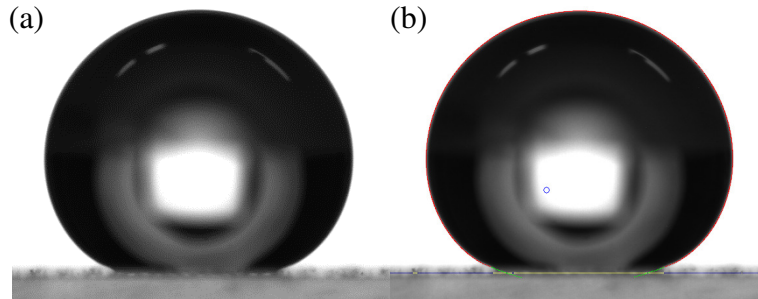


Figure 6.14 (a) Original image of a water droplet captured from the highest static contact angle of 161.5° on a multi-level hierarchical G-G structure IV with two patterns, and (b) the image of the water droplet after contour fitting by software.

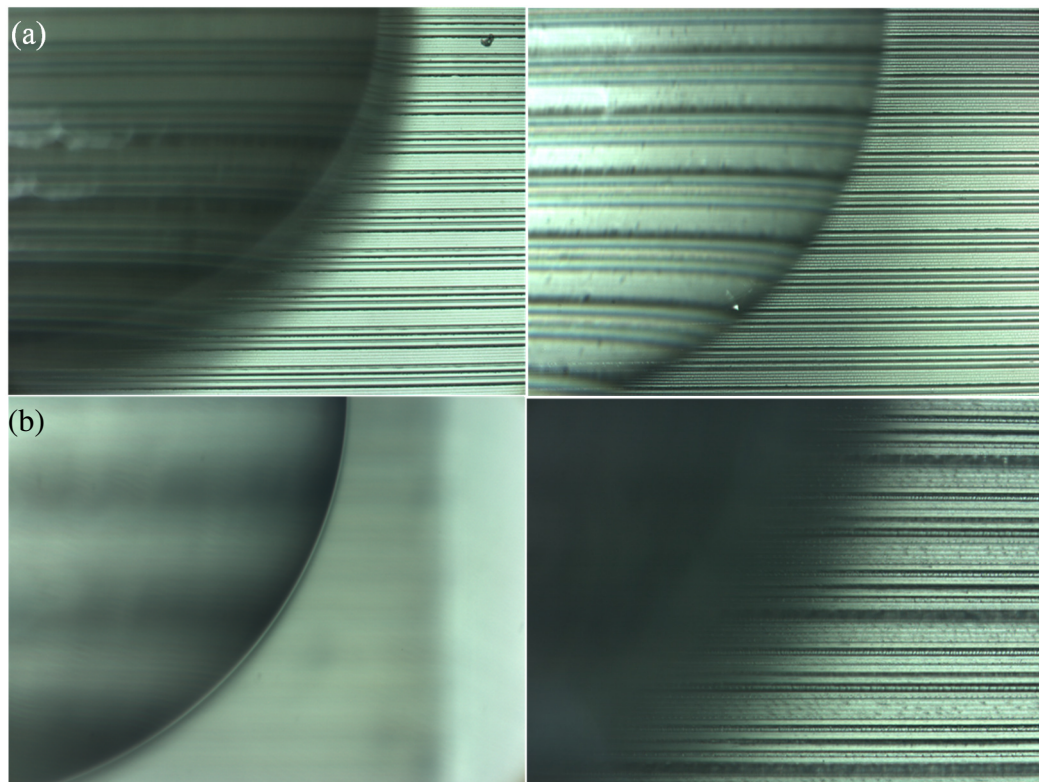


Figure 6.15 Droplet contact lines on (a) micro-micro hierarchical G-G structure III, and (b) micro-micro hierarchical G-G structure IV. (Remark: Left is focusing on the droplet contact line; Right is focusing on the structures.)

In the sliding angle measurement of the multi-level hierarchical G-G structure

III with a single pattern, a 10 μ l water droplet started to slide at 47° and rolled-off at 74° in the parallel direction, as shown in Figure 6.16(a). The reason may be that the aspect ratio of the hierarchical structures on micro-micro hierarchical G-G structure III is not high enough, due to fabrication defects. This low aspect ratio of the hierarchical structures decreases the stability of the droplet wetting state. Thus, the droplet wetting state on multi-level hierarchical G-G structure III with a single pattern may have transited from the Cassie and Baxter regime to the intermediate wetting state during the tilting process.

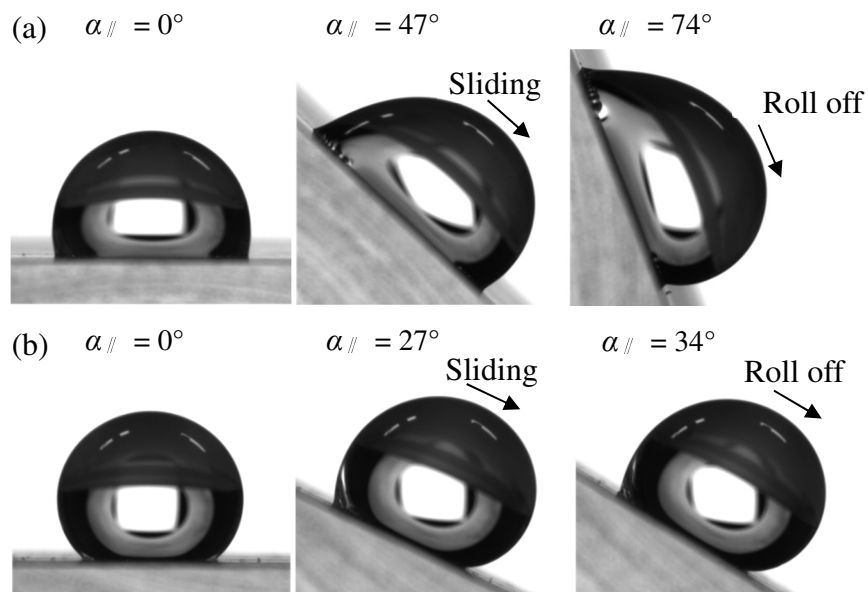


Figure 6.16 Sliding performance of water droplets on the multi-level (a) hierarchical G-G structure III with one pattern, and (b) hierarchical G-G structure IV with two patterns.

Compared with multi-level hierarchical G-G structure IV with two patterns, the droplet started to slide at 27° and rolled-off at 34° in the parallel direction, as

shown in Figure 6.16(b). This is likely due to the relatively higher aspect ratio of the hierarchical structures on the micro-micro hierarchical G-G structure IV, as shown in Figure 6.11(b), that increases the stability of the droplet wetting state. Thus, the water droplet under the Cassie and Baxter regime still forms a solid-liquid-air interface with the micro-directional grooved surface due to the larger variation of the height level of the hierarchical structures shown in Figure 6.16(b) during the tilting process. More importantly, all of these show that the multi-level design with a single pattern can enhance the static contact angle, whereas the multi-level design with two patterns can increase the stability of the droplet wetting state during the tilting process.

6.5 Summary

This chapter describes the anisotropic wetting of bare micro-micro hierarchical structured surfaces including (i) regular micro-micro hierarchical structures, (ii) irregular micro-micro hierarchical structures, and (iii) multi-level hierarchical structures fabricated by highly controllable one-step mechanical machining methods, including ultra-precision raster milling (UPRM), end-fly-cutting servo (EFCS), and end-fly-cutting (EFC), which are potentially applicable for mass production in plastic injection molding. Due to the sharp edges induced

by the numerical-controlled tool path of the material removal process in the mechanical machining, the dimensions of the surface geometry of the micro-patterned surfaces can be defined relatively accurately. By studying the static contact angle, the interaction between the droplet contact line and micro-patterned surfaces, it is found that the static contact angle of a water droplet can be enhanced to over 150° after adding hierarchical structures on the micro-grooved surfaces. The contact area of the solid-air-liquid interface can be reduced by using irregular micro-micro hierarchical G-G structures fabricated by EFCS, when compared with regular micro-micro hierarchical G-G structures fabricated by UPRM. This is because the irregular hierarchical structures do not provide enough support to the landing of the water droplet and induce a higher energy barrier during the wetting process. In addition, applying the multi-level design of a hierarchical G-G structure with two patterns can further enhance the water static contact angle to 161.5° , since the larger variation of the height levels of the hierarchical structures can reduce the contact area of the solid-liquid interface, thereby reserving more buffers to the air pocket formation when compared with the regular and irregular micro-micro hierarchical G-G structures. The experimental results from the sliding angle measurements show that regular micro-micro hierarchical G-G structure, irregular micro-micro hierarchical G-G surface, and the multi-level hierarchical

G-G structure with two patterns give good sliding performance. This is important for potential applications in microfluidic systems, such as artificial self-cleaning surfaces for mass production in plastic injection molding.

Chapter 7

Conclusions and Suggestions for Future Work

7.1 Overall Conclusions

Microstructures in nature, such as lotus leaves and butterfly wings, have micro-patterned surfaces that possess hydrophobic properties. These hydrophobic surfaces have enormous potential in applications on artificial self-cleaning surfaces, such as the next generation of vehicle windshields, exterior paint for buildings and solar panels, due to their extreme water repellence. Recent studies have focused on the fabrication of hydrophobic micro-patterned surfaces using a variety of methods. Most of the present manufacturing processes are complicated in chemical treatment, time-consuming, not suitable for fabricating large surfaces, do not consider the optical performance, or are only applicable to engineering materials such as metals, semiconductors and alloys, but are limited in regard to plastics. There are very few one-step manufacturing methods capable of fabricating bare hydrophobic micro-patterned surfaces with good sliding performance and optical performance that are suitable for mass production.

It has also become clear that the existence of air under a droplet governed by the Cassie and Baxter state on a hydrophobic micro-patterned surface is an

essential element in achieving self-cleaning properties. However, traditionally, verification of the droplet wetting state was only capable of identifying complete and composite wetting states but could not identify intermediate wetting states. These limitations in the characterization of the droplet wetting state further lead to an incomplete understanding of the influence of the intermediate wetting states on the sliding performance of a water droplet on micro-directional grooved surfaces.

Highly controllable fabrication methods for bare micro-patterned surfaces with good sliding and optical performance for mass production are proposed using ultra-precision machining. Some major findings and conclusions can be summarized as follows:

- (i) Optimization modeling of the surface geometry of biomimetic structures for self-cleaning has been proposed based on an optical function and a wetting model for fabricating micro-patterned surfaces by ultra-precision machining, including micro-grooves and micro-pillars, considering hydrophobicity and optical performance. It is found that a composite wetting state can be achieved when the dimensions of the surface geometry are within a critical range. In addition, the transparency of the micro-patterns can be controlled using ultra-precision raster milling. Structural parameters for self-cleaning properties have been identified and provide an important guide for the

development of advanced self-cleaning surfaces.

- (ii) The wetting characteristics of bare hydrophobic micro-patterned cyclic olefin copolymer surfaces machined by a one-step fabrication method, ultra-precision raster milling (UPRM), which is potentially applicable for mass production in plastic injection molding, have been studied. Due to the sharp edges induced by the numerical-controlled tool path in the material removal process in the mechanical machining, the area fraction of the projected wet area on the micro-patterned surfaces can be defined accurately in the Cassie and Baxter model. This results in the excellent agreement of the static contact angle predicted by the models with the measured static contact angle of water droplets from the experiment.
- (iii) By studying the droplet anisotropy, and the interaction between the droplet contact line and the micro-patterned surfaces, it is found that the water droplet governed by the Cassie and Baxter regime is stabilized by the sharp edges at the top asperities of the micro-grooves and micro-pillars after deposition on the sample surfaces.
- (iv) The experimental results from the contact angle hysteresis and sliding angle measurements show that the micro-directional grooved surface gives good sliding performance which is important for the potential applications in

microfluidic systems, such as artificial self-cleaning surfaces for mass production in plastic injection molding.

- (v) A characterization method for the droplet wetting state, significantly affecting its sliding performance on hydrophobic surfaces, has been proposed from observations of the droplet contact lines on micro-directional grooved surfaces fabricated by UPRM. This characterization method is capable of identifying intermediate wetting states, including partial wetting and droplets contacting the side walls of the grooves, from the Cassie and Baxter state all of which have solid-liquid-air interfaces, however it is difficult to use traditional verification methods for identification.
- (vi) The droplet anisotropy, the variation of the static contact angle against droplet deposition time, and comparison with the static contact angle predicted from the Wenzel and the Cassie and Baxter models have been studied. The various wetting states characterized by the droplet contact lines, including partial wetting, droplet contact with the side walls of the grooves, complete wetting, and the Cassie and Baxter regime, have been verified.
- (vii) The experimental results from anisotropic sliding measurement show that the partial wetting state represents the sliding boundary of micro-grooved surfaces, whereas droplets contacting the side walls of the grooves are still

in a favorable wetting state for anisotropic sliding on micro-directional grooved surfaces. This finding will enable more flexibility in the design of advanced self-cleaning surfaces.

- (viii) The groove width and spacing of micro-grooved surfaces are identified as key factors, resulting in different sliding angles and durations before roll-off from surfaces with the same area fraction of projected wet area (50%) in the parallel direction to the anisotropic sliding measurement.
- (ix) Bare micro-micro hierarchical structured surfaces with good sliding performance have been successfully fabricated by a one-step fabrication method, ultra-precision raster milling (UPRM). It is found that the static contact angle of a water droplet can be enhanced to over 150° after adding hierarchical structures on the micro-grooved surfaces.
- (x) The contact area of the solid-air-liquid interface can be reduced by using irregular micro-micro hierarchical G-G structures fabricated by EFCS when compared with regular micro-micro hierarchical G-G structures fabricated by UPRM. This is because irregular hierarchical structures do not provide enough support to the landing of the water droplet, and induce a higher energy barrier during the wetting process.
- (xi) Applying the multi-level design of a hierarchical G-G structure with two

patterns can further enhance the water static contact angle to 161.5° , since the larger variation of the height levels of the hierarchical structures can reduce the contact area of the solid-liquid interface, thereby reserving more buffers to the air pocket formation when compared with the regular and irregular micro-micro hierarchical G-G structures.

This research enables highly controllable one-step fabrication methods for bare micro-patterned surfaces with good sliding and optical performance, which are important for potential applications in microfluidic systems, such as artificial self-cleaning surfaces for mass production in plastic injection molding. The established optimization model is able to estimate equilibrium performance between hydrophobicity and optical performance for facilitating the development of advanced self-cleaning surfaces. Applying the developed characterization method for the droplet wetting state contributes to deeper insights into the influence of intermediate wetting states to the sliding performance on micro-patterned surfaces, and provides more flexibility for the design of advanced self-cleaning surfaces.

7.2 Suggestions for Future Work

Although this thesis provides a comprehensive study of the wetting characteristics of biomimetic structures for self-cleaning fabricated by ultra-precision machining and the characterization of droplet wetting states on micro-patterned surfaces, and all the research objectives have been achieved, there are still some related research areas that could be undertaken in the near future.

Suggestions for further work are as follows:

- (i) Study of the wetting characteristics and optical performance of micro-patterned surfaces manufactured by injection molding for mass production

In the present study, highly controllable one-step fabrication methods of bare micro-patterned surfaces with good sliding and optical performance are only proposed using ultra-precision machining technologies which are able to manufacture mould inserts for injection molding of the self-cleaning surfaces.

Although ultra-precision machining methods can directly fabricate micro-patterned surfaces on materials, it would be valuable to study the wetting characteristics and optical performance of micro-patterned surfaces with self-cleaning properties manufactured by injection molding for mass production.

- (ii) A model-based simulation system for illustrating the rolling and sliding behavior of liquid on micro-patterned surfaces

To have a better understanding and further develop self-cleaning surfaces, it is necessary to study the fluid mechanics of the rolling and sliding behavior of liquids on micro-patterned surfaces. Such study will help to construct a complete theoretical model of the rolling and sliding behavior of a liquid on a micro-patterned surface. This model will be able to define the boundary of the rolling and sliding behavior of liquid in regard to self-cleaning properties.

- (iii) Investigation of the feasibility of adding more optical functions onto the developed optimization model for advanced self-cleaning surfaces

The optimization model is currently only able to estimate the equilibrium performance between the hydrophobicity and transparency of micro-patterns for advanced self-cleaning surfaces. By controlling different cutting parameters, micro-patterns with various surface geometries for advanced self-cleaning surfaces can be manufactured using ultra-precision machining.

More optical functions such as haze and anti-reflection can be considered to add into the developed optimization model for advanced self-cleaning surfaces. The modified model will facilitate the development of multi-functionally advanced self-cleaning surfaces with great potential for wider applications in our lives.

Appendices

Appendix I Precitech Freeform 705G Ultra-precision Raster Milling Machine

Precitech Freeform 705G, as shown in Figure I-1, is a 5-axes CNC ultra-precision machining system which is able to conduct three-dimensional asymmetric freeform milling and grinding in X, Y, Z axes, and in two rotational axes in B and C axes. It is able to be directly mill micro-structures and freeform optical elements such as F-theta lenses and V-grooves with form accuracy in sub-micrometre range, and surface roughness in nanometre range. In addition, it consists of an optional grinding system for grinding optical products made from non-ferrous materials such as ceramic and steels.



Figure I-1 Precitech Freeform 705G Ultra-precision raster milling machine.

The key features and kinematics information of the UPRM machine are summarized as follows:

- Sealed natural granite base protects the machine from contamination.
- Self-leveling dual chamber isolation system minimizes the influence of vibration on the cutting process.
- Linear motor driven and the hydrostatic oil bearing slideways with advanced stiffness characteristics contribute to the ultimate performance during the cutting process.
- 8.6 or 1.4nm feedback resolution is for the improved velocity control.
- Slot-type thrust bearing spindle design is available up to 5000 rpm.
- Qnx[®] real time OS is designed for the advanced programming capacity with 1.0nm programming resolution for increased throughput.
- Rotational axes in operation and grinding spindles are available for the advanced capabilities.
- Maximum feed rate can reach 1500mm/min.
- Slide Travel is 350mm, 150mm, and 250mm in X, Y, and Z respectively.

Appendix II Hitachi TM3000 Scanning Electron Microscope

Hitachi TM3000, as shown in Figure II-1, is a tabletop scanning electron microscope which can directly capture 2D images of non-conductive specimens or samples containing moisture with over a range of magnification from 15x to 30,000x in 30nm resolution. This wide magnification range ensures maximum benefit from the depth-of-field and resolution advantages of the electron microscopy. The image capture pixel count is 640 x 480 pixels using “Quick Save” mode, and 1,280 x 960 pixels using “Save” mode.



Figure II-1 TM3000 Hitachi Electron Microscope.

TM3000 features a backscattered electron detector with four independent segments. Different combinations of the independent segments enable the user to emphasize compositional or topographic details in the image by using

different modes including “Compo”, “Topo”, “Shadow 1”, and “Shadow 2”. Coating of the specimen is not required for the TM3000 when using charge-up reduction mode with accelerating voltage of 5 or 15kV by a tungsten source. This allows the user capture a clear image on insulating materials. Versatile detector control and multiple beam conditions also improve the image quality.

Appendix III Zygo Nexview™ 3D Optical Surface Profiler

Zygo Nexview™, as shown in Figure III-1, is a 3D optical surface profiler which is able to measure different kinds of surfaces from super-smooth to very rough with a sub-nanometer range of precision using a non-contact measurement method. Different types of measurement including flatness, roughness, thin film, large steps and segments, and steep slopes can be captured with feature heights ranging from less than 1nm up to 20000µm.



Figure III-1 Zygo Nexview™ 3D Optical Surface Profiler.

The main features of Zygo Nexview™ are shown as follows:

- All types of surface including flatness, roughness, thin film, large steps and segments, and steep slopes can be captured from super-smooth to very rough.
- Its exceptional precision and repeatability in performance is highly suitable for the most demanding production applications.
- The vibration tolerance technology gives a robust operation in virtually any environment.
- Its surface measurement parameters fit the international standard of ISO 25178.
- The new graphical workflow software design provides more capability and less training to the users.
- Streamlined design of the measurement system gives full automation and no manual in controls to the users.

Appendix IV Alicona IFM G4 3D Optical Surface Profiler

Alicona IFM G4, as shown in Figure IV-1, is a non-contact type three dimensional optical surface profiler which is based on the principle of focus-variation to capture the surface topography in micro- and nano ranges. Both the captured information of topography and color can be registered in true color. It is able to measure various complex features in geometries such as cutting edge radii, cutting angle, and steep flanks. Different modes including “Profile Analysis”, “Area Analysis”, “Form Analysis”, “Volume Analysis”, and “2D Image Analysis” can be selected to perform measurement based on the different requirements in measurement. A polarizer is available for the topography measurement of highly reflective samples.



Figure IV-1 Alicona IFM G4 3D Optical Surface Profiler.

The main features of Alicona IFM G4 are summarized as follows:

- Up to 10mm in vertical resolution.
- Up to 2.5 mm per second in vertical measurement speeds
- Fast measurement due to the automation of measurement tasks via scripting
- Capable to measure the roughness and form accuracy of the sample surfaces.

Appendix V Olympus BX40 Optical Microscope

The Olympus BX40 optical microscope, as shown in Figure V-1, consists of objective lenses in 5x, 10x, 20x, 50x, and 100x magnification. The optical microscope objective lens can be synchronized with a computer to capture real time 2D images. The main function of the optical microscope in this study is to observe the droplet contact lines on the sample surfaces from the top view.

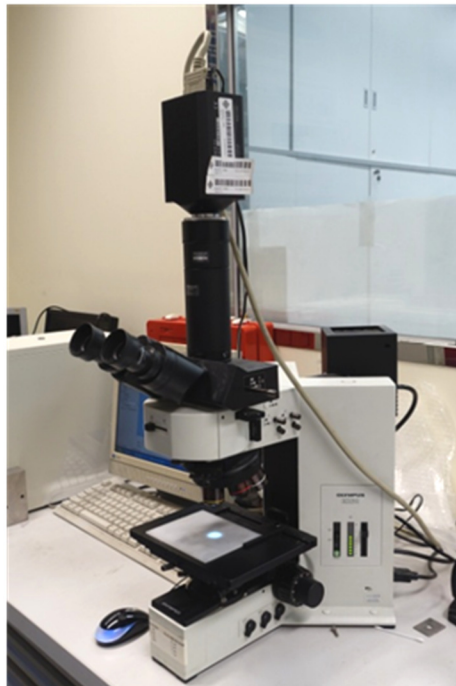


Figure V-1 Olympus BX40 Optical Microscope.

Appendix VI Sindatek Model 100SB Video-based Optical Contact Angle Meter

Sindatek Model 100SB, as shown in Figure VI-1, is an video-based optical goniometer which is able to measure static and dynamic contact angles of droplets on sample surfaces using sessile, captive, and pendant drop methods. It is generally used to analyze the wetting behaviour on solid surfaces, the surface free energy of solids, and the interfacial tension from the drop shape. The contact angle goniometer consists of three main units which are camera, water pump, and sample stages. The size of the water droplet can be controlled by the water pump automatically using the software named “Magic Droplet”. A homogeneous LED back lighting electronics is used as a continuously adjustable intensity for imaging.



Figure VI-1 Sindatek Model 100SB Video-based Optical Contact Angle Meter.

The main features of the contact angle goniometer are summarized as follows:

- The camera is high resolution 1280 x 1024 USB 2.0 with 60 fps speed.
- The sample stage is a standard size in 90mm x 90mm which can be adjusted in X, Y, and Z directions.
- The maximum sample size is 18cm x 9cm (W x H).
- The range of contact angle measured is from 0 to $180^\circ \pm 0.1^\circ$.
- The range of surface and interfacial tension is 0.01 ~ 2,000 mN/m ± 0.05 mN/m.
- Automatic baseline detection can be selected.
- Video can be recorded with a rate of 15fps under a time setting for dynamic study such as spreading, absorption, and reaction kinetics.

References

- Agarwal S.; Rao, P. V. “Experimental investigation of surface/subsurface damage formation and material removal mechanisms in SiC grinding”, *International Journal of Machine Tools and Manufacture* **2008**, *48*, 698–710.
- Ahmed, F.; Choudhury, N. R.; Dutta, N. K.; Zannettino, A.; Knott., R. “Near Superhydrophobic Fibrous Scaffold for Endothelialization: Fabrication, Characterization and Cellular Activities”, *Biomacromolecules* **2013**, *14*, 3850-3860.
- Bartolo, D.; Bouamrène, F.; Verneuil, E.; Buguin, A.; Silberzan, P.; Moulinet, S. “Bouncing or sticky droplets: Impalement transitions on superhydrophobic micropatterned surfaces”, *Europhysics Letters* **2006**, *74*, 299.
- Bhushan, B.; Jung, Y. C. “Natural and Biomimetic Artificial Surfaces for Superhydrophobicity, Self-Cleaning, Low Adhesion, and Drag Reduction”, *Progress in Materials Science* **2011**, *56*, *1*, 1-108.
- Bhushan, B.; Jung, Y. C.; Koch, K. “Micro-, Nano- and Hierarchical Structures for Superhydrophobicity, Self-cleaning and Low Adhesion”, *Philosophical Transactions of the Royal Society A-Mathematical Physical and Engineering Sciences* **2009**, *367*, *1894*, 1631-1672.
- Bixler, G. D.; Bhushan, B. “Bioinspired micro/nanostructured surfaces for oil

- drag reduction in closed channel flow”, *Soft Matter* **2013**, 9, 1620-1635.
- Bixler, G. D.; Bhushan, B. “Bioinspired rice leaf and butterfly wing surface structures combining shark skin and lotus effects”, *Soft Matter* **2012**, 8, 11271-11284.
- Bletek, T.; Klocke, F.; Hüntten, M.; Dambon, O. “Dressing of fine grained diamond grinding wheels for ultra precision grinding of structured molds in brittle hard materials”, *Optifab 2013* **2013**, 888405–888408.
- Boreyko, J. B.; Baker, C. H.; Poley, C. R.; Chen, C. H. Wetting and Dewetting Transitions on Hierarchical Superhydrophobic Surfaces, *Langmuir* **2011**, 27, 7502-7509.
- Bormashenko, E. “Progress in understanding wetting transitions on rough surfaces”, *Advances in Colloid and Interface Science* **2015**, 222, 92-103.
- Bormashenko, E.; Pogreb, R.; Whyman, G.; Erlich, M. “Cassie–Wenzel Wetting Transition in Vibrating Drops Deposited on Rough Surfaces: Is the Dynamic Cassie–Wenzel Wetting Transition a 2D or 1D Affair?”, *Langmuir* **2007**, 23, 6501-6503.
- Byun, D.; Hong, J.; Saputra; Ko, J. H.; Lee, Y. J.; Park, H. C.; Byun, B. K.; Lukes, J. R. “Wetting Characteristics of Insect Wing Surfaces”, *Journal of Bionic Engineering* **2009**, 6, 63-70.

- Cassie, B. D.; Baxter, S. “Wettability of Porous Surfaces”, *Trans. Faraday Soc.* **1944**, *40*, 546-551.
- Celia, E.; Darmanin, T.; de Givenchy, E. T.; Amigoni, S.; Guittard, F. “Recent Advances in Designing Superhydrophobic Surfaces”, *Journal of Colloid and Interface Science* **2013**, *402*, 1-18.
- Chen, F.; Zhang, D.; Yang, Q.; Yong, J.; Du, G.; Si, J.; Yun, F.; Hou, X. “Bioinspired Wetting Surface via Laser Microfabrication”, *ACS Applied Materials & Interfaces* **2013**, *5*, *15*, 6777-6792.
- Chen, F.; Zhang, D. S.; Yang, Q.; Wang, X. H.; Dai, B. J.; Li, X. M.; Hao, X. Q.; Ding, Y. C.; Si, J. H. Hou, X. “Anisotropic Wetting on Microstrips Surface Fabricated by Femtosecond Laser”, *Langmuir* **2011**, *27*, *1*, 359-365.
- Chen, Y.; He, B.; Lee, J. H. “Anisotropy in the Wetting of Rough Surfaces”, *Journal of Colloid and Interface Science* **2005**, *281*, 458-464.
- Cheng, C. T.; Zhang, G.; To, S. “Wetting characteristics of bare micro-patterned cyclic olefin copolymer surfaces fabricated by ultra-precision raster milling”, *RSC Advances* **2016**, *6*, 1562-1570.
- Cheng, M. N.; Cheung, C. F.; Lee, W. B.; To, S.; Kong, L. B. “Theoretical and experimental analysis of nano-surface generation in ultra-precision raster

- milling”, *International Journal of Machine Tools and Manufacture* **2008**, *48*, 1090-1102.
- Cheng, Y. T.; Rodak, D. E.; Wong, C. A.; Hayden, C. A. “Effects of Micro- and Nano-structures on the Self-cleaning Behaviour of Lotus Leaves”, *Nanotechnology* **2006**, *17*, 1359-1362.
- Chu, D. H.; Nemoto, A.; Ito, H. “Enhancement of dynamic wetting properties by direct fabrication on robust micro–micro hierarchical polymer surfaces”, *Applied Surface Science* **2014**, *300*, 117-123.
- Davaasuren, G.; Ngo, C. V.; Oh, H. S.; Chun, D. M. “Geometric study of transparent superhydrophobic surfaces of molded and grid patterned polydimethylsiloxane (PDMS)”, *Applied Surface Science* **2014**, *314*, 530-536.
- David, R.; Neumann, A. W. “Shapes of drops in the Cassie state on grooved surfaces”, *Colloids and Surfaces A: Physicochemical and Engineering Aspects* **2012**, *399*, 41-45.
- Ebert, D.; Bhushan, B. “Durable Lotus-effect surfaces with hierarchical structure using micro- and nanosized hydrophobic silica particles”, *Journal of Colloid and Interface Science* **2012**, *368*, 584-591.

- Erbil, H. Y. “The debate on the dependence of apparent contact angles on drop contact area or three-phase contact line: A review”, *Surface Science Reports* **2014**, *69*, 325-365.
- Erbil, H. Y.; Cansoy, C. E. “Range of Applicability of the Wenzel and Cassie-Baxter Equations for Superhydrophobic Surfaces”, *Langmuir* **2009**, *25*, *24*, 14135-14145.
- Feng, J. S.; Tuominen, M. T.; Rothstein, J. P. “Hierarchical Superhydrophobic Surfaces Fabricated by Dual-Scale Electron-Beam-Lithography with Well-Ordered Secondary Nanostructures”, *Advanced Functional Materials* **2011**, *21*, 3715-3722.
- Feng, L.; Zhang, Y. A.; Xi, J. M.; Zhu, Y.; Wang, N.; Xia, F.; Jiang, L. “Petal effect: A superhydrophobic state with high adhesive force”, *Langmuir* **2008**, *24*, 4114-4119.
- Furmidge, C. G. L. “Studies at Phase Interfaces. I. The Sliding of Liquid Drops on Solid Surfaces and a Theory for Spray Retention”, *Journal of Colloid Science* **1962**, *17*, 309-324.
- Gao, L.; McCarthy, T. J. “Wetting 101 degree”, *Langmuir* **2009**, *25*, 14105-14115.

- Gao L.; McCarthy, T. J. “How Wenzel and Cassie Were Wrong”, *Langmuir* **2007**, *23*, 3762-3765.
- Gao L.; McCarthy, T. J. “The “Lotus Effect” Explained: Two Reasons Why Two Length Scales of Topography Are Important”, *Langmuir* **2006**, *22*, 2966-2967.
- Greiner, C.; Arzt, E.; del Campo, A. “Hierarchical Gecko-Like Adhesives”, *Advanced Materials* **2009**, *21*, 479-482.
- Gu, Z. Z.; Uetsuka, H.; Takahashi, K.; Nakajima, R.; Onishi, H.; Fujishima, A.; Sato, O. “Structural Color and the Lotus Effect”, *Angewandte Chemie-International Edition* **2003**, *42*, 894-897.
- Guo, P.; Lu Y.; Ehmman, K.F.; Cao, J. “Generation of hierarchical microstructures for anisotropic wetting by elliptical vibration cutting”, *CIRP Ann.-Manuf.Technol.* **2014**, *63*, 553–556.
- Guo, Z.; Liu, W. “Biomimic from the superhydrophobic plant leaves in nature: Binary structure and unitary structure”, *Plant Science* **2007**, *172*, 1103-1112.
- Han, D. W.; Steckl, A. J. “Superhydrophobic and Oleophobic Fibers by Coaxial Electrospinning”, *Langmuir* **2009**, *25*, 9454-9462.
- He, B.; Patankar, N.A.; Lee, J. “Multiple equilibrium droplet shapes and design criterion for rough hydrophobic surfaces”, *Langmuir* **2003**, *19*, 5001.

- Huovinen, E.; Hirvi, J.; Suvanto, M.; Pakkanen, T. A. “Micro–Micro Hierarchy Replacing Micro–Nano Hierarchy: A Precisely Controlled Way To Produce Wear-Resistant Superhydrophobic Polymer Surfaces”, *Langmuir* **2012**, *28*, 14747-14755.
- Jansen, H. P.; Nliznyuk, O.; Kooij, E. S.; Poelsema, B. “Simulating Anisotropic Droplet Shapes on Chemically Striped Patterned Surfaces”, *Langmuir* **2012**, *28*, *1*, 499-505.
- Jansen, H. P.; Zandvliet, H. J. W.; Kooij, E. S. “Evaporation of elongated droplets on chemically stripe-patterned surfaces”, *International Journal of Heat and Mass Transfer* **2015**, *82*, 537-544.
- Jena, R. K.; Yue, C. Y. “Cyclic Olefin Copolymer based Microfluidic Devices for Biochip Applications: Ultraviolet Surface Grafting using 2-methacryloyloxyethyl Phosphorylcholine”, *Biomicrofluidics* **2012**, *6*, *1*, 012822.
- Jeong, H. E.; Kwak, M. K.; Park, C. I.; Suh, K. Y. “Wettability of nanoengineered dual-roughness surfaces fabricated by UV-assisted capillary force lithography”, *Journal of Colloid and Interface Science* **2009**, *339*, 202-207.
- Jiang, Y.; Hirvi, J. T.; Suvanto, M.; Pakkanen, T. A. “Molecular dynamic simulations of anisotropic wetting and embedding on functionalized

- polypropylene surfaces”, *Chemical Physics* **2014**, *429*, 44-50.
- Jiang, Y. D.; Shu, L. M.; Natsu, W.; He, F. B. “Anisotropic wetting characteristics versus roughness on machined surfaces of hydrophilic and hydrophobic materials”, *Applied Surface Science* **2015**, *331*, 41-49.
- Jung, Y. C.; Bhushan, B. “Dynamic Effects Induced Transition of Droplets on Biomimetic Superhydrophobic Surfaces”, *Langmuir* **2009**, *25*, 9208-9218.
- Jung, Y. C.; Bhushan, B. “Wetting Transition of Water Droplets on Superhydrophobic Patterned Surfaces”, *Scripta Materialia* **2007**, *57*, 1057-1060.
- Jung, Y. C.; Bhushan, B. “Contact angle, adhesion, and friction properties of micro- and nanopatterned polymers for superhydrophobicity”, *Nanotechnology* **2006**, *17*, 4970-4980.
- Jung, Y. C.; Bhushan, B.; Koch, K. “Micro-, Nano- and Hierarchical Structures for Superhydrophobicity, Self-cleaning and Low Adhesion”, *Philosophical Transactions of the Royal Society A-Mathematical Physical and Engineering Sciences* **2009**, *367*, 1894, 1631-1672.
- Kang, S.M.; Lee, C.; Kim, H. N.; Lee, B. J.; Lee, J. E.; Kwak, M. K.; Suh, K. Y. “Directional Oil Sliding Surfaces with Hierarchical Anisotropic Groove Microstructures”, *Advanced Materials* **2013**, *25*, 5756-5761.

- Kim, D. H.; Kim, Y.; Kang, J. W.; Hong, S.; Lee, D.; Cho, C. R.; Kim, S. H.; Lee, D. W.; Kim, J. M. “Inclined-wall regular micro-pillar-arrayed surfaces covered entirely with an alumina nanowire forest and their improved superhydrophobicity”, *Journal of Micromechanics and Microengineering* **2011**, *21*, 075024.
- Kong, L. B.; Cheung, C. F.; To, S. “Design, fabrication and characterization of three dimensional patterned microstructured surfaces with self-cleaning properties from hydrophilic materials”, *Proceedings of the Institution of Mechanical Engineers Part B- Journal of Engineering Manufacture* **2012**, *226*, 1536-1549.
- Kong, L. B.; Cheung, C. F.; To, S.; Cheng, C. T. “Modeling and characterization of generation of 3D micro-structured surfaces with self-cleaning and optical functions”, *Optik* **2013**, *124*, 2848-2853.
- Kooij, E. S.; Jansen, H. P.; Bliznyuk, O.; Poelsema, B.; Zandvliet, H. J. W. “Directional wetting on chemically patterned substrates”, *Colloids and Surfaces A: Physicochemical and Engineering Aspects* **2012**, *413*, 328-333.
- Lee, S. G.; Lim, H. S.; Lee, D. Y.; Kwak, D.; Cho, K. “Tunable Anisotropic Wettability of Rice Leaf-Like Wavy Surfaces”, *Advanced Functional Materials* **2013**, *23*, 5, 547-553.

- Lee, W.; Jin, M. K.; Yoo, W. C.; Lee, J. K. “Nanostructuring of a Polymeric Substrate with Well-Defined Nanometer-Scale Topography and Tailored Surface Wettability” *Langmuir* **2004**, *20*, 7665-7669.
- Levkin, P. A.; Svec, F.; Frechet, J. M. J. “Porous Polymer Coatings: a Versatile Approach to Superhydrophobic Surfaces”, *Advanced Functional Materials* **2009**, *19*, 1993-1998.
- Li, B. J.; Zhou, M.; Zhang, W.; Amoako, G.; Gao, C. Y. “Comparison of structures and hydrophobicity of femtosecond and nanosecond laser-etched surfaces on silicon”, *Applied Surface Science* **2012**, *263*, 45-49.
- Li, J. A.; Liu, X. H.; Ye, Y. P.; Zhou, H. D.; Chen, J. M. “Fabrication of Superhydrophobic CuO Surfaces with Tunable Water Adhesion”, *Journal of Physical Chemistry C* **2011**, *115*, 4726-4729.
- Li, P.; Xie, J.; Deng, Z. J. “Characterization of irregularly micro-structured surfaces related to their wetting properties”, *Applied Surface Science* **2015**, *335*, 29-38.
- Li, P.; Xie, J.; Cheng, J.; Wu, K. K. “Anisotropic wetting properties on a precision-ground micro-v-grooved Si surface related to their micro-characterized variables”, *Journal of Micromechanics and Microengineering* **2014**, *24*,

075004.

Li, W.; Amirfazli, A. “Microtextured superhydrophobic surfaces: A thermodynamic analysis”, *Advances in Colloid Interface Science* **2007**, *132*, 51-68.

Li, X. Y.; Ma, X. H.; Lan, Z. “Dynamic Behavior of the Water Droplet Impact on a Textured Hydrophobic/Superhydrophobic Surface: The Effect of the Remaining Liquid Film Arising on the Pillars Tops on the Contact Time”, *Langmuir* **2010**, *26*, 7, 4831-4838.

Liu, Y.; Yin, X. M.; Zhang, J. J.; Wang, Y. M.; Han, Z. W.; Ren, L. Q. “Biomimetic hydrophobic surface fabricated by chemical etching method from hierarchically structured magnesium alloy substrate”, *Applied Surfaces Science* **2013**, *280*, 845-849.

Li, Y. Y.; Dai, S. X.; John, J.; Carter, K. R. “Superhydrophobic Surfaces from Hierarchically Structured Wrinkled Polymers”, *ACS Applied Materials & Interfaces* **2013**, *5*, 11066-11073.

Liu, S. H.; Liu, X. J.; Latthe, S. S. ; Gao, L.; An, S.; Yoon, S. S.; Liu, B. S.; Xing, R. M. “Self-cleaning transparent superhydrophobic coatings through

- simple sol-gel processing of fluoroalkylsilane”, *Applied Surface Science* **2015**, *351*, 897-903.
- Luo, C.; Xiang, M. M.; Liu, X. C.; Wang, H. “Transition from Cassie-Baxter to Wenzel States on microline-formed PDMS surfaces induced by evaporation or pressing of water droplets”, *Microfluid Nanofluid* **2011**, *10*, 831-842.
- Lv, C. J.; Yang, C. W.; Hao, P. F.; He, F.; Zheng, Q. S. “Sliding of Water Droplets on Microstructured Hydrophobic Surfaces”, *Langmuir* **2010**, *26*, *11*, 8704-8708.
- Ma, C. H.; Bai, S. X.; Peng, X. D.; Meng, Y. G. “Anisotropic wettability of laser micro-grooved SiC surfaces”, *Applied Surface Science* **2013**, *284*, 930-935.
- Ma, M. L.; Hill, R. M. “Superhydrophobic surfaces”, *Current Opinion in Colloid & Interface Science* **2006**, *11*, *4*, 193-202.
- Ma, M. L.; Hill, R. M.; Lowery, J. L.; Fridrikh, S. V.; Rutledge, G. C. “Electrospun poly(styrene-block-dimethylsiloxane) block copolymer fibers exhibiting superhydrophobicity”, *Langmuir* **2005**, *21*, 5549-5554.
- Malm, J.; Sahramo, E.; Karppinen, M.; Ras, R. H. A. “Photo-Controlled Wettability Switching by Conformal Coating of Nanoscale Topographies with Ultrathin Oxide Films”, *Chemistry of Materials* **2010**, *22*, 3349-3352.

- Marmur, A. “Solid-Surface Characterization by Wetting”, *Annual Review of Materials Research* **2009**, *39*, 473-489.
- Marmur, A. “Soft Contact: Measurement and Interpretation of Contact Angles”, *Soft Matter* **2006**, *2*, 12-17.
- Marmur, A. “The Lotus Effect: Superhydrophobicity and Metastability”, *Langmuir* **2004**, *20*, 9, 3517-3519.
- Merion, T. S.; Marmur, A.; Saguy, I. S. “Contact angle measurement on rough surfaces”, *Journal of Colloid and Interface Science* **2004**, *274*, 637-644.
- Miwa, M.; Nakajima, A.; Fujishima, A.; Hashimoto, K.; Watanabe T. “Effects of the Surface Roughness on Sliding Angles of Water Droplets on Superhydrophobic Surfaces”, *Langmuir* **2000**, *16*, 13, 5754-5760.
- Murakami, D.; Jinnai, H.; Takahara, A. “Wetting Transition from the Cassie-Baxter State to the Wenzel State on Textured Polymer Surfaces”, *Langmuir* **2014**, *20*, 2061-2067.
- Neuhaus, S.; Spencer, N. D.; Padeste, C. “Anisotropic Wetting of Microstructured Surfaces as a Function of Surface Chemistry”, *ACS Applied Materials & Interfaces* **2012**, *4*, 123-130.

- Nishimoto, S.; Bhushan, B. “Bioinspired Self-Cleaning Surfaces with Superhydrophobicity, Superoleophobicity, and Superhydrophilicity”, *RSC Advances* **2013**, *3*, 3, 671-690.
- Nosonovsky, M. “Model for solid-liquid and solid-solid friction of rough surfaces with adhesion hysteresis”, *Journal of Chemical Physics* **2007**, *126*, 224701.
- Nosonovsky, M.; Bhushan, B. “Wetting of rough three-dimensional superhydrophobic surfaces”, *Microsyst Technol* **2006**, *12*, 273-281.
- Oner, D.; McCarthy, T. J. “Ultrahydrophobic Surfaces. Effects of Topography Length Scales on Wettability”, *Langmuir* **2000**, *16*, 7777-7782.
- Park, C. I.; Jeong, H. E.; Lee, S. H.; Cho, H. S.; Suh, K. S. “Wetting Transition and Optimal Design for Microstructured Surfaces with Hydrophobic and Hydrophilic Materials”, *Journal of Colloid and Interface Science* **2009**, *336*, 298-303.
- Park, S. G.; Moon, J. H.; Jeon, H. C.; Yang, S. M. “Anisotropic wetting and superhydrophobicity on holographically featured 3D nanostructured surfaces”, *Soft Matter* **2012**, *8*, 4567-4570.
- Pashos, G.; Kokkoris, G.; Boudouvis, A. G. “Minimum Energy Paths of Wetting Transitions on Grooved Surfaces”, *Langmuir* **2015**, *31*, 3059-2068.

- Pozzato, A.; Zilio, S. D.; Fois, G.; Vendramin, D.; Mistura, G.; Natali, M. “Superhydrophobic surfaces fabricated by nanoimprint lithography”, *Microelectronic Engineering* **2006**, *83*, 4-9, 884-888.
- Radha, B.; Lim, S. H.; Saifullah, M. S. M.; Kulkarni, G. U. “Metal hierarchical patterning by direct nanoimprint lithography”, *Scientific Reports* **2013**, 1078.
- Rao, A. V.; Latthe, S. S.; Nadargi, D. Y.; Hirahima, H.; Ganesan, V. “Preparation of MTMS based transparent superhydrophobic silica films by sol–gel method”, *Journal of Colloid and Interface Science* **2009**, *332*, 484-490.
- Ren, W. Q. “Wetting Transition on Patterned Surfaces: Transition States and Energy Barriers”, *Langmuir* **2014**, *30*, 10, 2879-2885.
- Rukosuyev, M. V.; Lee, J.; Cho, S. J.; Lim, G.; Jun, MBG. “One-step fabrication of superhydrophobic hierarchical structures by femtosecond laser ablation”, *Applied Surface Science* **2014**, *313*, 411-417.
- Sameoto, D.; Menon, C. “Recent Advances in the Fabrication and Adhesion Testing of Biomimetic Dry adhesives”, *Smart Materials and Structures* **2010**, *19*, 10, 103001.
- Sahoo, B. N.; Kandasubramanian, B. “Recent progress in fabrication and characterisation of hierarchical biomimetic superhydrophobic structures”, *RSC Advances* **2014**, *4*, 22053-22093.

- Shao, J. Y.; Ding, Y. C.; Wang, W. J.; Mei, X. S.; Zhai, H. P.; Tian, H. M.; Li, X. M.; Liu, B. “Generation of Fully-Covering Hierarchical Micro-Nano-Structures by Nanoimprinting and Modified Laser Swelling”, *Small* **2014**, *10*, 2595-2601.
- Sommers, A. D.; Jacobi, A. M. “Wetting phenomena on micro-grooved aluminum surfaces and modeling of the critical droplet size”, *Journal of Colloid and Interface Science* **2008**, *328*, 402-411.
- Song, D.; Song, B. W.; Hu, H. B.; Du, X. S. Ma, Z. B. “Contact angle and impinging process of droplets on partially grooved hydrophobic surfaces”, *Applied Thermal Engineering* **2015**, *85*, 356-364.
- Sun, T. L.; Feng, L.; Gao, X. F.; Jiang, L. “Bioinspired surfaces with special wettability”, *Accounts of Chemical Research* **2005**, *38*, 644-652.
- Suzuki, H.; Okada, M.; Yamagata, Y.; Morita, S.; Higuchi, T. “Precision grinding of structured ceramic molds by diamond wheel trued with alloy metal”, *CIRP Annals Manufacturing Technology* **2012**, *61*, 283–286.
- Tanaka, D.; Buenger, D.; Hildebrandt, H.; Moeller, M.; Groll, J. “Unidirectional Control of Anisotropic Wetting through Surface Modification of PDMS Microstructures”, *Langmuir* **2013** *29*, *40*, 12331-12336.
- Tie, L.; Guo, Z. G.; Liu, W. M. “Anisotropic wetting properties on various shape

- of parallel grooved microstructure”, *Journal of Colloid and Interface Science* **2015**, *453*, 142-150.
- Vukusic, P.; Hooper, I. “Directionally Controlled Fluorescence Emission in Butterflies”, *Science* **2005**, *310*, 1151-1151.
- Vukusic, P.; Sambles, J. R. “Photonic structures in biology”, *Nature* **2003**, *424*, 852-855.
- Wang, J.; Chen H.; Sui T.; Chen D. “Investigation on hydrophobicity of lotus leaf: Experiment and theory”, *Plant Science* **2009**, *176*, 687-695.
- Wang, S.; Jiang, L. “Definition of Superhydrophobic States”, *Advanced Materials* **2007**, *19*, 3423-3424.
- Wanger, T.; Neinhuis, C.; Barhlott, W. “Wettability and Contaminability of Insect Wings as a Function of Their Surface Sculptures”, *Acta Zoologica* **1996**, *77*, 213-225.
- Watson, G. S.; Myhra, S.; Cribb, B. W.; Watson, J. A. “Putative Functions and Functional Efficiency of Ordered Cuticular Nanoarrays on Insect Wings”, *Biophysical Journal* **2008**, *94*, 3352-3360.
- Wenzel, R. N. “Resistance of Solid Surfaces to Wetting by Water”, *Ind. Eng. Chem.* **1936**, *28*, 988-994.

- Wolfram, E.; Fraust, R. “Wetting, Spreading, and Adhesion”, Padday, J. F., ed., *Academica Press, London* **1978**, Chapter 10, 212-222.
- Wu, D.; Wang, J. N.; Wu, S. Z.; Chen, Q. D.; Zhao, S. A.; Zhang, H.; Sun, H. B. Jiang, L. “Three-Level Biomimetic Rice-Leaf Surfaces with Controllable Anisotropic Sliding”, *Advanced Functional Materials* **2011**, 21, 2927-2932.
- Wu, S. Z.; Wu, D.; Yao, J.; Chen, Q. D.; Wang, J. N.; Niu, L. G.; Fang, H. H.; Sun, H. B. “One-Step Preparation of Regular Micropearl Arrays for Two-Direction Controllable Anisotropic Wetting”, *Langmuir* **2010**, 26, 12012-12016.
- Xia, D. Y.; Johnson, L. M.; Lopez, G. P. “Anisotropic Wetting Surfaces with One-Dimensional and Directional Structures: Fabrication Approaches, Wetting Properties and Potential Applications”, *Advanced Materials* **2012**, 24, 1287-1302.
- Xiao, F.; Yuan, S. J.; Laing, B.; Li, G. Q.; Pehkonen, S. O.; Zhang, T. J. “Superhydrophobic CuO nanoneedle-covered copper surfaces for anticorrosion”, *Journal of Materials Chemistry A* **2015**, 3, 4374-4388.
- Yang, H. T.; Dou, X.; Fang, Y.; Jiang, P. “Self-assembled biomimetic superhydrophobic hierarchical arrays”, *Journal of Colloid and Interface Science* **2013**, 405, 51-57.

- Yang, H. T.; Jiang, P. “Scalable fabrication of superhydrophobic hierarchical colloidal arrays”, *Journal of Colloid and Interface Science* **2010**, *352*, 558-565.
- Yang, Y. L.; Hsu, C. C.; Chang, T. L.; Kuo, L. S.; Chen, P. H. “Study on wetting properties of periodical nanopatterns by a combinative technique of photolithography and laser interference lithography”, *Applied Surface Science* **2010**, *256*, 3683-3687.
- Yao, X.; Chen, Q. W.; Xu, L.; Li, Q. K.; Song, Y. L.; Gao, X. F.; Quere, D.; Jiang, L. “Bioinspired Ribbed Nanoneedles with Robust Superhydrophobicity”, *Advanced Functional Materials* **2010**, *20*, 656-662.
- Yeh, K. Y.; Chen, L. J. “Contact Angle Hysteresis on Regular Pillar-Like Hydrophobic Surfaces”, *Langmuir* **2008**, *24*, 245-251.
- Yong, J. L.; Yang, Q.; Chen, F.; Zhang, D. S.; Du, G. Q.; Hao, B.; Si, J. H.; Hou, X. “Bioinspired superhydrophobic surfaces with directional Adhesion”, *RSC Advances* **2014**, *4*, 8138-8143.
- Yong, J. L.; Yang, Q.; Chen, F.; Zhang, D. S.; Farooq, U.; Du, G. Q.; Hou, X. A. “A Simple Way to achieve Superhydrophobicity, Controllable Water Adhesion, Anisotropic Sliding, and Anisotropic Wetting based on Femtosecond-laser-induced Line-patterned Surfaces”, *Journal of Materials Chemistry A* **2014**, *2*, 5499-5507.

- Yu, D. P.; Wong, Y. S.; Hong, G. S. “Ultraprecision machining of micro-structure functional surfaces on brittle materials”, *Journal of Micromechanics and Microengineering* **2011**, *21*, 095011.
- Zhang, D. S.; Chen, F.; Fang, G. P.; Yang, Q.; Xie, D. G.; Qiao, G. J.; Li, W.; Si, J. H.; Hou, X. “Wetting characteristics on hierarchical structures patterned by a femtosecond laser”, *Journal of Micromechanics and Microengineering* **2010**, *20*, 075029.
- Zhang, F. X.; Low, H. Y. “Anisotropic Wettability on Imprinted Hierarchical Structures”, *Langmuir* **2007**, *23*, 7793-7798.
- Zhang, P. C.; Liu, H. L.; Meng, J. X.; Yang, G.; Liu, X. L.; Wang, S. T.; Jiang, L. “Grooved Organogel Surfaces towards Anisotropic Sliding of Water Droplets”, *Advanced Materials* **2014**, *26*, 19, 3131-3135.
- Zhang, Q. L.; To, S.; Zhao, Q. L.; Guo, B. “Amorphization and C segregation based surface generation of Reaction-Bonded SiC_s-Si composites under micro-grinding”, *International Journal of Machine Tools & Manufacture* **2015**, *95*, 78-81.
- Zhao, H.; Law, K. Y. “Directional Self-Cleaning Superoleophobic Surface”, *Langmuir* **2012**, *28*, 11821-11827.

Zhao, H.; Law, K. Y.; Sambhy, V. “Fabrication, Surface Properties, and Origin of Superoleophobicity for a Model Textured Surface”, *Langmuir* **2011**, *27*, 5927-5935.

Zhao, H.; Park, K. C.; Law, K. Y. “Effect of Surface Texturing on Superoleophobicity, Contact Angle Hysteresis, and “Robustness””, *Langmuir* **2012**, *28*, 14952-14934.

Zheng, Y. M.; Gao, X. F.; Jiang, L. “Directional adhesion of superhydrophobic butterfly wings”, *Soft Matter* **2007**, *3*, 178-182.

Zhu, Z.; To, S.; Zhang, S. “Theoretical and experimental investigation on the novel end-fly-cutting-servo diamond machining of hierarchical micro-nanostructures”, *International Journal of Machine Tools & Manufacture* **2015**, *94*, 15-25.